Complex vectorial beam state manipulation through gradient index optics



Chao He

Jesus College
Michaelmas Term 2019

A thesis submitted for the degree of Doctor of Philosophy
at the University of Oxford

Declaration

The material contained within this thesis has not previously been submitted for a degree at the University of Oxford or any other university. The research reported within this thesis has been conducted by the author unless indicated otherwise.

Copyright Notice

The copyright of this thesis rests with the author. No quotation from it should be published without the prior written consent of the author, and any information derived from it should be acknowledged.

Acknowledgements

Most scientific research may be carried in solitude, however helping hands pushed the progress forward. Since January 2018 embarking on my DPhil career, I am so lucky to have numerous hands to help me and also be the witnesses of my growth. It is really my honour to have chance to thank the people played important roles throughout my DPhil journey here.

First of all, to my supervisor, Prof. Martin J. Booth, for whom I have immense respect. His broad vision and patient guidance shepherded my growth from a fresh science graduate to a professional researcher. He also models the kind of leader I aspire to become: a modest, easy-going and helpful person. When I encountered problems in my research, he always tried the best to help and found time to discuss with me. It is indeed my great fortune to work in Martin's lab, and for the whole experience I would forever be grateful.

I also would like to thank my college advisor. Prof. Steve Morris, for many nice chats and his support to my DPhil study. Thanks all my colleagues at Dynamic Optics and Photonics Group, especially Dr. Jingyu Wang, Dr. Jacopo Antonello and Mrs. Qi Hu – in assistance with the whole process of the aspects of simulations and experiments in my project. Thanks Dr. Patrick Salter, Dr. Jun Guan, Dr. Raphael Turcotte, Dr. Mick Phillips, Dr. Karen Hampson, Dr. Matthew Wincott, Dr. Chris Chong, Dr. Ravi Shivaraman, Dr. Syed Asad Hussain, Andrew Kirkpatrick, Yuanyuan Dai, Aurelien Barbotin, Nicholas Hall, Jiahe Cui and so on colleagues. With the friendship of our research group – 'life is no longer tough' :).

Then, I also would like specifically thank Prof. Hui Ma, Prof. Honghui He, Dr. Jintao Chang from Tsinghua University, Prof. Peng Xi from Peking University, Prof. Daniel S. Elson, Dr. Jianyu Lin from Imperial College London, Dr. Ben Dai from City University of Hong Kong, Dr. Shaoxiong Liu from Shenzhen Sixth People's Hospital (Nanshan Hospital) for their strong support and help in my DPhil career. And also thank Dr. Neal Radwell from University of Glasgow, Dr. C. T. Samlan from University of Hyderabad, Miss. Yang Dong, Mr. Donghong Lv, Prof. Yonghong He and Prof. Nan Zeng from Tsinghua University, Prof. Hailu Luo from Hunan University, Prof. Desen Liu, Prof. Xiaoping Jiang and Prof. Sumei Zhou from Southwest University, Dr. Ji Qi from

University College London, Mr. Zhao Liu from Femto Technology Co. Ltd., and Mr. Herbert Stürmer from GRINTECH GmbH for the helpful discussions about various topics.

Again, I would like to thank my supervisor Prof. Martin J. Booth, thanks for his strong support in giving me the studentship to cover most fees of my DPhil career. I always understand that a funding support for an oversea student is a rare case. I indeed appreciate it very much and the only thing I can do to return back is to try the best to make great scientific achievements.

Finally, and always, I am truly thankful to my family – my parents and my grandparents. They kept providing me endless love and always making their best to support me with my study, career and life. I am nothing without their unconditional love and the values they have instilled in me. They are the single most important thing in my life, and every accomplishment I achieve, I do it for them.

Chao He in Oxford
December 2019

Key Abbreviations

AM Angular momentum
AO Adaptive optics
CN Condition number
DOP Degree of polarisation
DM Deformable mirror
FWHM Full width at half maximum
GRIN lens Gradient index lens
GLS GRIN lens systems
HWP Half waveplate
KDP Potassium Dihydrogen Phosphate
MM Müller matrix
MMAC Müller matrix anisotropy coefficients
MMPD Müller matrix polar decomposition
MMT Müller matrix transformation
NA Numerical aperture
OAM Orbital angular momentum
P Polariser
P-AO Polarisation adaptive optics
PB Pancharatnam-Berry
PSA Polarisation state analyser
PSF Point spread function
PSG Polarisation state generator
QWP Quarter waveplate
RI Refractive index
SAM Spin angular momentum
SHEL Spin-Hall effect of light
SHWP Spatially-variant half waveplate
SLM Spatial light modulator
SOC Spin-orbital conversion
SOI Spin-orbital interaction
SOP State of polarisation
V-AO Vectorial adaptive optics
VB Vector beams
VVB Vector vortex beams

Contents

Abstract **10**

1 Introduction **11**

1.1 Background: A brief history of optical lenses 11

1.2 GRIN lens in the scalar approximation: History, development and basic functions 14

1.3 GRIN lens in the vectorial domain: A new vectorial beam manipulator 20

1.4 Thesis overview – scope and aim 26

2 Polarisation and phase **31**

2.1 Introduction – Polarisation and phase of light field 31

2.1.1 Vectorial light description 31

2.1.1.1 Linear, circular, elliptical polarisation, depolarised light 32

2.1.1.2 Jones vector 35

2.1.1.3 Stokes vector 36

2.1.1.4 Polarisation ellipse and Poincaré sphere 40

2.1.2 Principle of vectorial light responses 44

2.1.2.1 Jones matrix 44

2.1.2.2 Müller matrix 46

2.1.2.3 Müller matrix decomposition methods 47

2.1.2.4 Jones-Müller transformation 51

2.2 Polarimeter 53

2.2.1 Polarimetric techniques 53

2.2.2 System configuration 54

2.2.3 Tissue polarimetry: Polarimetric imaging 60

2.2.3.1 Stokes vector imaging 61

2.2.3.2 Müller matrix imaging 61

2.3 Interferometer 62

2.3.1 Interferometric techniques 63

2.3.2 System configuration....63
2.3.3 Interferometric method for orbital angular momentum (OAM) components analysis....65
2.3.3.1 Spin angular momentum (SAM) and OAM of light....66
2.3.3.2 Geometric phase and spin-orbital interaction (SOI) of light....66
2.4 Summary and discussion....68
3 GRIN lens and its cascade....70
3.1 GRIN lens formulism and characterization in vectorial field....70
3.2 GRIN lens cascade....74
3.3 Basic passive polarisation/phase modulation components characterization....76
3.3.1 Diattenuater....77
3.3.2 Retarder....77
3.4 Optical properties of GRIN lens and its cascade....78
3.4.1 Müller matrix and its corresponding decomposition parameters....79
3.4.1.1 Single GRIN lens: optical properties characterization....79
3.4.1.2 Asymmetric properties of Müller matrices of GRIN lens cascade....80
3.4.2 Spin-Hall effect of light inside GRIN lens....86
3.4.2.1 Single GRIN lens cascade: oblique incident induced symmetric breaking....86
3.4.2.2 Circular anisotropy coefficient of single GRIN lens....88
3.5 Summary and discussion....94
4 Vectorial beam generation through GRIN lens cascade....95
4.1 Vectorial beam generation....95
4.1.1 Vector beam....96
4.1.1.1 Singular vector beam – full Poincaré beam....96
4.1.1.2 Polarisation singularities – single GRIN lens characterization....97
4.1.1.3 Complex polarisation singularities characterization in GRIN lens cascade....100
4.1.2 Vortex beam....110
4.1.2.1 Optical vortex beam – OAM characterization....110

4.1.2.2 Phase singularities – single GRIN lens characterization 111
4.1.2.3 Complex phase singularities characterization in GRIN lens cascade ... 115
4.1.3 Vector vortex beam 118
4.2 Birefringence and eigenmodes of a GRIN lens 119
4.2.1 Eigenmodes of a GRIN lens 119
4.2.2 Axial resolution modification for GRIN lens imaging system 120
4.3 Summary and discussion 123
5 Vectorial beam analysis through GRIN lens cascades 126
5.1 Müller matrix tissue polarimetry 126
5.1.1 Introduction of tissue polarimetry 126
5.1.2 Sequential/simultaneous Müller matrix tissue polarimetry 128
5.2 Snap-shot GRIN lens Müller matrix polarimeter 129
5.2.1 Measurement principle 130
5.2.2 System design 132
5.2.2.1 Single GRIN lens configuration 132
5.2.2.2 Dual GRIN lenses configuration 136
5.2.3 Validation of standard samples 138
5.3 Cancer characterization via GRIN lens cascade 139
5.3.1 GRIN lens cascade polarimeter measurement 141
5.3.2 Data processing algorithm and optimization method 143
5.3.1 Statistical analysis, comparison and error analysis 145
5.4 Summary and discussion 149
6 Vectorial adaptive optics enhanced GRIN lens system 151
6.1 Vectorial adaptive optics 151
6.1.1 Phase correction with traditional adaptive optics 152
6.1.2 Polarisation correction with polarisation adaptive optics 153
6.1.3 Phase and polarisation correction with vectorial adaptive optics 155
6.2 Vectorial adaptive optics correction system 156
6.2.1 Spatial light modulator based geometry 157

6.2.2 Spatial light modulators and deformable mirror based geometry 159
6.3 Vectorial adaptive optics correction in GRIN lens system 161
6.3.1 System confirmation 161
6.3.2 Adaptive polarisation closed-loop correction 165
6.3.2.1 Tilted vortex wave plate 165
6.3.2.2 GRIN lens 168
6.3.3 Vectorial adaptive optics for point spread function modulation 170
6.3.3.1 Point spread function modification (polarisation only) 170
6.3.3.2 Point spread function modification (polarisation and phase) 172
6.4 Summary and discussion 174
7 Conclusion, future work and discussion 176
7.1 Conclusion and future work 176
7.1.1 Novel fluorescence-based imaging methods using GRIN lens cascades 178
7.1.1.1 Micro-endoscope for stimulated emission depletion (STED) microscopy 178
7.1.1.2 Micro-endoscope for structured illumination microscopy 180
7.1.2 New label-free polarimetric method for GRIN lens cascade 180
7.1.2.1 Multi-wavelength micro-endoscopy 181
7.1.1.2 Micro-endoscope with multi-layer scanning 182
7.2 Discussion 183
Reference 184
Journal Publications 207
Participated Conference 208

Abstract

Complex vectorial beam state manipulation through gradient index optics

Submitted for the degree of *Doctor of Philosophy*
Chao He, Jesus College, Michaelmas Term 2019

Gradient index (GRIN) lenses are commonly used for compact imaging systems. It is not widely appreciated that the ion-exchange process that creates the rotationally symmetric GRIN lens index profile also causes a symmetric birefringence variation. This property is usually considered a nuisance, such that manufacturing processes are optimized to keep it to a minimum.

Here, rather than avoiding this birefringence, we understand, harness and overcome its effect by using GRIN lenses in cascade with other optical components to enable extra functionality in commonplace GRIN lens systems.

I first show how the GRIN lens cascades can benefit research in the area of asymmetric Müller matrices and spin-orbital interaction of light, through taking advantage of their optical properties. I then show how birefringence in the GRIN cascades can generate vector vortex beams and foci, and how it can be used advantageously to improve axial resolution. Through using the birefringence for analysis, I show that the GRIN cascades form the basis of a new single-shot Müller matrix polarimeter with potential for endoscopic label-free cancer diagnostics. The versatility of these cascades opens up new technological directions. Additionally, with the help of vectorial adaptive optics, preliminary demonstrations of the correction of the birefringence effect of a GRIN lens were shown both in its pupil domain and focal domain.

I finally give a summary of the whole thesis and provide an outlook for future work with an emphasis on novel fluorescence-based or label-free imaging systems empowered by GRIN lens cascades.

Chapter 1

Introduction

1.1 Background: A brief history of optical lenses

Optics is probably one of the oldest scientific disciplines. ‘Optics’ is derived from the Greek term *ταὀπτικά* meaning ‘appearance’, ‘look’ [1]. One component of great importance and widely used in optics is optical lens. Lens comes from *lēns*, the Latin word for ‘lentil’, because a double-convex lens is lentil-shaped [1, 2]. Ever since early scientists began to investigate the world we live in, questions corresponding to light, such as what the nature of light is, what the properties of it are and phenomena related to light-matter interaction – gained widespread attention [3]. Simple answers have been emerging since the first crude lens was created by the ancient Egyptian and Mesopotamian scientists, followed by theories on light and vision developed by ancient Greek philosophers and the development of geometrical optics in the Greco-Roman world [1, 3]. Generations of scientists over the world across different continents such as Asia, Africa and Europe started to put forward hypothesises, validate formulations, and design optical systems so

that experiments can be performed in the hope of explaining scientific theories – with the help of the great assistants: lenses [3]. The collective efforts of revealing and characterising the behaviour of light, greatly strengthen the basis of the optical research. With significant development in physical and physiological optics in the medieval Islamic world, research of light was advanced in early Europe [4]. These former studies on optics are now described as 'classical optics' [5]. Over two thousand years later, rapid development in many research fields has enabled the investigation in 'modern optics' [5, 6] – which focuses on new research areas including quantum optics [6].

Archaeological evidence indicates that around 700 BC, ancient Egyptians and Mesopotamians started polishing crystals, mainly quartz, in the attempt to recur the optical functionalities that they noticed can be induced in water. Between 750 BC and 710 BC the first lenses were known to be made using polished quartz in ancient Assyria, known as Nimrud/Layard lens [7]. This lens may have been used as a burning glass or magnifying glass [7]. There are many similar lenses from ancient Egypt, Greece and Babylon. However, glass lenses were not invented until the Middle Ages [8]. As a predecessor to modern glass lens – 'reading stones' were invented between the 11th and 13th centuries aiming to assist in illuminating texts by monks [9]. This can be considered as a prototype of plano-convex lenses – normally made by cutting a sphere glass into half at that time [9]. Around 1286, history of optics changed dramatically with *Friar Salvino*

D'Armate's creation of the first wearable spectacles (there are other voices arguing that the first pair of glasses were possibly made in Pisan, Italy, but with unclear inventors). This craft soon spread across Europe, especially in Netherlands and Germany, which became the centres of spectacle manufacturing in the 14th and 15th centuries [3]. It paves the way for contemporary scientists to explore deeper into exciting discoveries.

Practical development and experimentation of lenses led to the invention of the compound optical microscope around 1595, and the refracting telescope in 1608, both of which appeared in the spectacle-making centres in the Netherlands [10]. *Galileo Galilei* greatly improved upon the designs of telescopes from *Hans Lippershey* and *Jacob Metius's* early designs [11]. *Isaac Newton* is credited to build the first functional reflection telescope in 1668 by using his Newtonian reflector [12]. As for microscopes (the original inventor unknown), it has been claimed as inventor by *Zacharias Janssen* and/or his father *Hans Martens* in 1590 [13], also by an expatriate called *Cornelis Drebbel* who had a unit in London in 1619 [14, 15]. *Galileo Galilei* seems to have found around 1609 that he could also use his telescope to view small objects [11, 16]. After seeing a compound microscope built by *Drebbel* exhibited in Rome) in 1624, he improved the design and built his own [11, 16]. In the meantime, *Johannes Kepler* picked up the investigation of the laws of optics from his lunar essay of 1600 [17]. He then developed and expanded the understanding

in geometric optic in the early 17th century including generating and recording the thoughts of inner mechanism of human retina, convex, concave lenses, and properties of light [17]. The development of optics continued with the efforts of *Willebrord Snellius* (Snell's law), *René Descartes* (Descartes' law), *Christiaan Huygens* (Opera reliqua) and *Isaac Newton* – whose book 'Opticks' was a great achievement at that time [5, 6, 18]. The inventions of telescopes and optical microscopes led to a great deal of experimentations, especially on the shapes of lenses, in the 17th and early 18th centuries – including those trying to correct chromatic and spherical aberrations induced in lenses [3]. Opticians and related companies tried to construct lenses with varying degrees of curvature (as recorded, they assumed the aberrations arose from defects in the spherical figure of their surfaces [3]). Optical theory of refraction validated that no single-element lens could bring all colours to a focus – this led to the invention of the compound achromatic lens or achromat by *Chester Moore Hall* in England in 1733 (an invention claimed at the same time by *John Dollond* who patented it in 1758). The advances in lens development have always been moving forward with the wheel of history (besides the glimpse of this brief history) owing to numerous physicists, mathematicians and engineers [5, 6].

1.2 GRIN lens in the scalar approximation: History, development and basic functions

The development history of gradient index (GRIN) lens should be traced back to the early studies of astronomical refraction [19, 20, 21]. In 1100 AD, *Alhazan* pointed out that the flattening effect of the sun's disk near the horizon was due to astronomical refraction [21]. *Cassini*, in 1656, applied Snell's law correctly to the observation/assumption but also assumed the homogeneity of the refractive index (RI) distribution of the atmosphere [21]. Further developments resulted in the establishment of enhanced models proposing a concentric symmetry in RI distribution [21]. It has been the insight of many that inhomogeneous media, such as that with a gradually changing RI, can be taken advantage of in optical systems [19, 21]. However, it wasn't until 1854 that *Maxwell* put forward an ideal instrument, commonly known as 'Maxwell's fisheye lens' [20, 21]. The lens has a spherical symmetric index function about one point and it was expected that a light beam could be focussed from one point on the sphere to another, as shown in Figure 1.1. Due to limitations in the manufacturing technology and lack of potential applications at that time, the fisheye lens has been preserved as a theoretical existence [21]. In 1964, *Lüneburg* put forward a lens that could focus every parallel beam into the same foci [19, 20, 21]. However, some requirements make this lens difficult to manufacture, one of them being that the RI of its spherical surface needs to match that of the surrounding medium [19, 20, 21].

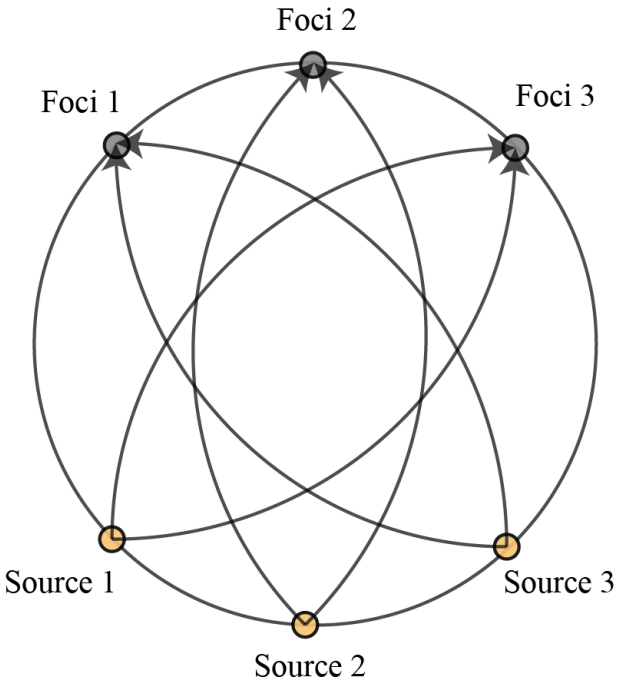


Figure 1.1 Sketch of Maxwell's fisheye lens – an ideal model.

In 1958, *Morgan* and other researchers generalized *Lüneburg*'s formula and reported that a GRIN lens can be designed to meet that focus/imaging propose, from one external sphere to another external sphere [21]. *Wood* (1905) discovered a method to construct a lens that has two plane surfaces but with gradually changing RI along the radial direction [21]. His method was based on a dipping technique through a cylinder of gelatine, generating an internal graded RI distribution about the optical axis [21]. *Wood* demonstrated when slicing this cylinder orthogonally relative to the axis, that the detached slice could act as a diverging lens (RI increasing along radius) or converging lens (RI decreasing along radius). Due to imprecisions in the manufacturing process,

noticeable defects were present in these devices, making it very difficult to create practical GRIN lenses. The development of these lenses was therefore slow-moving for several decades [21].

Until a few years ago, a practical technique involving diffusing ions (so called ion-exchange process) into glass to modify its RI – was discovered and applied to the production of high-grade GRIN lens [21]. This successful attempt generated a renewed vigour in the research area of inhomogeneous media. It allows demonstration of theoretical implications in view that it will further lead on to practical applications. A direct impact is to extend the boundary of research in fibre optics [22-30]. Additionally, as such lenses have inherent advantages in mass and size (compared to other eyepieces and objectives), they are capable of being integrated into compact imaging systems such as endoscopic/micro-endoscopic systems, where theoretical work already exist [23-30]. The scope of research is now expected to approach biomedical research and clinical applications [23-26].

It should be noted that there are three types of GRIN lens: spherical gradient lens, axial gradient lens and radial gradient lens [19-22]. Their usage span across various research areas [19-22]. Radial gradient type is most commonly used in modern optics [22]. Shorter ones can be used as coupling lenses in fibre systems or waveguide-based on-chip devices [23, 24, 28]; longer units

are normally treated as relay lenses or objective lenses that can form for example biopsy needles for disease diagnosis [23, 24, 30, 31]. They can also be found in other compact systems, such as fluorescence micro-endoscopes for deep tissue imaging [29, 30]. In this thesis, we focus on the research of radial gradient type GRIN lens.

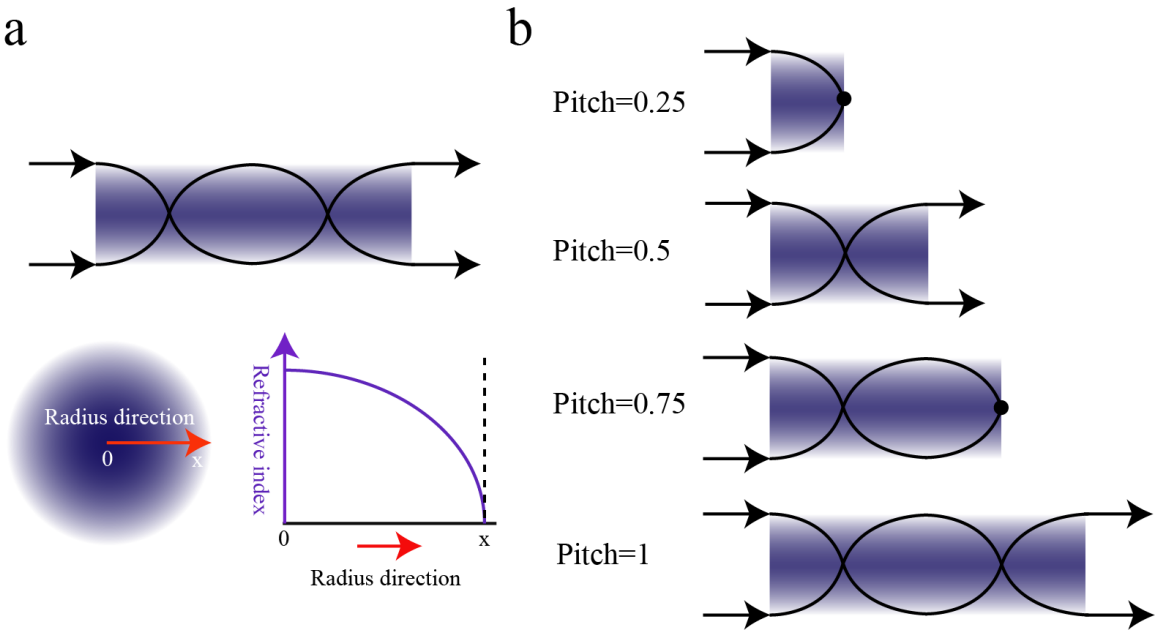


Figure 1.2 (a) Sketches of RI profile of a GRIN lens and its focussing property; (b) Different ray traces inside GRIN lenses with different pitch.

The GRIN lens contains several important parameters: 1) RI profile (Figure 1.2 (a), if we take a section of GRIN lens and measure its RI, it is approximately a parabolic profile with the maximum value in the centre and decreasing along the radial direction [21]); 2) Pitch (P) (Figure 1.2 (b), the 0.25 P represents the performance is equivalent to a normal lens with collimated light input and convergent light output; 0.5 P can be acted as a commonly-used 4F system [21]); 3) Numerical

aperture (NA) (normally the NA of GRIN lens is small, typical value is around 0.1-0.5 [21], in some specific cases it can reach 0.8 with help of special optical designs [25]); 4) Field of view (FOV); 5) Period. More details and other parameters can be found in Ref [21].

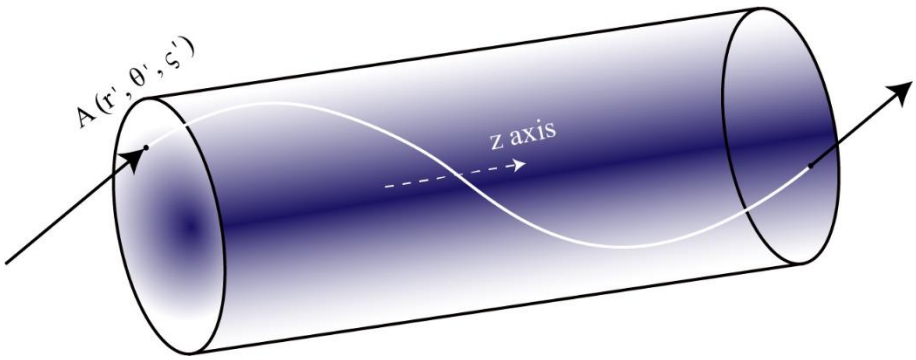


Figure 1.3 Ray tracing inside GRIN lens. The incident point A is represented by $(r', \theta', \varsigma')$, and the inner ray trace is presented via white sinusoid.

For an incident ray on the front surface of the GRIN lens, the distance from the GRIN lens axis is denoted by r, the azimuth of the incident position is denoted by θ, and the interior angle between the ray and the direction of the z axis is denoted by ς. Then an incident point A can be expressed as $(r', \theta', \varsigma')$, as shown in Figure 1.3. An arbitrary point inside the GRIN lens along the propagation ray trace is denoted by $\mathrm{B}(r, \theta, \varsigma)$. The blue double-sided arrow indicates the radial direction, and the orthogonal red counterpart shows the azimuthal direction of that arbitrary point. With the theory of scalar GRIN lens ray tracing [21, 23], the ray path C of the specific incident beam can be represented by Eq. (1-2-1) below,

$$C(z) = r'\cos\left(\sqrt{A}z\right) + \frac{\tan\varsigma'}{\sqrt{A}}\sin\left(\sqrt{A}z\right)$$
$$= \sqrt{r'^2 + \frac{\tan^2\varsigma'}{A}}\cos\left(\sqrt{A}z - \tan^{-1}\frac{\tan\varsigma'}{\sqrt{A}r'}\right) \quad (1\text{-}2\text{-}1)$$

where z is the propagation length along z axis and A is a constant determined by the manufacturing process [21, 23], $\frac{2\pi}{\sqrt{A}}$ is the period and the amplitude is $\sqrt{r'^2 + \frac{\tan^2\varsigma'}{A}}$ [21, 23]. The RI is denoted by n, which is a function of the radius r. We then could express the RI of a GRIN lens in a series form as shown in Eq. (1-2-2) below:

$$n(r) = n(0) + \alpha_1 r + \alpha_2 r^2 + \alpha_3 r^3 + \cdots + \alpha_k r^k \quad (1\text{-}2\text{-}2)$$

Where $n(0)$ is the RI at the centre, and $\alpha_1, \alpha_2, \alpha_3, \cdots \alpha_k$ are constants related to the parameter *A* mentioned before that are determined by the manufacturing process [21, 23]. It should be noted that all the equations above are under the meridional plane approximation [21, 23]. Note that in a rotationally symmetric lens system the meridional plane is the cross-section containing the principal axis and the object point [21, 23].

1.3 GRIN lens in the vectorial domain: A new vectorial beam manipulator

Procedures for fabrication of GRIN lenses are well established: an ion-exchange process creates a rotationally symmetric index profile in the glass rod [32, 33]. There is however an undesirable side-effect: the process also introduces a concomitant intrinsic birefringence that maintains the

same rotational symmetry [32, 33] (see Figure 1.4 (a) to (c)). This gradually changing birefringence profile exhibits the following properties: 1) the magnitude of the retardance is constant at a given radius, 2) the retardance increases with increasing radius; and 3) the slow axis is oriented in the radial direction. These properties mean that the GRIN lens behaves like a spatially variant waveplate array.

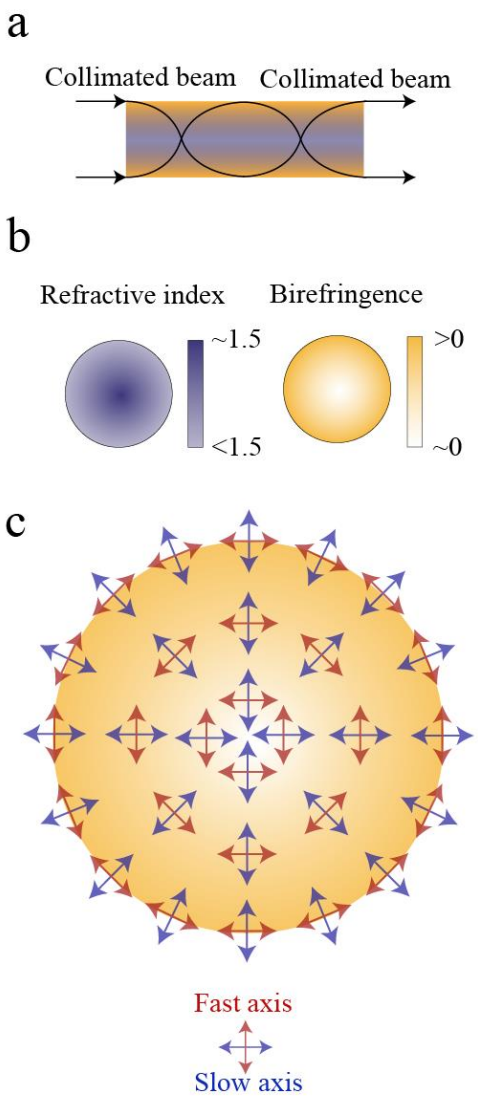


Figure 1.4 GRIN lens properties and GRIN lens cascade. (a) Schematic of the GRIN lens ray trace; (b) show the birefringence and RI profile of a GRIN lens over its cross section. (c) The fast axis/slow axis distribution of the local retardation over one cross-section of the GRIN lens.

From the inherent character of the RI and previous studies about the birefringence property of the GRIN lens [32, 33], we could demonstrate the RI (blue-violet gradually changing colour), birefringence property (yellow gradually changing colour) as well as one arbitrary ray trace (white line) when light propagates through the GRIN lens in Figure 1.5 (a). Figure 1.5 (b) shows the RI and birefringence profile of a GRIN lens section, and shows the curves of these two parameters along the radial direction from centre point to the boundary. The birefringence property implies that vector effects must be considered.

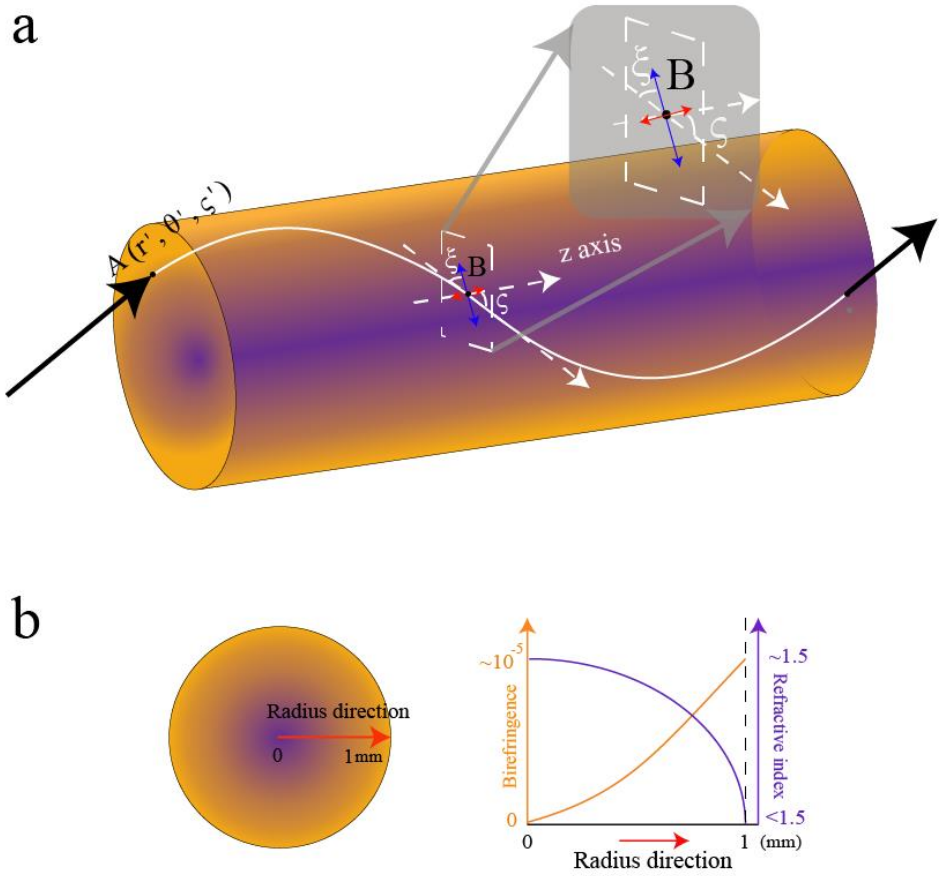


Figure 1.5 GRIN lens properties in a vectorial field. (a) The incident point A is represented by $(r', \theta', \varsigma')$, and an arbitrary point inside the GRIN lens along the propagation ray trace is denoted by B (r, θ, ς). The

blue double-sided arrow indicates the direction of the slow axis (extraordinary axis), and the orthometric red counterpart indicates that of the fast axis (ordinary axis) at the arbitrary point. (b) the section of a GRIN lens shows the RI and birefringence profiles; and the curves of these two parameters along the radial direction from centre to the boundary of the GRIN lens.

Besides the fundamental theoretical equations given in Eq. (1-2-1) and related paragraphs, when the vectorial field is considered, the RI of the *o* rays and *e* rays (for a uniaxial crystal, one of the two rays does indeed obey Snell's Law; this ray is called the ordinary ray (or *o* ray). The other ray (and any ray that does not obey Snell's Law) is an extraordinary ray (or *e* ray) [32, 33]). The two rays are characterised by n_o and n_e respectively, which are functions of the radius r. We then could express the RI of a GRIN lens in a series form as shown in Eq. (1-3-1) below. It should be noted that the magnitude of the difference between n_o and n_e is quantified by the original definition of birefringence: $\Delta n = n_e - n_o$. The unit is consistent.

$$\begin{aligned} n_o(r) &= n_o(0) + \alpha_1 r + \alpha_2 r^2 + \alpha_3 r^3 + \cdots + \alpha_k r^k \\ n_e(r) &= n_e(0) + \beta_1 r + \beta_2 r^2 + \beta_3 r^3 + \cdots + \beta_k r^k \end{aligned} \qquad (1\text{-}3\text{-}1)$$

The polarisation crosstalk effect – or polarisation aberration effect – has been partially studied especially in scalar field applications by many [32, 33]. However, with incomplete understanding of the vectorial nature of light, an important question comes to us – whether this side-effect of the manufacturing process, i.e., the unexpected birefringence, could be understood in more depth or even be taken as an advantage to benefit vectorial field research? In this thesis, rather than avoiding this nuisance birefringence – such that manufacturing processes are optimized to keep

it to a minimum [21] – we have tried to understand and harness it to open up new technological directions for commonplace GRIN lens systems.

There are already numerous existing vectorial beam manipulators [31, 34-37]. Their applications span across fundamental physics, quantum optics, and biomedical applications [31, 34-37]. Figure 1.6 shows a brief structure of the associations of the manipulators. The manipulator contains two categories: passive components and active components. The former one contains numerous everyday optics such as polarizers, waveplates; or more dedicated optical parts such as q-plates [35], metasurfaces [36], reflected cones etc. [34]. The latter one includes deformable mirrors (DM), spatial light modulators (SLM), digital micro-mirror devices (DMD) [38].

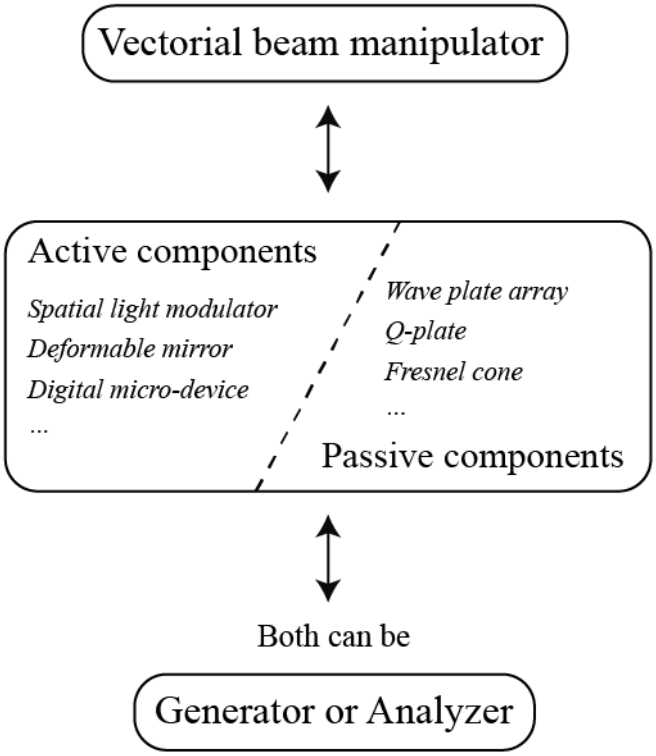


Figure 1.6 Vector manipulators. Several examples for active and passive components.

From another point of view, in optical imaging systems we have both an illumination part and detection part, with the help of vectorial beam manipulators inserted in these two optical paths, a large variety of manipulations involving vectorial beam generation and analysis can be applied to tailor different applications [39-42], such as phase or/and polarisation control in fundamental singularities research [39], optical communication [40], nanoparticle manipulation [41] and microscopy/endoscopy techniques [42]. Learning from a similar conception, here we introduce the GRIN lens and its unexpected birefringence into the field of vectorial beam manipulation – with scopes in both beam generation and analysis. By understanding its vectorial manipulation

ability and effects, new GRIN lens imaging methods can be delivered, leading to more potential application prospects – if we bear in mind its basic function as a focusing/imaging lens.

1.4 Thesis overview – scope and aim

This thesis mainly focuses on the question of how to better understand and take advantage of the gradually changing birefringence of radial type GRIN lens, to explore new techniques in the vectorial field with an emphasis on adding extra functionalities to traditional GRIN lens imaging systems.

Chapter 2 gives a main introduction to the basic concepts that are used in this thesis, including mathematical characterisations of polarisation and phase of a light beam, description of vectorial light responses of objects as well as related applications. The polarimeter and interferometer are introduced as well alongside with their functionalities and usage in this thesis. Specific applications for polarimeter such as biomedical tissue polarimetry, and orbital angular momentum characterization, as well as their corresponding mechanisms and methodologies are also explained briefly.

Then, a key conception, also the main novelty of this project – "GRIN lens cascades" is put forward. These cascades comprise one or more GRIN lenses with interstitial optical elements, including polarizers and waveplates. Such combinations of elements introduce myriad possibilities for structuring the phase and polarisation of beams and foci. Chapter 3 describes the construction of different GRIN lens cascades with an emphasis on characterization of the optical properties of single GRIN lens cascade. The research of asymmetric properties of Müller matrices (MMs) and spin-Hall effect of light are also introduced. They are explained by analysing the optical properties of GRIN lens cascades themselves. Primary data and corresponding analysis are also presented. Figure 1.7 shows the map of the thesis structure (from this Chapter).

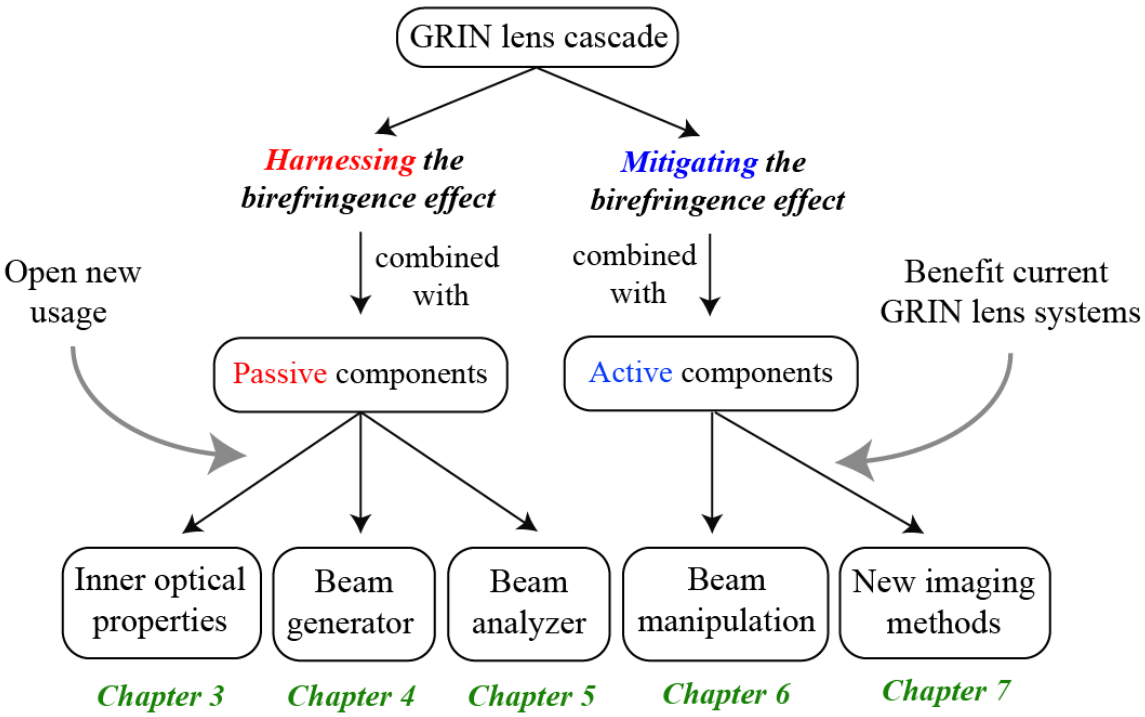


Figure 1.7 Thesis structure. Chapters 3, 4 and 5 are under the structure of harnessing the unexpected birefringence effect to open new usage for GRIN lens systems; and Chapter 6 and 7 are under the structure of mitigating the birefringence effect for traditional GRIN lens systems.

The gradually changing birefringence profile means that the GRIN lens behaves like a spatially variant waveplate array (as shown in Figure 1.4 (c)), providing a continuum of birefringence states that can manipulate the polarisation and phase of a light beam. Chapter 4 presents that how we could harness the birefringence and use a GRIN lens cascade as a vectorial beam generator to generate vector beam, vortex beam and vector vortex beam. The concepts and basic mathematical descriptions of those three beams are introduced and a detailed analysis of corresponding singularities including polarisation singularities (related with vector topological charges) and phase singularities (containing orbital angular momentum components) are presented as well. Through understanding the generation ability of a GRIN lens cascade (or say, the effect of spatial variant polarisation aberration), we also put forward a possible method to enhance the axial resolution of GRIN lens imaging systems and pave the way to new imaging methods for GRIN lens imaging systems, which might benefit endoscopic systems such as fluorescence GRIN lens micro-endoscope.

As the cascade can act as a generator, it is natural to treat it as an analyser. Chapter 5 describes how the GRIN lens cascade enables comprehensive polarisation detection based on MM

measurement, which can be used in label-free sensing. We present two different designs for the new endoscopic imaging system with experiments for feasibility validation. The optimisation and calibration process of the systems are also discussed. An interesting demonstration of cancer characterization via GRIN lens cascade is presented in Chapter 5 to show potential biomedical/clinical application. Data processing algorithms, optimization methods, statistical analysis and error analysis are also presented.

As previous techniques are based on passive components, new prospects can be explored using active devices such as SLMs to act as interstitial components in GRIN lens cascades. Chapter 6 introduces that through combining SLMs and/or DMs into current GRIN lens based imaging systems, we can perform full polarisation and phase control of the beam and hence enable vectorial adaptive optics enhanced endoscopic systems. As GRIN lens systems contain relatively huge polarisation aberration (led by its inner birefringence), it would introduce not only polarisation aberration but also phase aberration – which can have intrinsic interactions that are crucial not only for normal fluorescence imaging methods but also related polarisation sensing methods. We use dynamic phase/polarisation modulation devices to manipulate the phase and polarisation states of the beam to improve the imaging contrast of current GRIN lens based

systems such as fluorescence micro-endoscopy and label-free sensing micro-endoscopy. Preliminary data are given with explanations and corresponding future prospects.

Chapter 7 summarises the thesis and provides an outlook for future work with an emphasis on novel fluorescence-based/label-free imaging systems empowered by GRIN lens cascades.

Chapter 2

Polarisation and phase

2.1 Introduction – Polarisation and phase of light field

This chapter outlines the background theories, corresponding concepts and introduces the technical tools used in this thesis. Section 2.1 shows the mathematical characterization of 1) polarisation and phase properties of light with an emphasis on its electromagnetic form; 2) the fundamental polarisation/phase response of matter and related methods to interpret them using Müller and Jones matrices. Two fundamental tools for vectorial beam state measurement, polarimeter and interferometer are introduced in Section 2.2 and 2.3, followed with a short introduction of their history and development, system configuration as well as their main applications that are demonstrated in this thesis (polarimeter: tissue polarimetry; interferometer: orbital angular momentum components analysis). Section 2.4 gives a summary of this chapter followed by a discussion.

2.1.1 Vectorial light description

Light – which has been harnessed for several hundreds of years – emerges in numerous research areas such as astronomy and microscopy [43]. Compared with the scalar form of electromagnetic radiation, its vectorial field study has a shorter history. As a result, the exploration of vectorial light for applications such as sensing and imaging still remains active [43, 44]. There is particular interest in light beams that contain complex polarisation and phase structure [43, 44, 45]. The complex structures 1) are not confined solely to the transverse plane (lateral plane) but also to the longitudinal axis along the propagation direction; 2) can be performed in the phase domain and/or polarisation domain; 3) are not confined to pure polarisation light, but also (partially or fully) depolarised light; 4) are generated by both coherent sources (such as lasers) and incoherent sources (such as LEDs).

2.1.1.1 Linear, circular, elliptical polarisation, depolarised light

Waves in nature consists of both transverse wave and longitudinal waves [43]. The oscillating disturbance for a longitudinal wave is parallel to the direction of the propagation, such as sound waves in air [43]. As for transverse waves, e.g., electro-magnetic waves, the wave vector oscillation disturbance is perpendicular to the propagation direction [43].

Light is an electro-magnetic wave. We can use the electric field formulism to describe light for simplification if we only consider the corresponding response from matter. For a light beam

propagating in the z direction, the oscillation direction of the electric wave vector is confined in the *xy* plane that is perpendicular to *z*. In the spatial domain, the electric field of monochromatic waves can be described as a function of *z* and time *t*:

$$\begin{aligned}\mathbf{E}(z,t) &= \mathbf{E}(z_0,t_0)\exp\left[i\left(\frac{2\pi}{\lambda}(n+ik)z-\omega t+\delta_E(z_0,t_0)\right)\right]\\ &= \mathbf{E}_x(z,t)+\mathbf{E}_y(z,t)\\ &= E_x(z,t)\vec{\boldsymbol{x}}+E_y(z,t)\vec{\boldsymbol{y}}\\ &= E_x(z_0,t_0)\exp\left[i\left(\frac{2\pi}{\lambda}(n+ik)z-\omega t+\delta_x(z_0,t_0)\right)\right]\vec{\boldsymbol{x}}+\\ &\quad E_y(z_0,t_0)\exp\left[i\left(\frac{2\pi}{\lambda}(n+ik)z-\omega t+\delta_y(z_0,t_0)\right)\right]\vec{\boldsymbol{y}}.\end{aligned} \tag{2-1-1}$$

where $\mathbf{E}(z_0,t_0)$, and $\delta_E(z_0,t_0)$ are original electric field and phase at the initial moment, respectively. $\mathbf{E}_x(z,t)$ and $\mathbf{E}_y(z,t)$ are the components of $\mathbf{E}(z,t)$ in *x* and *y* directions. For the components in *xy* plane, $E_x(z_0,t_0)$, $E_y(z_0,t_0)$ and $\delta_x(z_0,t_0)$, $\delta_y(z_0,t_0)$ are their amplitude and phase at the initial moment. ω is frequency. Component $n'=n+ik$ represents complex refractive index of the matter, with refractive index *n* and extinction coefficient *k*. When the communication medium has no absorption (i.e., $k=0$), the electric field oscillates in a sinusoidal form. However, the exponential form is widely-used due to its flexibility in dealing with complex functions. This sinusoidal format equation can be expressed as

$$\begin{aligned}\mathbf{E}(z,t) &= E_x(z_0,t_0)\cos\left(\frac{2\pi n}{\lambda}z-\omega t+\delta_x(z_0,t_0)\right)\vec{\boldsymbol{x}}+\\ &\quad E_y(z_0,t_0)\cos\left(\frac{2\pi n}{\lambda}z-\omega t+\delta_y(z_0,t_0)\right)\vec{\boldsymbol{y}}.\end{aligned} \tag{2-1-2}$$

Consider the trajectory of electric field vector within a fixed *xy* plane, the disturbance of a plane time-harmonic wave may either be along a single direction, or rotate periodically at the wave frequency, or oscillate in a disorganized manner – known as definitions of linear polarisation state, circular/elliptical polarisation state and depolarised state, respectively.

Note:

1) The framework of polarisation optics was built by ***Thomas Young****,* ***Etienne-Louis Malus*** *and* ***Augustin-Jean Fresnel*** *through investigating the birefringence properties of calcite crystals [43, 44]. **Fresnel** developed wave equations to characterize optical disturbance and explained in detail the optical effects of birefringence in the 19th century [43, 44]. In the early 20th century, **James Clerk Maxwell** indicated that light is a propagating electro-magnetic field and established Maxwell's equations to reveal the polarisation nature of light [43, 44].*

2) For a pure polarised light beam, the polarisation state of light is defined by two parameters a) the amplitude of field $\boldsymbol{E}_x$ *and* $\boldsymbol{E}_y$*; b) the relative phase between field* $\boldsymbol{E}_x$ *and* $\boldsymbol{E}_y$*; Assuming that the amplitudes are equal for* $\boldsymbol{E}_x$ *and* $\boldsymbol{E}_y$ *a) when relative phase* $\delta=\delta_y(z_0,t_0)-\delta_x(z_0,t_0)$ *equals to 0°/180°, field* $\boldsymbol{E}$ *becomes 45°-*

45° linearly polarised; b) when δ equals ±90°, the polarisation state is referred to as circular polarisation; c) Except from the cases in point a) and b), the rest are referred to as elliptical polarised light.

*3) The definition of right-hand circular polarised light (clockwise rotation) and left-hand circular polarised light (anticlockwise rotation) are different in optics books and academic communities. It depends on whether the observer 'sees' the light from the source (**Agreement I**), or from the detector (**Agreement II**). Institute of Electrical and Electronics Engineers (IEEE) uses the **Agreement I**, so it is also widely used in engineering science fields; Quantum physicists also use **Agreement I** to be consistent with the particle spin states [45]. However, for numerous optics books such as Principle of Optics (Born&Wolf [43]) and Handbook of Optics [46], **Agreement II** is used. In this thesis, we use **Agreement II** in order to correspond to such scientific references.*

2.1.1.2 Jones vector

Jones vectors can only represent non-depolarised state of a light beam [47-51]. As we have discussed above, any electrical field **E** can be decomposed into two orthogonal vectors (along *x* and *y* axis), each vector with its own amplitude A_i and phase ϕ_i. Note in general we choose *p* or *s* polarised (parallel and senkrecht) orientation as *x* or *y* axis of the local coordinate system assuming x is on the plane of incidence [47], in the vicinity of a surface [47]. Then, the Jones vector for an electrical field can be defined as:

$$\begin{pmatrix} E_x \\ E_y \end{pmatrix} = \begin{pmatrix} E_p \\ E_s \end{pmatrix} = \begin{pmatrix} A_p e^{i\varphi_p} \\ A_s e^{i\varphi_s} \end{pmatrix}. \quad \text{(2-1-3)}$$

Note:

1) It should be pointed out that when we say ***phase*** *for a vectorial beam, two types of phase are normally referred. One is absolute phase and one is relative phase [49, 50, 51]. Jones vector formulism contains the functionalities of 1) doing the mathematical calculations for (multiple) beam interference issues; 2) revealing the absolute phase performance.*

2) When only one single (uniform) beam is considered, the absolute phase effect can be neglected. Either $\phi_p=0$ *or* $\phi_s=0$ *(in Eq. (2-1-3)), then the Jones vector can be translated into a Stokes vector via the well-known Pauli matrices transformation [49, 50, 51].*

2.1.1.3 Stokes vector

While the light beam contains depolarised characteristics, a Jones vector is no longer sufficient for describing light properties comprehensively [48-51]. The reason is that for partially polarised light (or fully depolarised light), the performance of the trajectory of the electrical vector in the chosen *xy* plane is semi-disordered (or completely disordered) alongside the propagation process, so that more degrees of freedom are required to describe the field [48-51]. In the scope of linear

optics, a light beam that contains depolarised part can be described by a *4 × 1* vector, named coherence vector *C* [48-51],

$$\mathbf{C} = \left(C_1, C_2, C_3, C_4\right)^T = \left(\left\langle E_p E_p^* \right\rangle, \left\langle E_p E_s^* \right\rangle, \left\langle E_s E_p^* \right\rangle, \left\langle E_s E_s^* \right\rangle\right)^T . \tag{2-1-4}$$

where C_1 and C_4 are real numbers, and C_2 and C_3 are conjugate complex values. The bracket <> represents mathematical expectation. The Stokes vector of the light beam can be calculated by a matrix transformation via a relay matrix *A* [48-51],

$$\mathbf{S} = \mathbf{AC}, \quad \mathbf{A} = \begin{pmatrix} 1 & 0 & 0 & 1 \\ 1 & 0 & 0 & -1 \\ 0 & 1 & 1 & 0 \\ 0 & i & -i & 0 \end{pmatrix}. \tag{2-1-5}$$

where vector *S* is:

$$\mathbf{S} = \begin{bmatrix} S_0 \\ S_1 \\ S_2 \\ S_3 \end{bmatrix} = \begin{bmatrix} \left\langle E_p E_p^* + E_s E_s^* \right\rangle \\ \left\langle E_p E_p^* - E_s E_s^* \right\rangle \\ \left\langle E_p E_s^* + E_s E_p^* \right\rangle \\ i\left\langle E_p E_s^* - E_s E_p^* \right\rangle \end{bmatrix} = \begin{bmatrix} I_p + I_s \\ I_p - I_s \\ I_{45°} - I_{-45°} \\ I_R - I_L \end{bmatrix}. \tag{2-1-6}$$

where I_p, I_s, I_{45}, I_{-45} are projection intensities (different linear component in directions of 0°, 90°, 45°, -45°) of a light beam, I_L and I_R are components of left/right hand circular. From Eq. (2-1-6) we know that Stokes vector can be based on intensity measurement, while Jones vector is defined by amplitude and phase that cannot be directly measured. For this reason, throughout the whole

thesis we emphasise Stokes vector measurements and its analysis in consideration of the flexibility of the measurement. Equation (2-1-6) can be rewritten to the form of (2-1-7), as below,

$$\mathbf{S}=\begin{bmatrix}S_0\\S_1\\S_2\\S_3\end{bmatrix}=\begin{bmatrix}\langle E_pE_p^*+E_sE_s^*\rangle\\\langle E_pE_p^*-E_sE_s^*\rangle\\\langle E_pE_s^*+E_sE_p^*\rangle\\i\langle E_pE_s^*-E_sE_p^*\rangle\end{bmatrix}=\begin{bmatrix}\langle a_p^2+a_s^2\rangle\\\langle a_p^2-a_s^2\rangle\\\langle 2a_pa_s\cos\delta\rangle\\\langle 2a_pa_s\sin\delta\rangle\end{bmatrix}. \quad (2\text{-}1\text{-}7)$$

where $\delta=\delta_p-\delta_s$ is the retardance (phase different) between two orthogonal vector components, a_p and a_s are the modulus of vector E_p and E_s. The bracket <> represents a time-averaged value. When the changing rate of retardance stays constant, i.e., $d\delta/dt=0$, we can deduce from Eq. (2-1-7) to $S_0^2=S_1^2+S_2^2+S_3^2$. This indicates that the light beam is a fully polarised light – i.e., the chirality, ellipticity and azimuthal angle of the polarisation properties of the light beam are independent of time. However, if $d\delta/dt\neq0$, the component $a_pa_se^{i\delta}$ and $a_pa_se^{-i\delta}$ are both functions of time. This implies depolarised properties are present in the light beam. Several parameters can be interpreted from the Stokes vector to describe this property [48-51], such as the degree of polarisation (DOP), degree of linear polarisation (DOLP) and degree of circular polarisation (DOCP) of light, mathematical definitions can be found in Eq. (2-1-8) below:

$$\begin{aligned}DOP&=\frac{\sqrt{S_1^2+S_2^2+S_3^2}}{S_0}\\DOLP&=\frac{\sqrt{S_1^2+S_2^2}}{S_0}\\DOCP&=\frac{S_3}{S_0}\end{aligned}. \quad (2\text{-}1\text{-}8)$$

As for a single (uniform polarised) light beam, the DOP is 1 for fully polarised, 0 for unpolarised or completely depolarised, and 0-1 for partially polarised. The DOP cannot be larger than 1 [48-51]. Despite containing four elements, a Stokes vector contains fewer than four degrees of freedom due to physical constraints [48-51]. The Stokes vector can be considered as an incoherent superposition of a completely polarised and an unpolarised part of the light field.

Note:

1) A Stokes vector can be written in several forms. ***Stokes*** *(1852) used A, B, C, D;* ***Walker*** *(1954) used I, Q, U, V that is widely adopted in scattering/polarimetic optics methods (for tissue characterization) especially in biomedical research [43, 49].* ***Perrin*** *(1942) and* ***Shurcliff*** *(1962) used I, M, C, S;* ***Collett*** *(1968) used S_0, S_1, S_2, S_3 that is widely adopted in the field of polarisation measurement.* ***Rozenberg*** *(1960) used S_1, S_2, S_3, S_4 in order to meet the notation consistency with Müller matrix (discussed below). For clarity, we use S_0, S_1, S_2, S_3 in this thesis.*

2) For a beam generated via incoherence light source (such as an LED), the Stokes vector can be directly added by scalar calculation. Therefore, partially polarised light can be divided into two parts – fully

polarised/depolarised components [51]. Eq. (2-1-9) below can be used to decompose Stokes vectors, where $\boldsymbol{S}_u$ *and* $\boldsymbol{S}_p$ *represent fully depolarised and polarised components respectively.*

$$\begin{aligned}\mathbf{S}&=\mathbf{S}_u+\mathbf{S}_p\\&=\left(\left(S_u\right)_0,\quad 0,\quad 0,\quad 0\right)^T+\left(S_0-\left(S_u\right)_0,\quad S_1,\quad S_2,\quad S_3\right)^T.\end{aligned}\qquad (2\text{-}1\text{-}9)$$

3) In consideration of the issues in experiments, a number of factors contribute to depolarisation. We conclude three main reasons in this Note. It should be pointed out that in general the Stokes vector polarimeter is based on intensity measurement [47], so a) for the reason that intensity recorded via a detector includes a time-involved integration process, if the polarisation state changes rapidly, Eq. (2-1-8) interprets the reason for depolarisation. This reason is given in the time domain; b) when imaging processes are involved in the experiment, every point on the beam section may accumulate through various sub-beams that have different polarisation states, leading to depolarised properties. This reason is given in the spatial domain; c) as is the case with all intensity measurements, the spectral range of the detected light must be considered. Hence for different wavelengths, differences in $\delta=\delta_p-\delta_s$ *may lead to depolarisation as well. This reason is given in the spectral domain.*

2.1.1.4 Polarisation ellipse and Poincaré sphere

Graphical representation exhibits an intuitive way to describe phase and polarisation state of light [51]. Jones vector and Stokes vector can use the Polarisation ellipse and Poincaré sphere respectively to visualize the field [51]. These two methods are inherently related.

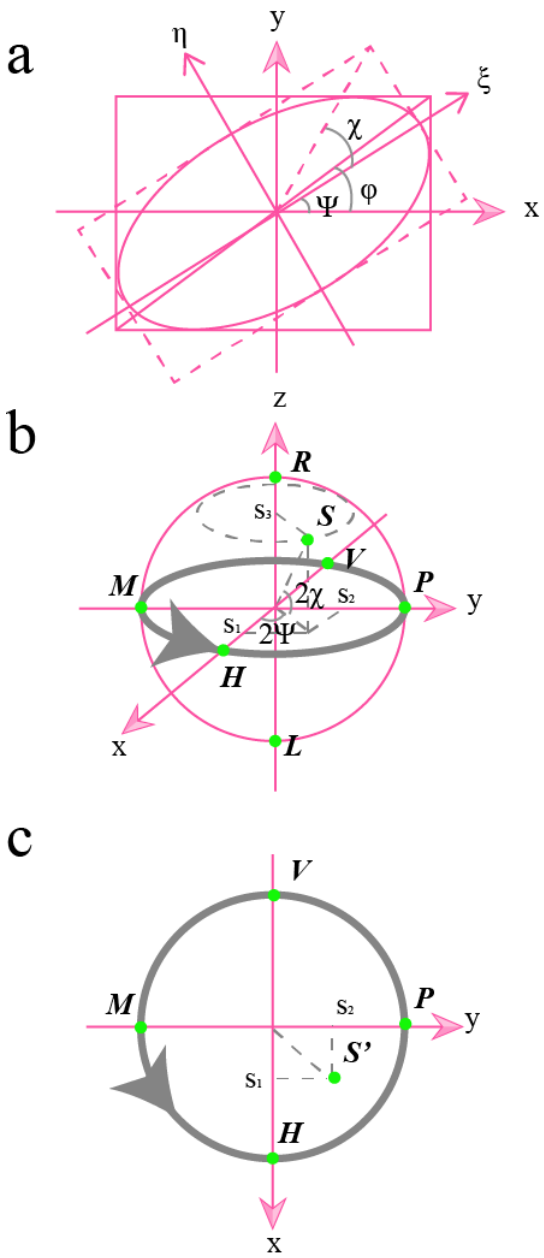


Figure 2.1 Polarisation ellipse and Poincaré sphere. (a) Polarisation ellipse to present polarisation state of light. (b) Poincaré sphere to present polarisation state of light. (c) Linear polarised light circle on Poincaré sphere (the equator).

As we have discussed above, in an *xy* plane, a certain trajectory (with retardance $\delta=\delta_y(z_0,t_0)-\delta_x(z_0,t_0)$) of the electrical vector can perform in an elliptical shape (Figure 2.1 (a)). In Figure 2.1 (a), the length and width of the grey dotted rectangle box represent the long/short axis of the ellipse. The length and width of the solid grey box is the external rectangle for the ellipse along the *xy* coordinate. The transformation equations for the parameters in Figure 2.1 (a) are concluded below, with χ, ψ, φ, δ representing ellipticity, long axis direction, relay angle and retardance respectively [47, 51].

It should be noted that the polarisation ellipse is only appropriate to describe completely polarised light. On the other hand, the Poincaré sphere is also compatible with partially polarised and depolarised light [47, 51]. According to Eqs. (2-1-7) and (2-1-8), the Stokes vector can be also expressed by Eq. (2-1-11).

$$\tan 2\psi = \tan 2\varphi \cos\delta, \quad \sin 2\chi = -\sin 2\varphi \sin\delta. \tag{2-1-10}$$

$$\mathbf{S} = \begin{pmatrix} S_0 \\ S_1 \\ S_2 \\ S_3 \end{pmatrix} = S_0 \begin{pmatrix} 1 \\ DoP \cdot \cos 2\varphi \\ DoP \cdot \sin 2\varphi \cos\delta \\ DoP \cdot \sin 2\varphi \sin\delta \end{pmatrix} = S_0 \begin{pmatrix} 1 \\ DoP \cdot \cos 2\chi \cos 2\psi \\ DoP \cdot \cos 2\chi \sin 2\psi \\ DoP \cdot \sin 2\chi \end{pmatrix}. \tag{2-1-11}$$

The Poincaré sphere can demonstrate the state of polarisation (SOP) in a three-dimensional coordinate system with the basis of S_1, S_2 and S_3. It is a unitary sphere that represents complete polarisation states on its surface and depolarised states inside the sphere [47, 51]. A unitary (by intensity) Stokes vector (i.e., $[S_0, S_1, S_2, S_3]/S_0$) starts at the center point (origin) of the Poincaré sphere and terminates either on the surface or inside the sphere. Figure 2.1 (b) and (c) give a convenient demonstration of the Poincaré sphere and the projection of its equator. The length of this derived vector denotes the DOP of light. *H*, *V*, *M*, *P* on capital letters are specific polarisation states [47, 51] such as horizontally polarised (*H*), vertically polarised (*V*), 45 degree polarised (*M*) and -45 degree polarised (*P*). According to Eq. (2-1-10), the polarisation ellipse parameters χ (and ψ) can be interpreted from the azimuth angle (and the polar angle) of the derived vector inside the Poincaré sphere using Eq. (2-1-11) and Eq. (2-1-12), shown below.

$$\begin{aligned}
&\delta = \tan^{-1}\left(\frac{S_3}{S_2}\right), \qquad \psi = 0.5\tan^{-1}\left(\frac{S_2}{S_1}\right), \\
&\chi = 0.5\sin^{-1}\left(\frac{S_3}{\sqrt{S_1^2+S_2^2+S_3^2}}\right) = 0.5\tan^{-1}\left(\frac{S_3}{\sqrt{S_1^2+S_2^2}}\right), \\
&\varphi = 0.5\cos^{-1}\left(\frac{S_1}{\sqrt{S_1^2+S_2^2+S_3^2}}\right) = 0.5\tan^{-1}\left(\frac{S_1}{\sqrt{S_2^2+S_3^2}}\right).
\end{aligned} \tag{2-1-12}$$

Note:

It should be pointed out that the graphical representation contains no absolute phase information – which is sometimes not addressed in typical vectorial beam analysis such as pure polarisation measurement or tissue polarimetry [47, 51]. However, the absolute phase variation is indeed directly related to the pathway of the 'polarisation state changing' vector on the surface of the Poincaré sphere, where usually it is referred to as 'induced' geometric phase [52] – which will be explained in the later sections/chapters.

2.1.2 Principle of vectorial light responses

The phase and polarisation of a light beam may change significantly on interaction with matter. This can be used to characterize optical properties of the objects [48, 49, 50]. Such interactions (transformations) can be described via matrices – normally Jones or Müller matrices [51]. In the following sections, we introduce Jones and Müller matrices calculations as well as several of the cutting-edge decomposition methods for the Müller matrix with emphasis on applications of biomedical tissues characterization.

2.1.2.1 Jones matrix

Following the description in Eq. (2-1-3), when a light beam, described by Jones vector interacts with an object, the vectorial beam state transformation ([*R. C. Jones* in 1941]) can be described as below:

$$\begin{pmatrix} E_p^{out} \\ E_s^{out} \end{pmatrix} = \begin{pmatrix} J_{pp} & J_{ps} \\ J_{sp} & J_{ss} \end{pmatrix} \begin{pmatrix} E_p^{in} \\ E_s^{in} \end{pmatrix}. \quad (2\text{-}1\text{-}13)$$

where J_{ij} is element of Jones matrix [51]. Similar to the Jones vector, the *absolute phase* (transformation) information can be manipulated and presented via Jones matrix calculation as well [51]. The degrees of freedom in a Jones matrix are eight. Those parameters all should be kept when the targeted applications are concentrated on the details of input/output vectorial beams.

Note:

Jones matrix is widely used in lots of research areas related to polarimetric techniques, typically in the area of ellipsometry [47]. The main targeted samples in ellipsometry, thin films, are in general isotropic [47]. So, the Jones matrix of the sample can degenerate into Eq. (2-1-14), where r_p and r_s are reflective coefficients, and their ratio ρ can represent elliptical angle parameters Ψ and Δ [47] (see Eq. (2-1-15)).

$$\begin{pmatrix} E_p^{out} \\ E_s^{out} \end{pmatrix} = \begin{pmatrix} r_p & 0 \\ 0 & r_s \end{pmatrix} \begin{pmatrix} E_p^{in} \\ E_s^{in} \end{pmatrix}. \quad (2\text{-}1\text{-}14)$$

$$\rho = \frac{r_p}{r_s} = \tan\Psi e^{i\Delta}. \quad (2\text{-}1\text{-}15)$$

where *0≤Ψ≤90°, 0≤Δ≤360°, ρ=f*(θ,λ) *was a function of incident angle and wavelength. Eq. (2-1-16) can be represented by the equation below as well.*

$$\tan\Psi = \frac{|r_p|}{|r_s|} \quad , \quad \Delta = \arg(r_p) - \arg(r_s) = \delta_p - \delta_s. \qquad (2\text{-}1\text{-}16)$$

2.1.2.2 Müller matrix

When using Stokes vector – similar to Jones vector – the transformation is defined by a *4×4* matrix named Müller matrix devised by *Hans Müller* in 1943 [47, 48]. With an input SOP ($\boldsymbol{S}_{in}$), the transformation properties of the object (Müller matrix, *M*) transform the SOP into an output Stokes vector ($\boldsymbol{S}_{out}$). This interaction process can be expressed through Eq. (2-1-17) below,

$$\mathbf{S}_{out} = \mathbf{M}\mathbf{S}_{in} = \begin{pmatrix} m_{11} & m_{12} & m_{13} & m_{14} \\ m_{21} & m_{22} & m_{23} & m_{24} \\ m_{31} & m_{32} & m_{33} & m_{34} \\ m_{41} & m_{42} & m_{43} & m_{44} \end{pmatrix} \cdot S_{in}. \qquad (2\text{-}1\text{-}17)$$

Stokes-Müller formulism is defined in the same vectorial space, so they own the same pros and cons. It should be noted that when described the optical properties of an object via Müller matrix, the coordinate system should be taken into consideration [51]. For instance, for a system that has a reference plane (such as *xy* plane) and a reference axis (such as *x* axis), the presented Müller matrix should be rotated via a rotation matrix *Rot* with respect to an angle φ to keep accordance

to input/output SOP. The transformation is specified by Ref [51] and can be expressed by Eq. (2-1-18), where *Rot* represents the rotation matrix with respect to the reference plane.

$$M(\varphi) = Rot(-2\varphi)MRot(2\varphi),$$

$$Rot(\varphi) = \begin{pmatrix} 1 & 0 & 0 & 0 \\ 0 & \cos\varphi & \sin\varphi & 0 \\ 0 & -\sin\varphi & \cos\varphi & 0 \\ 0 & 0 & 0 & 1 \end{pmatrix}. \quad (2\text{-}1\text{-}18)$$

M matrix was transformed via *Rot* (see Eq. (2-1-18)) [51] – implied by 1) The rotation transformation does not change the matrices' eigenvalue; 2) it would change specific value which means the Müller matrices are sensitive to the coordinate system; 3) when use Müller matrix to characterize the properties of the object, the orientation of the sample always need to be taken into consideration; 4) angle-free parameters are expected to be derived from Müller matrix in characterization of biomedical or other material samples.

2.1.2.3 Müller matrix decomposition methods

As we discussed before, a Müller matrix contains 16 elements. Individual Müller matrix elements lack clear physical meaning and association with structural properties, and are sensitive to the choice of coordinate system [49]. Previous researchers made great effort to extract specific polarisation parameters from Müller matrix [53-61] to characterize the optical and structural properties of the object. One prevalent method is the Müller matrix polar-decomposition (MMPD)

proposed by *Shih Y. Lu* and *Russell A. Chipman* [53], which has been used and validated in lots of research and applications of biomedical/material samples characterizations; *Honghui He* and his colleagues put forward Müller matrix transformation (MMT) with validations using Monte Carlo simulation [58] and biomedical sample characterization [61]; *Oriol Arteaga* and his colleagues derived Müller matrix anisotropy coefficients (MMAC) to describe the level of different kinds of anisotropy of different polarisation systems [57]. Besides, other parameters were also developed [54, 55, 56]. In this thesis, we use these three methods, which are suitable for analyzing complex turbid media.

Müller matrix polar decomposition (MMPD) method decomposes the complicated interactions between sample and polarised light into three basic phenomena [53]: diattenuation (D) – resulting in different absorption ratio of the two eigen polarisation state (electrical vector) of light beam, retardance (R) – resulting in different phase delay of the two eigen polarisation state (electrical vector) of light beam and depolarisation (Δ) – resulting in the semi-disordered (or completely disordered) orientation of the electrical vector in the chosen plane alongside the propagation process. The main principle is represented by Eq. (2-1-19), where the M_Δ, M_R and M_D are the 4×4 sub-matrices of depolarisation, retardance, and diattenuation, respectively.

$$M_{Sample} = M_\Delta M_R M_D. \tag{2-1-19}$$

The diattenuation D can be readily obtained from the second to fourth elements in the first row of a Müller matrix, i.e. elements m_{12}, m_{13} and m_{14} respectively, as shown in Eq. (2-1-20). The retardance R is reconstructed from the trace of M_R; while the orientation of optical axis of linear retardance θ (with respect to the horizontal axis) ranging from $-\frac{\pi}{2}$ to $\frac{\pi}{2}$ radians is calculated using Eq. (2-1-20). The depolarisation properties are defined by the bottom right 3×3 matrix m_Δ of matrix M_Δ. λ_1, λ_2 and λ_3 in Eq. (2-1-20) are the eigenvalues of m_Δ, and P is a matrix composed of the eigenvectors of m_Δ. Δ_L and $\Delta_c$are linear/circular depolarisation values.

$$
\begin{aligned}
D &= \sqrt{m_{12}^2 + m_{13}^2 + m_{14}^2}, \\
R &= \cos^{-1}\left[\frac{\mathrm{tr}(M_R)}{2} - 1\right], \\
\theta &= \frac{1}{2}\tan^{-1}\left[\frac{M_{R23} - M_{R32}}{M_{R31} - M_{R13}}\right],
\end{aligned}
\qquad (2\text{-}1\text{-}20)
$$

$$
m_\Delta = P\begin{pmatrix} \lambda_1 & 0 & 0 \\ 0 & \lambda_3 & 0 \\ 0 & 0 & \lambda_3 \end{pmatrix}P^{-1}, \quad \Delta_L = 1 - \frac{\lambda_1+\lambda_2}{2}, \quad \Delta_R = 1 - \lambda_3.
$$

Müller matrix transformation (MMT) parameters have been obtained to reveal the polarisation properties of objects especially biomedical samples through calculating different combinations of the elements of the Müller matrix [58]. Compared with MMPD method, the MMT method presents several advantages [58] such as faster calculation/decomposition speed, which can benefit the cases such as fast *in vivo* clinical diagnosis [61-65]. Similar to MMPD, there are

several extracted angle-free polarization MMT parameters: depolarisation property (*1-b*), level of anisotropy (t_1), diattenuation property (t_2), level of birefringence (t_3) and fast axis orientation (x_3). The mathematical presentations of the parameters are given in Eq. (2-1-21) below:

$$\begin{aligned} 1\text{-}b &= 1-\frac{m_{22}+m_{33}}{2}, \\ t1 &= \frac{\sqrt{\left(m_{22}-m_{33}\right)^2+\left(m_{23}+m_{32}\right)^2}}{2}, \\ t2 &= \sqrt{{m_{12}}^2+{m_{13}}^2}, \\ t3 &= \sqrt{{m_{24}}^2+{m_{34}}^2}, \\ x3 &= \frac{1}{2}\tan^{-1}\frac{m_{42}}{-m_{43}}. \end{aligned} \tag{2-1-21}$$

Müller matrix anisotropy coefficients (MMAC) have been proposed to extract the anisotropy properties of the sample from the Müller matrix [57]. Intuitively, the parameters α, β, and γ from MMAC can be regarded as ratios of horizontal linear anisotropy, 45° linear anisotropy and circular anisotropy respectively with respect to the global anisotropy of the Müller matrix [57]. Among them, the circular parameter γ is used to directly reflect the existence of circular birefringence which is also used for example to determine the existence of spin-Hall effect of light among current Müller matrix research [66]. The original mathematical definition of α, β, and γ with respect to Müller matrix elements is shown below:

$$
\begin{aligned}
&\Sigma = 3m_{11}^2 - (m_{22}^2 + m_{33}^2 + m_{44}^2) + 2\Delta, \\
&\Delta = m_{12}m_{21} + m_{13}m_{31} + m_{14}m_{41} - \\
&(m_{34}m_{43} + m_{24}m_{42} + m_{23}m_{32}), \\
&\alpha = \sqrt{\frac{1}{\Sigma}[(m_{12} + m_{21})^2 + (m_{34} - m_{43})^2]}, \cdot \\
&\beta = \sqrt{\frac{1}{\Sigma}[(m_{13} + m_{31})^2 + (m_{24} - m_{42})^2]}, \\
&\gamma = \sqrt{\frac{1}{\Sigma}[(m_{14} + m_{41})^2 + (m_{23} - m_{32})^2]}.
\end{aligned}
\tag{2-1-22}
$$

For a specific system, if the relative sign between dichroism and birefringence is known, the sign of the MMAC parameters α, β, and γ can be determined through following expressions [57]:

$$
\begin{aligned}
&sign(\alpha) = sign(m_{12} + m_{21} \pm (m_{43} - m_{34})), \\
&sign(\beta) = sign(m_{13} + m_{31} \pm (m_{24} - m_{42})), \cdot \\
&sign(\gamma) = sign(m_{14} + m_{41} \pm (m_{23} - m_{32})).
\end{aligned}
\tag{2-1-23}
$$

2.1.2.4 Jones-Müller transformation

As we discussed above, for a non-depolarised light beam and non-depolarizing matter, we could use Jones formulism to describe the interaction between the light and matter using Eq. (2-1-13). The relation can be shown in the equation below:

$$
\left(E_i E_j^*\right)^{out} = \sum_{k,l} J_{ik} J_{jl}^* \left(E_k E_l^*\right)^{in}. \tag{2-1-24}
$$

For the cases of that the matter contains depolarisation properties, we should have the mathematical expectation for both side of Eq. (2-1-24) [50, 51]. In a linear system, we can assume that there is no statistical correlation between the Jones matrix and input electric magnetic field so we could independently have the expectation of them [50, 51] (see Eq. (2-1-25)).

$$\left(E_i E_j^*\right)^{out} = \sum_{k,l} \left\langle J_{ik} J_{jl}^* \right\rangle \left\langle \left(E_k E_l^*\right)^{in} \right\rangle, \quad \text{or} \quad \mathbf{C}^{out} = \mathbf{F}\mathbf{C}^{in}. \tag{2-1-25}$$

Considering the definition of vector ***C*** in Eq. (2-1-4), we could calculate matrix ***F*** through adding subscript tags *ik* and *jl*,

$$\mathbf{F} = \begin{pmatrix} \left\langle J_{pp} J_{pp}^* \right\rangle & \left\langle J_{pp} J_{ps}^* \right\rangle & \left\langle J_{ps} J_{pp}^* \right\rangle & \left\langle J_{ps} J_{ps}^* \right\rangle \\ \left\langle J_{pp} J_{sp}^* \right\rangle & \left\langle J_{pp} J_{ss}^* \right\rangle & \left\langle J_{ps} J_{sp}^* \right\rangle & \left\langle J_{ps} J_{ss}^* \right\rangle \\ \left\langle J_{sp} J_{pp}^* \right\rangle & \left\langle J_{sp} J_{ps}^* \right\rangle & \left\langle J_{ss} J_{pp}^* \right\rangle & \left\langle J_{ss} J_{ps}^* \right\rangle \\ \left\langle J_{sp} J_{sp}^* \right\rangle & \left\langle J_{sp} J_{ss}^* \right\rangle & \left\langle J_{ss} J_{sp}^* \right\rangle & \left\langle J_{ss} J_{ss}^* \right\rangle \end{pmatrix} = \left\langle \mathbf{J} \otimes \mathbf{J}^* \right\rangle. \tag{2-1-26}$$

where $\otimes$ is the Kronecker product, matrix ***F*** represents a transformation matrix for vector ***C***. We then could have Eq. (2-1-27) to Eq. (2-1-29) below via Eq. (2-1-5), Eq. (2-1-25) and Eq. (2-1-26). They can be used to perform Jones-Müller transformation.

$$\mathbf{S}^{out} = \begin{pmatrix} S_0 \\ S_1 \\ S_2 \\ S_3 \end{pmatrix}^{out} = \mathbf{M}\mathbf{S}^{in} = \begin{pmatrix} m_{11} & m_{12} & m_{13} & m_{14} \\ m_{21} & m_{22} & m_{23} & m_{24} \\ m_{31} & m_{32} & m_{33} & m_{34} \\ m_{41} & m_{42} & m_{43} & m_{44} \end{pmatrix} \cdot \begin{pmatrix} S_0 \\ S_1 \\ S_2 \\ S_3 \end{pmatrix}^{in}. \tag{2-1-27}$$

$$\mathbf{M} = \mathbf{A}\mathbf{F}\mathbf{A}^{-1} = \mathbf{A}\left\langle \mathbf{J} \otimes \mathbf{J}^* \right\rangle \mathbf{A}^{-1}. \tag{2-1-28}$$

$$\mathbf{M}=\begin{pmatrix} \frac{1}{2}\left\langle \left|J_{pp}\right|^2+\left|J_{ss}\right|^2+\left|J_{sp}\right|^2+\left|J_{ps}\right|^2 \right\rangle & \frac{1}{2}\left\langle \left|J_{pp}\right|^2-\left|J_{ss}\right|^2+\left|J_{sp}\right|^2-\left|J_{ps}\right|^2 \right\rangle \\ \frac{1}{2}\left\langle \left|J_{pp}\right|^2-\left|J_{ss}\right|^2-\left|J_{sp}\right|^2+\left|J_{ps}\right|^2 \right\rangle & \frac{1}{2}\left\langle \left|J_{pp}\right|^2+\left|J_{ss}\right|^2-\left|J_{sp}\right|^2-\left|J_{ps}\right|^2 \right\rangle \\ \left\langle \mathrm{Re}\left(J_{sp}J_{pp}^{*}+J_{ss}J_{ps}^{*}\right)\right\rangle & \left\langle \mathrm{Re}\left(J_{sp}J_{pp}^{*}-J_{ss}J_{ps}^{*}\right)\right\rangle \\ \left\langle \mathrm{Im}\left(J_{sp}J_{pp}^{*}+J_{ss}J_{ps}^{*}\right)\right\rangle & \left\langle \mathrm{Im}\left(J_{sp}J_{pp}^{*}-J_{ss}J_{ps}^{*}\right)\right\rangle \end{pmatrix} \tag{2-1-29}$$

$$\begin{pmatrix} \left\langle \mathrm{Re}\left(J_{ps}J_{pp}^{*}+J_{ss}J_{sp}^{*}\right)\right\rangle & -\left\langle \mathrm{Im}\left(J_{ps}J_{pp}^{*}+J_{ss}J_{sp}^{*}\right)\right\rangle \\ \left\langle \mathrm{Re}\left(J_{ps}J_{pp}^{*}-J_{ss}J_{sp}^{*}\right)\right\rangle & \left\langle \mathrm{Im}\left(-J_{ps}J_{pp}^{*}+J_{ss}J_{sp}^{*}\right)\right\rangle \\ \left\langle \mathrm{Re}\left(J_{ss}J_{pp}^{*}+J_{sp}J_{ps}^{*}\right)\right\rangle & \left\langle \mathrm{Im}\left(-J_{ss}J_{pp}^{*}+J_{sp}J_{ps}^{*}\right)\right\rangle \\ \left\langle \mathrm{Im}\left(J_{ss}J_{pp}^{*}+J_{sp}J_{ps}^{*}\right)\right\rangle & \left\langle \mathrm{Re}\left(J_{ss}J_{pp}^{*}+J_{sp}J_{ps}^{*}\right)\right\rangle \end{pmatrix}.$$

2.2 Polarimeter

2.2.1 Polarimetric techniques

Polarimetric techniques are up-and-coming tools mainly for various non-fluorescence imaging/sensing applications [66-73] such as 1) recognizing complex biological samples, especially those with fibrous or rod-like structures; as a label-free, anisotropic structure sensitive and multiple-scattered photons suppressing technique, polarimetry can be used to improve the imaging contrast and acquire information accurately of superficial epithelium [68, 71]; 2) characterizing complex material samples, especially for their chiral characteristics and related properties [70] as a label-free detection approach; 3) analysing the states of vectorial light field, studying on complex spin-orbital interaction (SOI) processes of light [66]. There exist various polarimetric techniques that basically can be classified into two categories: Stokes polarimetry

and Müller matrix polarimetry [69]. The former one is used to characterize the properties of light while the later one is used for determining the properties of objects.

2.2.2 System configuration

Due to the fact that a detector can only record intensity information (cannot measure phase directly), the majority of polarimetric techniques are based on intensity measurement and calculation [69]. Stokes polarimeters can be called a polarisation state analyser (PSA), which could be used to calculate any state of polarisation (SOP). In practice, the PSA should at least measure four independent intensity values to reconstruct any arbitrary incident SOP. A Stokes polarimeter normally is defined including a PSA and a detector [69]. A simplified setup is shown in Figure 2.2.

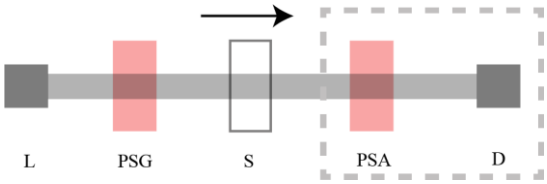


Figure 2.2 Stokes polarimeter (in dotted line box). L: light source; PSG: polarisation state generator; S: sample; PSA: polarisation state generator; D: detector.

A widely used configuration for PSA consists of a polarizer (P) and a quarter waveplate (QWP) [69]. This allows to measure the Stokes vectors of the light field by rotating the waveplate to four different angles, following a process described by Ref [31]. The principal equations for calculation of the Stokes vector light field are shown in Eq. (2-2-1) and Eq. (2-2-2).

$$S_{out}^{n} = M_P M_{QWP}^{n} S_{in},\ (n = 1,2,3,4 \ldots) \quad (2\text{-}2\text{-}1)$$

$$I = A \cdot S_{in}, \qquad S_{in} = A^{-1} \cdot I. \quad (2\text{-}2\text{-}2)$$

where S_{in} is the Stokes vector of the incident light field, M_P and M_{QWP}^{n} are Müller matrices of the corresponding polarizer and waveplate. S_{out}^{n} is the corresponding output Stokes vector for the n^{th} fast axis orientation state of the quarter waveplate. M_{QWP}^{n} is the Müller matrix of the quarter waveplate for the n^{th} fast axis orientation. A is a $n\times4$ matrix known as the instrument matrix [73], which is derived from $M_P \cdot M_{QWP}^{n}$. I is the intensity information recorded by the camera.

Among numerous polarimeters, Müller matrix polarimetry is advantageous because it is capable of extracting comprehensive polarisation properties of the sample [69]. Plenty of optical and structural information of the sample can be extracted by analyzing the obtained 16 elements or polarisation parameters eg: through methods of MMPD, MMT and so on [74] obtained from decomposition of the Müller matrix [74].

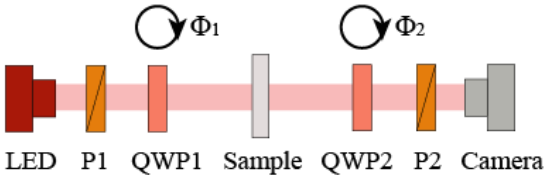


Figure 2.3 Setup of the Müller matrix imaging polarimetry. LED light source; P1, P2: fixed polarizer; QWP1, QWP2: rotated quarter waveplate. Camera as detector.

Figure 2.3 shows a Müller matrix imaging polarimeter via a dual-rotating wave plate method. The polarizers (P1, P2) are fixed and oriented in the same direction. Two quarter waveplates (QWP1, QWP2) rotate with fixed rotational speeds, such that $\phi_1 = 5\phi_2$. The main measurement principle is shown in Eq. (2-2-3) below, where superscript q represents the q^{th} measurement. M_{Sample} is the Müller matrix of the sample, M_{P1}, M_{P2}, M_{QWP1} and M_{QWP2} are Müller matrices of P1, P2, QWP1 and QWP2, respectively. M_{System} is the equivalent overall Müller matrix of the system. S_{in} and S_{out} are incident and output Stokes vectors.

$$S_{out}^{q} = M_{System}S_{in} = M_{P2}M_{QWP2}M_{QWP2}^{q}M_{Sample}M_{QWP1}^{q}M_{P1}S_{in}. \qquad (2\text{-}2\text{-}3)$$

Since the intensity is equivalent to the first element S_0 of the Stokes vector, we make $I^q = (S_{out}^q)_0$, which represents the corresponding intensity of q^{th} measurement. From Eq. (2-2-3) we obtain the Fourier series,

$$I^q = (S_{out}^q)_0 = a_0 + \sum_{n=1}^{12}(a_n \cos 2n\phi_1^q + b_n \sin 2n\phi_1^q). \qquad (2\text{-}2\text{-}4)$$

where a_n and b_n are the Fourier coefficients, and ϕ_1^q is the angle of QWP1 at q^{th} measurement. The Müller matrix of the sample could then be calculated from the Fourier coefficients as shown below. For more details see Ref [75, 76, 77].

$$M_{Sample} = \begin{pmatrix} m_{11} & m_{12} & m_{13} & m_{14} \\ m_{21} & m_{22} & m_{23} & m_{24} \\ m_{31} & m_{32} & m_{33} & m_{34} \\ m_{41} & m_{42} & m_{43} & m_{44} \end{pmatrix} = \begin{pmatrix} a_0 - a_2 + a_8 - a_{10} + a_{12} & 2a_2 - 2a_8 - 2a_{12} & 2b_2 - 2b_8 - 2b_{12} & b_1 - b_9 - b_{11} \\ -2a_8 + 2a_{10} - 2a_{12} & 4a_8 + 4a_{12} & 4b_{12} - 4b_8 & -2b_9 + 2b_{11} \\ -2b_8 + 2b_{10} - 2b_{12} & 4a_8 + 4b_{12} & 4a_8 - 4a_{12} & 2a_9 - 2a_{11} \\ b_3 - b_5 + b_7 & -2b_3 - 2b_7 & -2a_3 + 2a_7 & -a_4 + a_6 \end{pmatrix}. \quad (2\text{-}2\text{-}5)$$

Polarisation measurement belongs to high dimensional data measurement technique [75, 76, 77]. There are two main parts need to be well-calibrated for such measurement [75, 76, 77]: 1) system errors in intensity; 2) system errors in polarisation (errors from instrument matrix). Generally speaking, the system errors in intensity should be taken into consideration (calibrated) for all photoelectric devices, while the instrument matrix errors of polarimeters are specific for polarisation measurement.

For intensity calibration [78, 79, 80], we focus on three aspects. 1) Bias calibration. It is necessary to conduct multi-frame exposure of the dark condition of the detector then calculate the average value of the dark current. The average value should be deducted as a bias, when conducting polarisation imaging. 2) Non-linear response calibration. The non-linear response function is different for various detectors, so normally we could fit the non-linear intensity response curve via *Malus* law and then use it to do the calibration. Some suppliers of the detectors would also provide these curves for calibration. 3) Calibration for other factors. For example, when a system suffers from imaging of highlights scene, the adjacent pixels are quite easily suffer ‘intensity

crosstalk', which should also be calibrated if we aim to do precision imaging; more details can be found in Ref [78, 79].

As for polarisation calibration, there also exist several factors that can affect precise polarisation measurement/imaging (both in Stokes and Müller polarimeters) [78, 79, 80]. We list two factors here. 1) Multi- error sources. In general, each polarimeter contains more than one polarisation modulation device; each individual component may contribute to system errors through the domains of time, space and spectrum (refer to Note 3 in section 2.1.1.3 for details). 2) Complex error transfer processes. Complex errors can play a detrimental role to Stokes-Müller measurement; however, currently, there are no simple rules to describe these errors transfer through the polarisation measurement processes, Müller and the corresponding sources are hard to determine.

Due to the consistency of the measurement/calibration process of Stokes/Müller polarimeters [31] – i.e., Stokes polarimeter can always be treated as the PSA part of the Müller polarimeter. We focus on a widely used Müller matrix polarimeter calibration method in this thesis (setup and fundamental measurement principle can be found in the later part of this section).

In this section, we assume that all the modulation components are perfect with no system errors. However, during the real measurement process, the existed system that contains the polarisation components need to be calibrated [75, 76, 77]. We assume that the original angle (transmission axis angle and fast axis orientation angle) of P1, P2, QWP1 and QWP2 are all at 0 degree. We fix the axis angle of P1 as same as the *x* axis of the local coordinate system. Then the angle mismatch of P2, QWP1 and QWP2 compared with P1 can be described by ε_3, ε_4, ε_5, respectively. Besides the angle errors, the imperfection of the wave plate – retardance errors also play an important role in the contribution of the system errors. That is to say, the retardance of QWP1 and QWP2 may not be perfect at 90 degrees. The unexpected retardance error can be described via δ_1 and δ_2. Other issues such as residual retardance error in polarizer can be omitted in this discussion as they are not the main contributors for the measurement errors. More details can be found in Ref [75, 76, 77].

In general, the calibration of polarimetry needs more than one standard sample for calibration [81]. But as we mentioned above, those components are also source of the system errors. So, it should be pointed out here that the biggest advantage of the dual-rotating wave plate polarimetry method is that the calibration process only needs one standard sample – air [75, 76, 77] that has

little uncertainty issue compared with other standard calibration samples in polarimetry. It will not suffer any manufacture induced side-effects [75, 76, 77].

2.2.3 Tissue polarimetry: Polarimetric imaging

When polarimetry is combined with wide-field imaging, the technique is referred to as polarimetric imaging [68, 74]. Polarimetric imaging has lots of applications such as thin film measurement and characterization [70], cancer diagnosis [82, 83], fundamental studies in light scattering [64], remote sensing [69] and so on. Among them, biomedical sample characterization is one of the main applications of polarimetric imaging [81, 82, 83] especially those used in polarisation microscopic/endoscopic systems [68, 74, 84]. When all four elements of the Stokes vector of the light beam are calculated from the recorded intensity patterns, it is called imaging Stokes polarimetry [85]. Likewise, imaging Müller matrix polarimetry measures and characterizes the polarisation properties of the sample [68, 71]. It should be pointed out that: for imaging Müller matrix polarimetry, there is also a widely-used category – partial Müller matrix polarimetry – which only measures a selected portion of the Müller matrix elements from the sample for some specific research topics [86]. Indeed, considering practical perspectives, it is more desirable to reduce measurement conditions to reduce both time and spatial induced errors with a reduced requirement of the polarisation components [73]. A good example is that when linear polarised response is the dominant like in the research of atmospheric monitoring, people

would prefer 3×3 Müller matrix polarimetric imaging rather than 4×4 Müller matrix polarimetric imaging [87, 88].

2.2.3.1 Stokes vector imaging

Stokes vector imaging technique via Stokes polarimetry only require measuring the polarisation state of the light that emerges from the targets [89, 90]. While compared with the Müller matrix imaging methods, it is much easier to adopt simultaneous (snap-shot) imaging using existing devices such as a polarisation camera with polarizer coating [89] or Stokes camera with the assistant of meta-surfaces [90]. The snap-shot (and of course also time-sequential) Stokes polarimetry has shown great potential in biomedical characterization via rotating linearly polarised or simple circularly polarised illumination – to reveal subsurface structural information of the samples. *Chang, et al.* and *Qi, et al.* also investigated the possibilities to reveal the sample information that contained physical meaning (such as linear retardance) via Stokes vector analysis with a simple circularly polarised light illumination [73, 85]. The technique is validated that can be used in both thin and bulk tissue characterization [85].

2.2.3.2 Müller matrix imaging

Numerous Müller matrix imaging polarimeters have already been proposed in previous studies [91]. Meanwhile, many Müller matrix interpretation methods have been put forward to extract

polarisation parameters to characterize sample information (such as methods of MMPD, MMT, MMAC as we mentioned above). The most widely used method, MMPD interprets Müller matrix in terms of diattenuation, depolarisation, retardance and corresponding axis, which has been validated for both forward and backward geometry detections with a series of Monte Carlo simulations and related experiments [85]. Müller matrix polarimetry thus manifests its great potential in tissue sensing and characterization. *Pierangelo et al.* demonstrated that the depolarisation properties of the sample can be used to distinguish different stages of the colon cancer development [92, 93], while *Antonelli et al.* also showed the ability of stage determination of the human cancerous colon tissue via multi-spectral Müller matrix polarimetry [94]. *Shukla et al.* observed the retardance properties of the cervical tissue that are sensitive to morphological changes around the stroma while significant difference of the depolarisation property in healthy and cancerous regions of human cervix was also observed [95]. *Wood et al.* presented that Müller matrix polarimetry has ability to distinguish micro-organizational state of the myocardium. The technique can also be used to monitor regenerative treatments of myocardial infarction [96]. *Du et al.* and *Wang et al.* also used Müller matrix polarimetry to assist diagnosis of various cancerous tissues, such as skin cancer, cervical cancer and liver cancer [62, 97].

2.3 Interferometer

2.3.1 Interferometric techniques

Interferometric technique is a widely investigated technique in various research fields such as mechanical stress/strain measurement, astronomy, fibre optics, spectroscopy, quantum mechanics, nuclear and particle physics [98]. Amongst numerous types of interferometers, most of them are adopted the interferometric technique via a similar way that the light beam from a single source is split into two beams, one for reference and another one for experiment [31, 34]. Normally they will pass different optical path lengths, as a result, interference fringes is generated with phase information of the interference signal [31, 34]. It should be pointed out that normally the polarisation state of the experiment arm and reference arm should be the same. Otherwise, we normally need to use an additional polarisation state analyser to select same polarisation state distribution (as the reference arm) from the experimental arm to do interferometry [31, 34].

2.3.2 System configuration

Lots of interferometers have been put forward in previous research. Such as well-known Michelson configuration, Mach-Zehnder configuration and Fizeau configuration [98]. Here in Figure 2.4 (a) and (b) we give simple sketches of a Michelson and a Mach-Zehnder configuration interferometers (with inserted polarisation control [31, 34]).

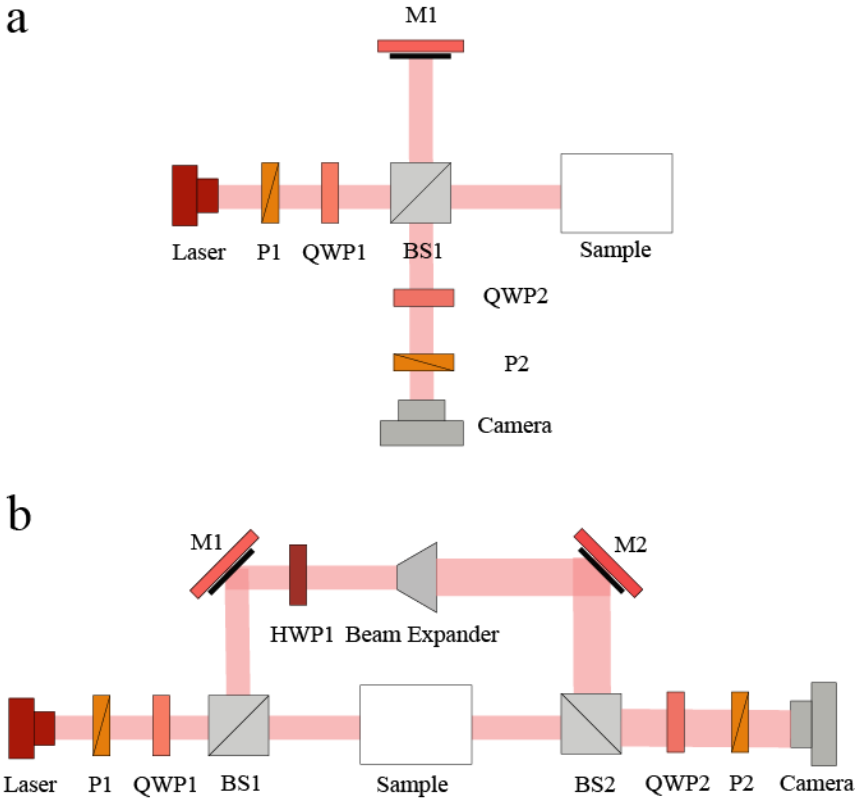


Figure 2.4 Configuration of (a) a Michelson interferometer; (b) a Mach-Zehnder interferometer. P1, P2: polarizer; QWP1, QWP2: quarter waveplate; HWP1: half waveplate; BS1, BS2: beam splitter; M1, M2: silver mirror; Camera: detector.

The general measurement mechanism would be: an incoming coherent light beam will be split into two beams by a beam-splitter; each beam travels a different optical path, and then they will be combined together before recorded by the detector – showing an interference pattern [31, 34]. By analysing the patterns, we could obtain the phase information [99, 100]. Take Figure 2.4 (a) as an example, two paths contain the same optical path length but in real experiment, one of the mirrors would be replaced by the target – normally a wave front modulator (can be a phase and/or amplitude modulator such as a SLM) – so it is defined as the experimental arm [98]. The other arm with a mirror is called the reference arm. When there exists an optical path length difference,

interference fringes are present, from which we could calculate the corresponding phase information of the target beam via various phase retrieving methods, such as Fourier-based fringe analysis [99, 100].

2.3.3 Interferometric method for orbital angular momentum (OAM) components analysis

A light beam possessing a helicoidal phase-front, described by the structure of $e^{il\vartheta}$, carries orbital angular momentum (OAM) of $l\hbar$ (where l is an integer and $\hbar$ is the reduced Planck constant) [40, 41, 101-112]. Since this revelation in 1992 [101], various further applications of this property have been developed, such as optical manipulation [104, 105], optical communications [108, 109], and in quantum and nano-optics [110, 111, 112]. As the fast development of modern optics research such as quantum optics [46], the interferometric techniques continue to find new applications [31, 34]. For example, it was used to determine the existence of the OAM of the photons as well as in the analysis of the OAM components, both in classical optics and quantum optics [31, 34, 106]. In this thesis, to determine the corresponding wavefront (via dealing with issues of polarisation inhomogeneous light fields), we use polarisation state analyser to filter the same polarisation state from the reference beam before applying interferometric technique. It should also be noted that the characterization of OAM in the whole work did not involve in any

phase retrieving process. Detailed mathematical presentations and algorithms information can be found in Ref [31, 34].

2.3.3.1 Spin angular momentum (SAM) and OAM of light

As it was validated in classical optics – the OAM is directly related with the singularities of the phase across the beam section, while the spin angular momentum (SAM) is directly related with circular polarised light [113]. It should be noted that the OAM is only related to the phase profile – independent with intensity profile of the light beams [113], and the origin of OAM is the vortex phase profile resulting in an azimuthal component of the Poynting vector [101, 103].

2.3.3.2 Geometric phase and spin-orbital interaction (SOI) of light

In the context of vectorial light, normally two types of geometric phase will be involved – Rytov-Vladimirskii-Berry (RVB) phase and Pancharatnam-Berry (PB) phase [114, 115, 116]; the former one is related with propagation direction variation of the light beam (such as propagating in inhomogeneous media) [114, 115] while the later one is associated with polarisation manipulation of the light beam (such as propagating in special axis varying crystals) [115, 116]. These two terms of phases are separately used with respect to dynamic phase [115], or ‘absolute phase change’. What is more, these two phases are also directly related with the process of spin-orbital

interaction (SOI) of light [117-120] – an interaction of spin angular momentum (SAM), the intrinsic (IOAM) and extrinsic orbital angular momentum (EOAM) of light [121, 122, 123].

In this thesis, we are mainly concerned with PB-phase and induced SOI process – which are widely appreciated in the rotational symmetric systems [117-120]. The SOI results in spin-orbital angular momentum conversion (SOC) that normally generates vortex beams. When it happens in a symmetry-breaking linear birefringence system, it often leads to the spin-Hall effect of light (SHEL) by consequence of the appearance of circular birefringence in the same system [117-120]. In 2001, *Hasman et al.* presented that the sub-wavelength grating can control the angular momentum (AM) of light – which triggered the design of special optical meta-surfaces that can manipulate the complex process of SOI of light via PB-phase [124, 125, 126]. The SHEL and SOC of light were also demonstrated using such gratings by them (*Hasman et al.*) through structuring the medium [124, 125]. Unfortunately, the fabrication limitation prevented the development of such kinds of grating to be widely used – the induced SOI can only be demonstrated in mid-infrared and near-infrared wavelengths. In 2006, *Marrucci et al*. developed a device that can generate vectorial beams through azimuthally varying PB-phase from a Gaussian beam [127]. Then, they demonstrated the device so called q-plate, which is widely used in current modern classical/quantum optics to convert the SAM to OAM [35]. In 2011, *Shitrit et al.* first observed the SHEL via the experiment with a one dimensional inhomogeneous anisotropic

medium [128]. Subsequently, other devices – such as higher dimensional meta-surfaces have also been reported [129]. All above issues involve with SOI of the light emerging from the space varying PB-phase on a quasi-plane wave beam in various medium. Indeed, huge amount of the research of SOC and its counterpart SHEL have been reported recently that are tightly related with PB-phase and corresponding SOI processes [103].

2.4 Summary and discussion

There is no doubt that the importance of phase and polarisation properties of the light beam spans across most research topics in optics. In this chapter, we first gave a brief introduction of the fundamental mathematical formulism to describe/analyse the light properties. Then, we gave different formula to describe the optical properties of objects that affect the phase and polarisation of the beam. Finally, we gave a brief introduction of two commonly-used instruments for phase sensing and polarisation sensing – interferometer and polarimeter. For the former one, we briefly introduced the fundamental mechanism, system configuration, and the corresponding usage in this thesis – analysing the OAM components. For the later one, we showed the fundamental mechanism difference between Stokes and Müller matrix polarimeter including their system configurations. Specifically, we gave several implementation notes for these techniques. Stokes vector imaging methods and Müller matrix imaging methods for tissue polarimetry were also

introduced. The above mathematical tools and measurement methods play an important role throughout the works in this thesis.

Chapter 3

GRIN lens and its cascade

3.1 GRIN lens formulism and characterization in vectorial field

Following the section 1.3 in Chapter 1, here we show mathematically how the retardance profile of the GRIN lens can be calculated and how the propagation of vector fields through these lenses can be modelled (the equations in this section form the basis for all modelling of the GRIN cascades).

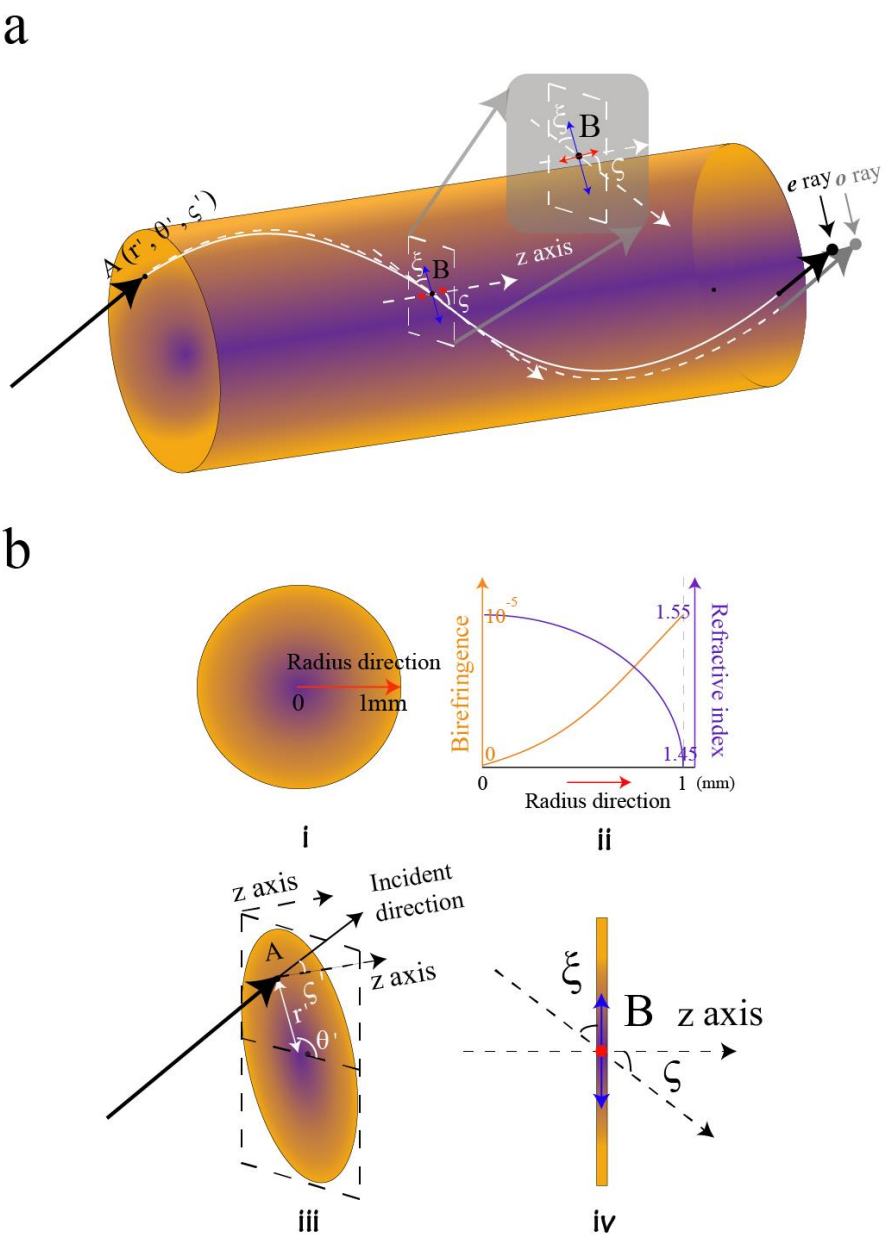


Figure 3.1 Model of the light modulation process by the graded birefringence of the GRIN lens. (a) A specific incident point A is represented by $(r', \theta', \varsigma')$, and the arbitrary point inside GRIN lens along the propagation ray trace is denoted by B (r, θ, ς). The blue double-sided arrow is slow axis direction (extraordinary axis), and the orthometric red counterpart is the fast axis direction (ordinary axis) of that arbitrary point. The black and grey focus points at distal side of the GRIN lens represent focus splitting between the *e* ray (white solid line) and the *o* ray (white dotted line), which is introduced by both the birefringence property and the sinusoid ray trace. (b) (i) the section of a GRIN lens shows the refractive index and the birefringence profiles, (ii) shows two curves of these two parameters along the radius direction from centre point to the boundary of GRIN lens, (iii) shows an incident light on point A$(r', \theta', \varsigma')$,

on the front surface of GRIN lens, referenced by z axis. (iv) shows the lateral profile of one arbitrary section of GRIN lens, which includes a ray trace passing through point B. ξ is the interior angle between the ray and the extraordinary axis (blue double-sided arrow in (a)) at point B, which is the complementary angle to ς, which is the interior angle between the ray and the direction of the z axis.

As we have already illustrated in Chapter 1 (Figure 1.4 and 1.5 of the sketches of ray trace, as well as Eq. (1-2-1), Eq. (1-2-2) and Eq. (1-3-1) for mathematical presentation), for a general ray within the GRIN lens, the distance from the GRIN lens axis is denoted by r, the azimuth of the incident position is denoted by θ, and the interior angle between the ray and the direction of the z axis is denoted by ς. Then a specific incident ray at point A can be expressed in terms of $(r', \theta', \varsigma')$. The mathematical presentation of ray path C, period of the sinusoidal ray trace, the amplitude, and the refractive indices seen by the o rays and e rays have already been given in Chapter 1.

Figure 3.1 (a) illustrates the refractive index (violet coloured gradient), birefringence (yellow coloured gradient) as well as one arbitrary ray trace (white solid line) when light propagates through the GRIN lens. Figure 3.1 (b) (i) and (iii) show the refractive index profile and birefringence profile of a GRIN lens section, and (ii) show sketches of these two parameters along the radius direction from the centre to the boundary (refer to the lens from Femto Technology Co. Ltd., G-B161157-S1484). All the calculations below are under the meridional plane

approximation [21, 22]. The effective refractive index $n_{e'}(r,\xi)$ experienced by the *e* ray at the local coordinates (r, θ, ς) inside the GRIN lens is represented by:

$$n_{e'}(r,\xi) = \frac{n_e(r)n_o(r)}{\sqrt{n_e^2(r)\cos^2\xi + n_o^2(r)\sin^2\xi}}. \quad (3\text{-}1\text{-}1)$$

where ξ is the interior angle between the wave normal and the extraordinary axis (blue double-sided arrow in Figure 3.1 (b) (iv)), which is the complementary angle to ς. Along the sinusoidal ray trace, there will be an accumulated phase difference σ between the *o* rays and *e* rays when the beam reaches the back surface of the GRIN lens. So, there would be a different overall σ dependent on the traced ray *C*.

Importantly, this observation enables us to point out that there also exists a minor beam split between *o* rays and *e* rays due to the birefringence properties of the GRIN lens (shown in Figure 3.1 (b) (i) – *e* ray (white solid line) and the *o* ray (white dotted line)). This affects the axial resolution of the GRIN lens imaging system, as will be explained further in Chapter 4. This splitting is due to the differing sinusoidal optical path lengths of the rays (C_e and C_o respectively). The parameter *A* in Eq. (1-2-1), which is related to the amplitude (and period) of the sinusoidal ray trace, is also different for *o* rays and *e* rays (in practice, the parameter should be represented by A_o and A_e, separately, which are determined by the corresponding refractive index profile, Eq.

(1-3-1)). As the collection of *o* rays and *e* rays inside the GRIN lens are associated with radial and azimuthal linear polarisation eigenmodes, the corresponding linear polarized light fields play a special role in all GRIN lens based systems. Based upon this understanding, we aim to calculate the optical path length difference (*OPLD*) and the phase difference determined by the retardance σ:

$$OPLD(r,\theta,\varsigma) = \int_{C_e}[n_{e'}(s)]ds - \int_{C_o}[n_o(s)]ds \approx \int_C[n_{e'}(s) - n_o(s)]ds. \qquad (3\text{-}1\text{-}2)$$
$$\sigma(r,\theta,\varsigma) = \frac{2\pi}{\lambda}\cdot\int_C[n_{e'}(s) - n_o(s)]ds.$$

Here $n_{e'}(s)$ and $n_o(s)$ are the local refractive indices experienced by e rays and o rays, as a function of distance s along the sinusoidal optical path, as an arc length integral from the original point on the front surface to the exit point on the back surface. Since the birefringence in the GRIN lens is very small, when calculating the accumulated retardance, we can make the approximation that the path of the e rays and the o rays is the same (as shown in Eq. (3-1-2)). We use parallel incident light ($\varsigma = 0$ at z = 0) throughout this work, and as the refractive index and birefringence profiles are rotationally symmetric, if we define the wavelength of the incident beam as λ, Eq. (3-1-2) would allow us to calculate the corresponding σ.

3.2 GRIN lens cascade

In this project, we have drawn upon the previously undesirable GRIN lens property of intrinsic birefringence to build new light manipulation structures to extend the applications of traditional GRIN lens systems (GLS). We call these structures "GRIN lens cascades". This concept runs throughout the whole thesis. As illustrated in Figure 3.2, these cascades comprise one or more GRIN lenses with interstitial optical elements, including polarizers and waveplates (of course, active components can also be considered into this structure as well such as spatial light modulators). Such combinations of elements introduce myriad possibilities for structuring the phase and polarisation profiles of beams and foci. We describe several aspects in this thesis that enable novel extra functionality in GLSs.

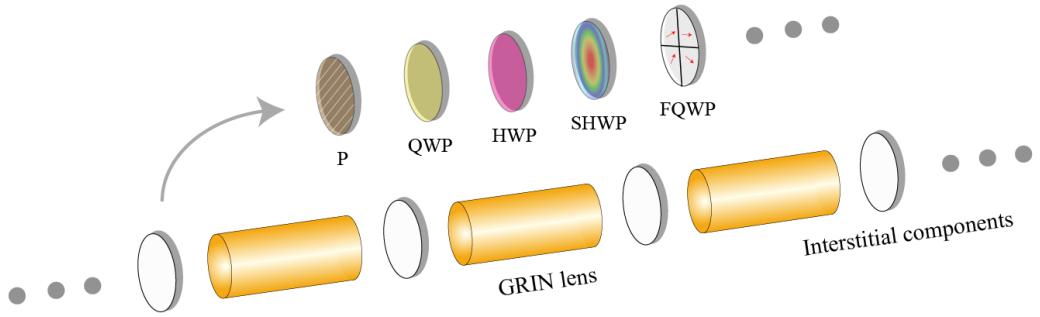


Figure 3.2 GRIN lens cascade. This cascade consists of the combination of one or more GRIN lenses along with various devices including interstitial components – such as P: Polarizer, QWP: Quarter waveplate; HWP: Half waveplate; SHWP: Spatially-variant half waveplate; FQWP: Four quadrant quarter waveplate array with four different fast axis orientations, etc.

We first show that GRIN lenses (and, furthermore, GRIN cascades) can show highly asymmetric Müller matrices (MMs - see details in section 3.4.1). Furthermore, some cascades also exhibit gradients in circular anisotropy, which presents the intriguing possibility that the spin-Hall effect

of light (SHEL) could be harnessed in a GRIN lens based imaging system (see details in section 3.4.2). Secondly, taking advantage of the generation ability of GRIN lens cascades, we show in Chapter 4 that they can generate a multitude of vector vortex beams, and permit the creation of corresponding vector foci. We also demonstrate that, by proper choice of the interstitial optics of the cascade, we can use azimuthal or radial polarisation light fields at the GRIN lens input to enhance axial resolution. Thirdly in Chapter 5 we show how a GRIN cascade forms the basis of a novel single-shot MM polarimeter, which can comprehensively extract the polarisation characteristics of an object. This capability can facilitate GLS based label-free endoscopic diagnosis of structural changes in tissues, with clear applications on cancer detection. Lastly, in Chapter 6, we use adaptive optics to enable new imaging methods of GRIN cascades – preliminary validations in both theory and experiment are given, and future prospects are also discussed (in Chapter 7).

3.3 Basic passive polarisation/phase modulation components characterization

The inner mechanism of the state of polarisation (SOP) modulation of the light beam is the change of its phase and amplitude properties [51]. For the work in this thesis deals we do not need to consider depolarized light or corresponding optical components that have depolarisation

properties, so in this section we mainly introduce two non-depolarizing properties of the object: diattenuation (related to amplitude anisotropy) and birefringence (related to phase anisotropy). This might in practice include linear diattenuation/birefringence, circular diattenuation/birefringence, or indeed a mix of both [51].

3.3.1 Diattenuater

To illustrate the full polarisation properties of a diattenuater and retarder, we use Müller calculus in these sections. The MM of a linear diattenuater (LD) [46-51] is shown below in Eq. (3-3-1).

$$\mathbf{M}_{LD}\left(P,\theta_D\right)=\begin{pmatrix} 1+P & \left(1-P\right)\cos 2\theta_D & \left(1-P\right)\sin 2\theta_D & 0 \\ \left(1-P\right)\cos 2\theta_D & \cos^2 2\theta_D\left(1+P\right)+2\sin^2 2\theta_D\sqrt{P} & \cos 2\theta_D \sin 2\theta_D\left(1-\sqrt{P}\right)^2 & 0 \\ \left(1-P\right)\sin 2\theta_D & \cos 2\theta_D \sin 2\theta_D\left(1-\sqrt{P}\right)^2 & \sin^2 2\theta_D\left(1+P\right)+2\cos^2 2\theta_D\sqrt{P} & 0 \\ 0 & 0 & 0 & 2\sqrt{P} \end{pmatrix}. \tag{3-3-1}$$

where the parameter P is the ratio of relative transmittance of two orthogonal directions, which equals to the ratio of the minimum to the maximum transmittance. θ_D is the azimuthal angle of the dichroism [46-51]. The MM of the circular diattenuater (CD) is shown in Eq. (3-3-2), where the parameter R means ratio of absorption of two orthogonal circular eigenvectors [46-51].

$$\mathbf{M}_{CD}\left(R\right)=\begin{pmatrix} 1+R^2 & 0 & 0 & 2R \\ 0 & 1-R^2 & 0 & 0 \\ 0 & 0 & 1-R^2 & 0 \\ 2R & 0 & 0 & 1+R^2 \end{pmatrix}. \tag{3-3-2}$$

3.3.2 Retarder

The MM of a linear retarder (LR) is shown in Eq. (3-3-3), where δ is the retardance value and θ is the orientation of the fast axis direction of a retarder [46-51].

$$\mathbf{M}_{LR}(\delta,\theta)=\begin{pmatrix}1 & 0 & 0 & 0\\ 0 & \cos^2 2\theta+\sin^2 2\theta\cos\delta & \cos 2\theta\sin 2\theta(1-\cos\delta) & -\sin 2\theta\sin\delta\\ 0 & \cos 2\theta\sin 2\theta(1-\cos\delta) & \sin^2 2\theta+\cos^2 2\theta\cos\delta & \cos 2\theta\sin\delta\\ 0 & \sin 2\theta\sin\delta & -\cos 2\theta\sin\delta & \cos\delta\end{pmatrix}. \quad (3\text{-}3\text{-}3)$$

Similar to the CD, the circular counterpart of LR – a circular retarder (CR)'s MM [46-51] can be found below in Eq. (3-3-4).

$$\boldsymbol{M}_{LR}(\delta=180°,\theta)=\begin{pmatrix}1 & 0 & 0 & 0\\ 0 & \cos 4\theta & \sin 4\theta & 0\\ 0 & \sin 4\theta & -\cos 4\theta & 0\\ 0 & 0 & 0 & -1\end{pmatrix}, \quad (3\text{-}3\text{-}4)$$

It should be noted that, among the above 4 kinds of anisotropy, there exist 6 independent anisotropic parameters P, θ_D, R, δ, θ and φ; the extraction and characterization of them from the MM play a very important role in modern vectorial optics [46-51].

3.4 Optical properties of GRIN lens and its cascade

When aiming to characterize the optical properties of GRIN lens, MM polarimetry and MM decomposition parameters (mentioned in Chapter 2, MMPD etc.) are applied as powerful tools. In this section, we applied MMPD and MMAC parameters to extract polarisation information of GRIN lens and its cascades – to understand their inner optical properties.

3.4.1 Müller matrix and its corresponding decomposition parameters

3.4.1.1 Single GRIN lens: optical properties characterization

Figure 3.3 (a) to 3.3 (c) demonstrate the MMs and the corresponding MMPD parameters of the single GRIN lens cascade. We found that 1) the experimental MM as well as the MMPD parameters match well with the simulation counterparts; 2) the MMPD parameters reveal that the birefringent structure of the GRIN lens behaves equivalently to a spatially-variant waveplate array with a linear retardance that gradually increases along the radial direction and b) fast axis directions that vary azimuthally (gradually changing from $-\pi/2$ to 0 then to $\pi/2$ radians as the azimuthal angle changes from 0 to π radians, then a similar variation when the azimuthal angle changes from π to 2π radians). The fast/slow axis direction distributions are shown in Figure 1 (c) in Chapter 1 as well.

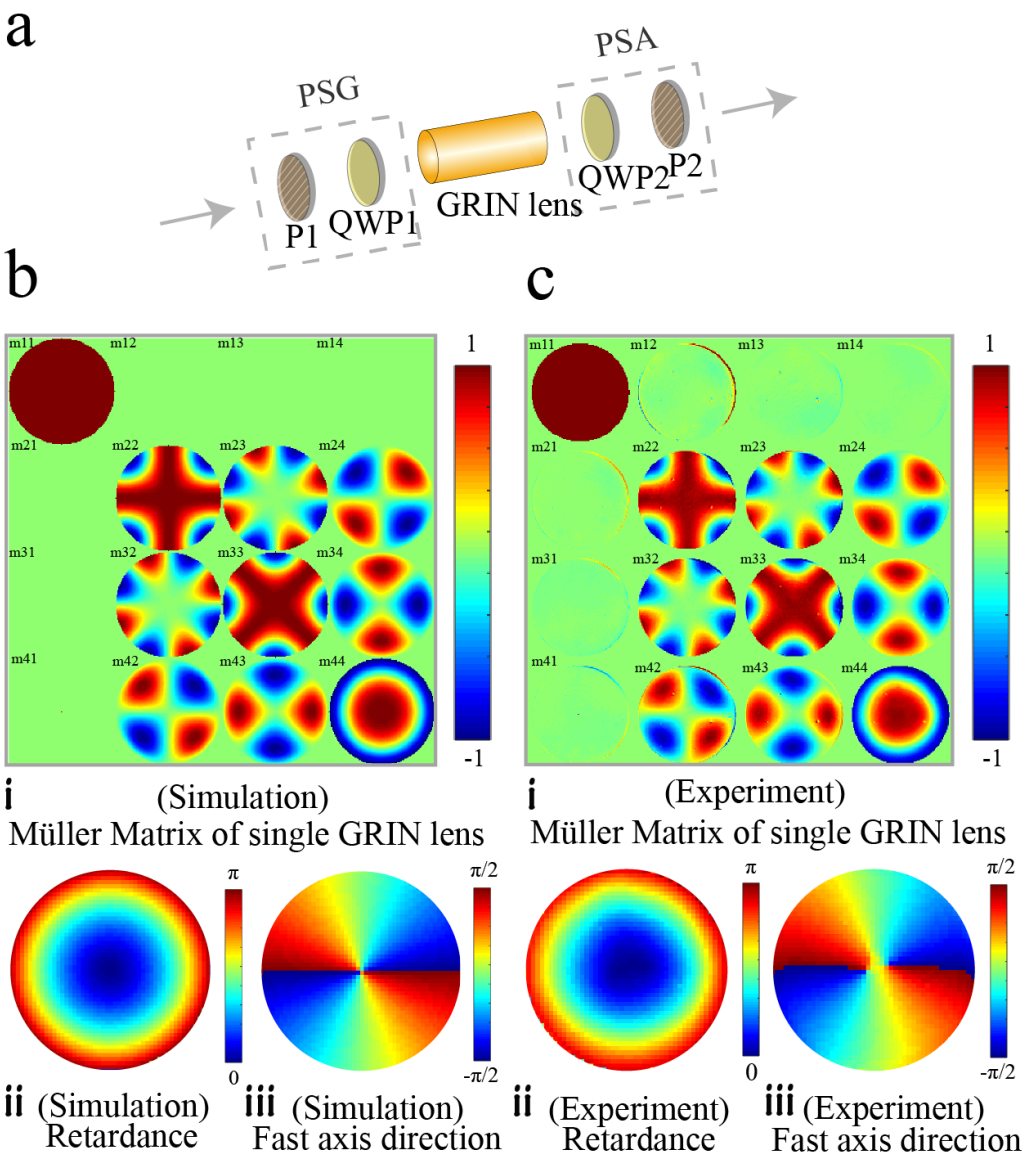


Figure 3.3. Polarization properties of single GRIN lens. (a), (b) and (c) are the schematic of the single GRIN lens cascade and its MM (MM element value range is normalized into -1 to 1), polarization parameters decomposed by MMPD method both in simulation and experiment (the retardance range is from 0 to π radians, and the fast axis orientation range is from -π/2 to π/2 radians). Note that the polarisation state generator (PSG) and polarisation state analyser (PSG) in (a) are used to measure the MM according to the method shown in Chapter 2 [75, 76, 77].

3.4.1.2 Asymmetric properties of Müller matrices of GRIN lens cascade

Spatially-variant half waveplate (SHWP) is a polarization component that has the function of: when combined with appropriate input polarisation, it permits the generation of the azimuthal and radial polarized light fields, see details in Figure 3.4. This component can be used in focus sharping of the GRIN lens imaging systems [31] which we would go details in Chapter 4 and 6. Such cascades (including SHWP) would be interesting in GRIN lens research.

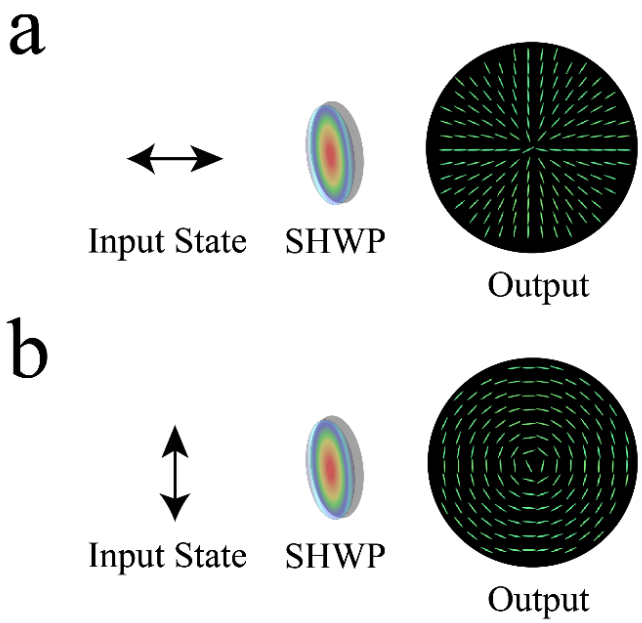


Figure 3.4 Polarisation modulation ability of SHWP. (a) and (b) show the vector vortex beams generated via SHWP using two uniform linear polarised light fields incident, separately.

In Figure 3.5 (a) to 3.5 (d), we further show four different SHWP based GRIN lens cascades. Besides the close correspondence between simulation and experimental results, we also found that the MMs of these GRIN lens cascades have significant off-diagonal asymmetry which is of interest in MM research, as well as related sample information analysis [130]. Specifically, we

extracted the circular anisotropy coefficient (named γ, which has been introduced in section of MMAC parameters in Chapter 2) of these four MMs, shown in Figure 3.5 (e), in which we use grey arrows to indicate the gradient of the circular anisotropy [31, 66]. This implies the system contains symmetric-breaking properties [31]. We will discuss this in detail in the later section to demonstrate further spin-Hall effect of light (SHEL) that is induced by asymmetric properties of the system [31] inside a GRIN lens.

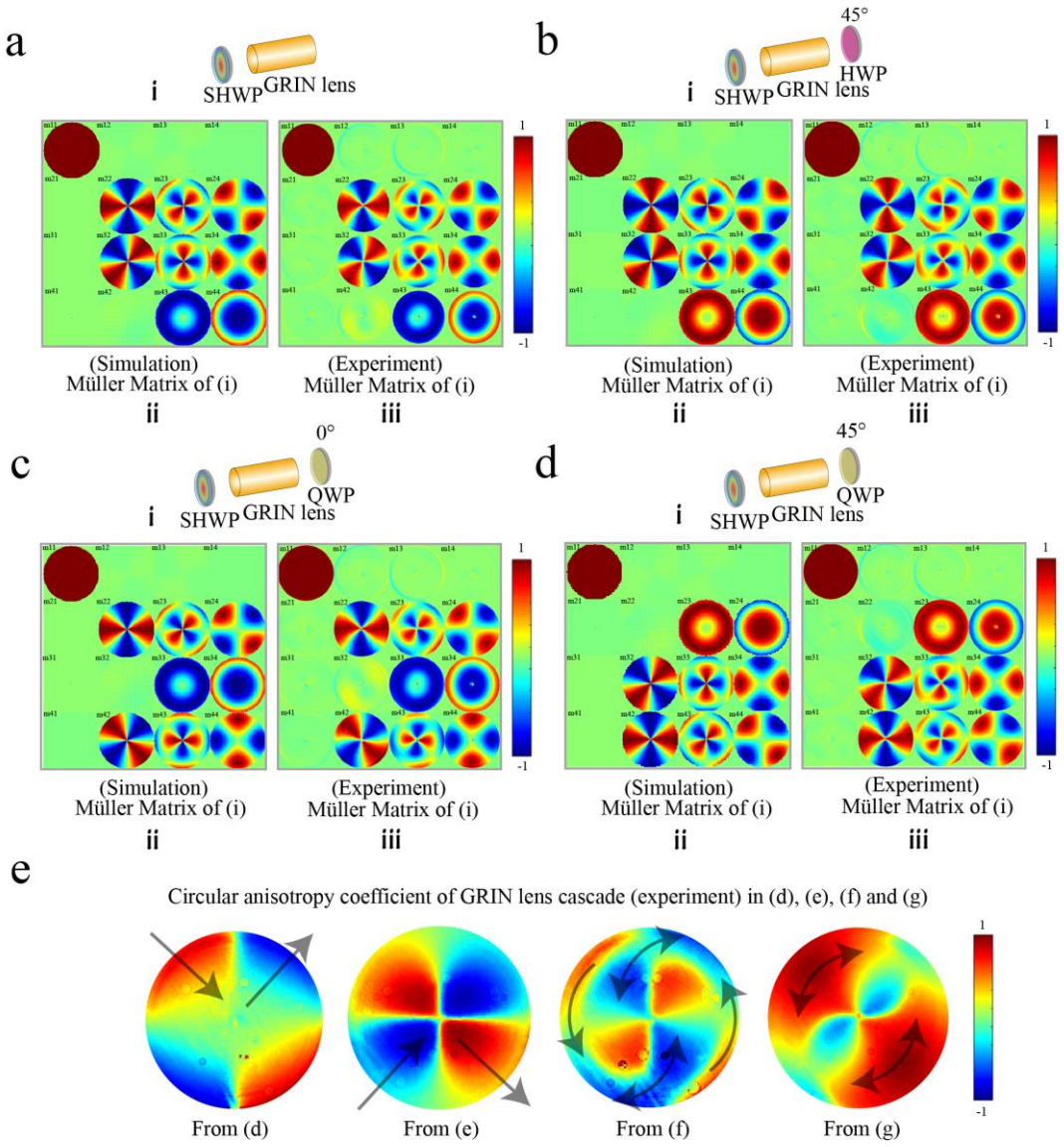


Figure 3.5 Polarisation properties of several GRIN lens cascades. (a), (b), (c), (d) are four different SHWP based GRIN lens cascades (the diagrams omit the PSG and the PSA parts) with their simulated and experimental MMs (MM element value range is normalized into the range -1 to 1). (e) Circular anisotropy coefficient (range is from -1 to 1) of GRIN lens cascade in (a), (b), (c) and (d). The grey arrows indicate the anisotropy gradient.

The above cascades were comprised of multiple linear birefringence layers as the interstitial elements. Of course, our GRIN lens cascades can also be constructed using diattenuators (such as polarizers) as the interstitial elements. Here we further gave some simulation results to show the

strong asymmetric MMs of several diattenuator involved GRIN lens cascades in Figure 3.6 (a) to 3.6 (f). As we can find in Figure 3.6 (a) and 3.6 (b), all the elements in 4th column of the MMs have zero values, including the m14 – which means vanishing of circular diattenuation [130]. In Figure 3.6 (c) and 3.6 (d), the elements in the 3rd and 4th rows of the MMs show zero values, including the m41 – which means vanishing of the circular polarizance [130]. Both of them (symmetric breaking m14 and m41) were used to determine the sequence information of optical elements (diattenuators and/or retarders) of the targeted samples [130]. Figure 3.6 (e) and 3.6 (f) showed that the intensity element m11 can have zero value in some regions of the aperture in such cascades, which might be a phenomenon to help further analyse multiple diattenuators (especially in determining the sequence of diattenuators and retarders [130]). To our surprise, there is a kind of asymmetric MM in Figure 3.6 (e) which contains zero value both in some rows and column simultaneously. All of these phenomena would be interesting in the characterization of multi-layered birefringence and diattenuation (especially mixed systems). This is of great interest in MM fundamental research as well [130] and deserves further exploration. These all take advantage of the unique property of the GRIN lens – its equivalence to a complex spatially variant waveplate array, which can encompass all combinations of retardance and fast axis direction.

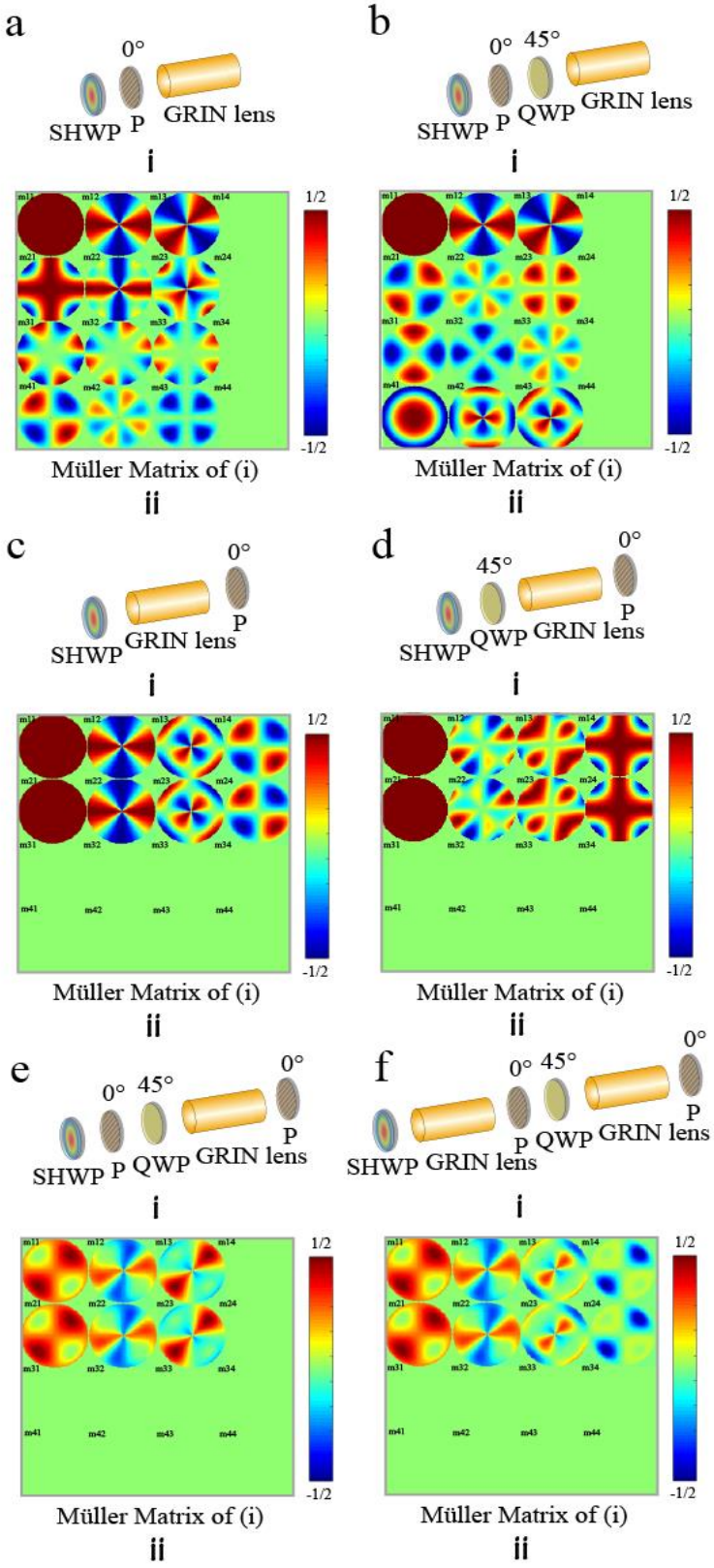


Figure 3.6 Polarisation properties represented by MMs of several GRIN lens cascades. (**a**), (**b**), (**c**), (**d**), (**e**) and (**f**) are the schematics of the diattenuator involved GRIN lens cascades and their MMs (range is from -0.5 to 0.5), which showed highly asymmetric properties.

3.4.2 Spin-Hall effect of light inside GRIN lens

It is widely appreciated that in rotational symmetric system, the spin orbital interaction (SOI) results in spin-orbital angular momentum conversion (SOC) – normally generates the vortex beams [117-120]. In a symmetry breaking system, the SOI process leads to spin-Hall effect of light (SHEL) – can be validated by the occurrence of circular birefringence [117-120]. In this section, we break the symmetry of the GRIN lens system by simply applying a tiny tilt on the GRIN lens – equivalently leads to a collimated, oblique incident light illuminated GRIN lens system – that also in effect changes its original birefringence distribution to demonstrate the SHEL.

3.4.2.1 Single GRIN lens cascade: oblique incident induced symmetric breaking

It should be noted that within the oblique incidence arrangement (determined by numerical aperture (NA) of the specific GRIN lens), the SHEL occurring in GRIN lens relies on the change of illumination angle. Also, due to GRIN lens's imaging ability, the lens also has great potential to be a field-controllable imaging SHEL device – a kind of instrument that is gradually drawing attention [66].

MM and its decomposition parameters have been used previously for mapping the complex topological structures of fast axis variation crystals and validating the appearance of SHEL by

analysing the circular anisotropy coefficient (which is directly related with circular birefringence) [66]. It is an alternative but powerful method to validate SHEL when weak SHEL occurs due to complex Pancharatnam-Berry phase gradient across the beam transverse plane – where traditional standard quantum weak measurement methods and Stokes vector analysis method are not suitable for application [66].

Of course, our observation in this work also suffers from the challenges of mathematical modelling for the ray trace and retardance accumulation process inside the GRIN lens, as the meridional plane approximation can never be applied in the situation of oblique incidence [19, 20, 21]. However, similar to the SHEL research in Potassium Dihydrogen Phosphate (KDP) crystals, where previous researchers also only demonstrated the important experimental phenomenon rather than mathematical explanations [66], we believe the demonstration of this important feature of those commonplace optical transmitters would also benefit various applications.

A GRIN lens has a spatially variant birefringence such that its fast axis is azimuthal distribution can be treated as a spatial variant waveplate array not only in the section of its thin slice but also in an overall performance [31], as explained in Chapter 1. Here, we first use a long GRIN lens (Femto Technology Co. Ltd., NA=0.25) to demonstrate the SHEL that can be harnessed by

oblique illumination via single GRIN lens cascade. Figure 3.7 shows the sketch of oblique illumination. The incident angle Φ is set from 5 to 10 degrees, with a 1 degree interval.

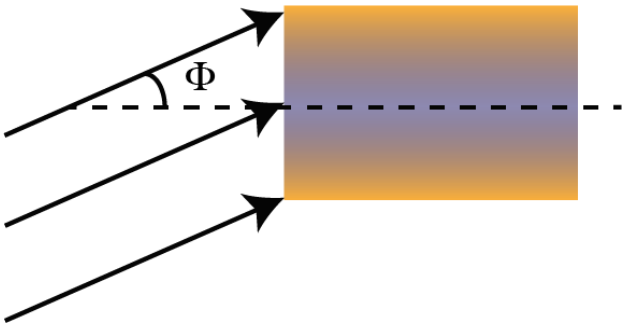


Figure 3.7 Sketch of oblique illuminated GRIN lens via collimated light beam. The parameter Φ is a variable. During the experiments, we tested 5 to 10 degrees of the incident angle (with 1 degree interval) with recorded MMs to do further analysis.

3.4.2.2 Circular anisotropy coefficient of single GRIN lens

We extracted the full polarisation properties of the GRIN lens via different MMs obtained using different incident angles. Then we calculated the MMPD and MMAC parameters to analyse the inner mechanism of the related SOI processes. Figure 3.8 show the results of different MMs (see Figure 3.8 (a)), different retardance values (see Figure 3.8 (b)) and spatial variant fast axis distributions (see Figure 3.8 (c)) derived from the corresponding MMs.

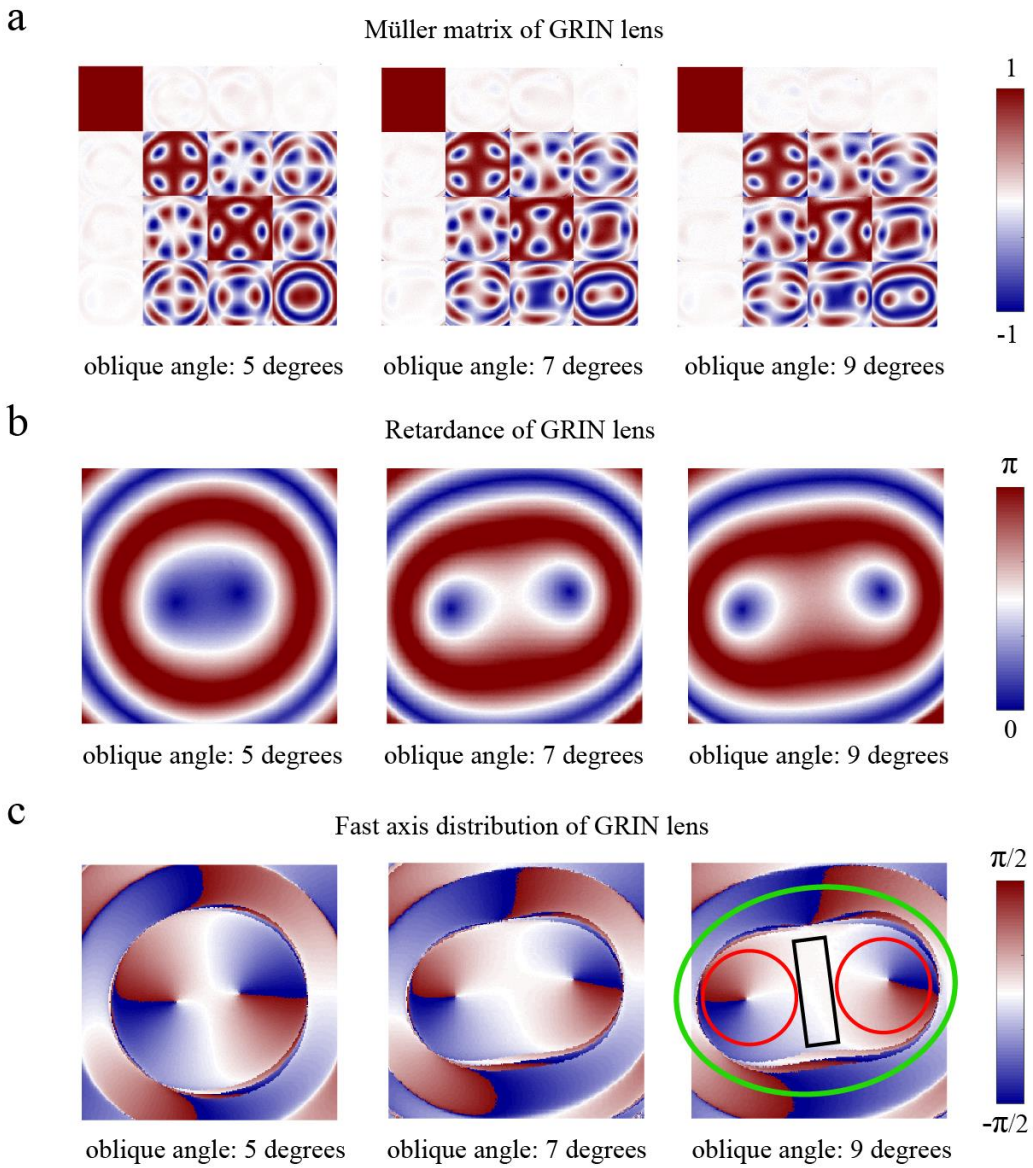


Figure 3.8 Experimental results. (**a**) MMs (MM element value range is normalized into the range -1 to 1) of GRIN lens with different tilted angle; (**b**) retardance properties of the GRIN lens (the retardance range is from 0 to π radians); (**c**) fast axis properties of the GRIN lens (the fast axis orientation range is from -π/2 to π/2 radians). They are demonstrated at incident angle Φ of 5, 7 and 9 degrees. The green circle, red circle and black box rectangle represent different topological charge units [131-134].

To reveal the inner SOI process at different incident angle, we thus focus on the analysis of retardance performance (see Figure 3.8 (b)) and the related fast axis orientation profiles (see

Figure 3.8 (c)), which govern the SOI process of a birefringence system [135, 136]. The process can be expressed by the point of view of angular momentum (AM) conversion.

It should first be clarified that the photons inside GRIN lens are partially converted during the SOI process, limited up to an efficiency factor μ [66, 137] due to the gradually changing retardance profile of GRIN lens, as the similar case in KDP [66, 137]. In later points we assume that all photons have been filtered by a polarisation state analyser to keep the full conversion.

When a photon carrying spin angular momentum (SAM) (such as right hand polarized, carries total AM (TAM) J = +1ħ, consisting of SAM σ = +1ħ and OAM l = 0ħ) passes through a GRIN lens, the interaction in the node topological area [131-134] in Figure 3.8 (c) converts SAM handedness of the photon into σ = -1ħ. The TAM is changed by a SAM induced factor +2ħ, where the SAM completely transfers in to intrinsic OAM (IOAM).

When a tilt is applied, the rotational symmetry of the birefringence distribution is broken (manifested in Figure 3.8 (b) and (c)). This would significantly change the SOI process, since then there exist three different topologies rather than the original one. From Figure 3.8 (c) (when

the incident angle is 9 degrees) we could clearly find two lemons (around red circles), a node (around green circle), and one linear gradient (around black rectangle) at the intermediate region.

For the node region, the SOC performs as discussed above; and for the lemon region (which are newly formed) [138], they would gain an IOAM of +1ħ. So, considering the whole field, due to the TAM conservation mechanism, the remaining +2ħ is expected to transfer into the medium – which is comparable with the SOI process in KDP [66].

The linear gradient areas (near lemon region, gray rectangle) are not associated with any azimuthal/radial coordinate [66, 137]. So, for such a beam-field the photons passing through this region would neither obtain IOAM nor involve with any SOC. However, the linear variation of the Pancharatnam-Berry phase in these areas makes the photon have an additional IOAM due to the validation of the circular anisotropy coefficient extracted along with the fast axis direction from measured MMs (shown in Figures 3.8 and 3.9), which validated the existence of the SHEL (i.e., the spatial walk off of two opposite spin states).

We then do some quantitative validations of the gradually stronger SHEL via analysis the circular anisotropy coefficient at different illumination angle. The process is: 1) we first chose three fixed

concentric circles on the GRIN lens surface (shown in Figure 3.9 (a)) near the linear gradient region; 2) at every angle, we obtained the data from the value of circular anisotropy coefficient of three circles; 3) then we calculated the mean value and standard deviation through statistical methods [139]; 4) then collected data from different angles and formed the Table 3.1 and Figure 3.9 (b).

And as we can find in Table 3.1 and Figure 3.9 (b) below that with larger incident angle, there exist higher values of circular anisotropy coefficient. To our best knowledge, this is the first report that the SHEL may be harnessed in GRIN lens systems via MM analysis.

Table 3.1 Circular anisotropy coefficient value with different illumination angle

	5 degree	6 degree	7 degree	8 degree	9 degree	10 degree
Mean value	0.107	0.153	0.212	0.246	0.281	0.324
Standard derivation	0.015	0.013	0.016	0.017	0.020	0.021

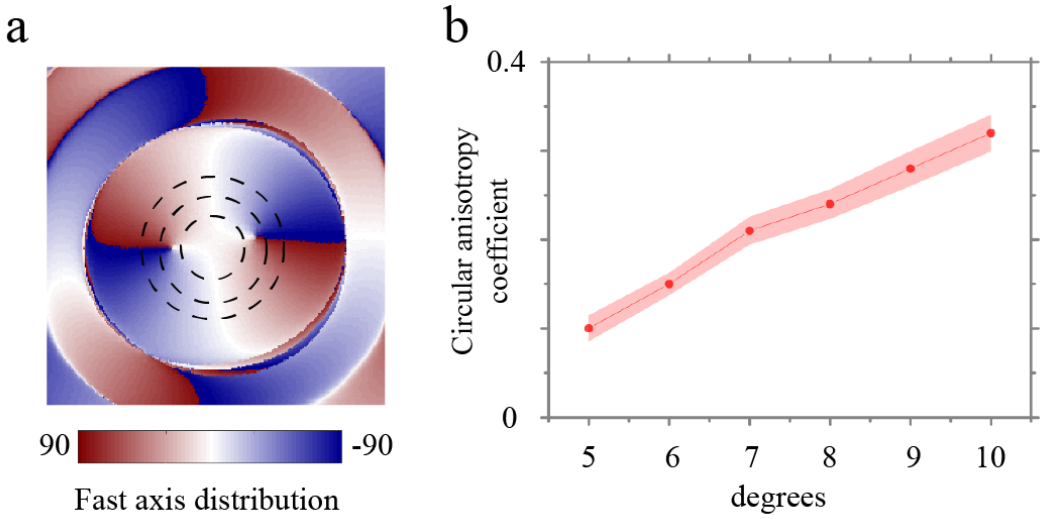


Figure 3.9 Circular anisotropy coefficient extracted from the measured MMs. The values of five points reflect the mean value and standard deviation of circular anisotropy coefficient that measured under conditions of different oblique illumination angles: 5, 6, 7, 8, 9 and 10 degrees. (a) The three fixed circle regions chosen from fixed GRIN lens surface are shown in dotted circles. (b) The solid red circle points represent the mean values that calculated from the circular anisotropy coefficient values from every three circles, and the pink areas represent the standard deviation of the data from three circles that obtained at every fixed illumination angle.

Overall, we reported in this section about the possibility of harnessing SHEL in a GRIN lens by breaking the symmetry of the system. It is field-controllable and provides extra degrees of freedom of SHEL taking advantage of polarisation properties of a tilted GRIN lens system. It should be pointed out that the GRIN lens still maintains its basic function of imaging. So, there is no doubt that the GRIN lens is functional as an imaging SHEL device, which has already attracted lots of interests in quantum optics and in classical optics such as the application of boundary detection [140]. We believe there exists a wider scope for harnessing the SHEL (and more complex geometric phase related effect) from GRIN lens and its cascade.

3.5 Summary and discussion

In this chapter, we put forward the main novelty of this thesis – GRIN lens cascade – to enable extra functionalities in common place GRIN lens systems. Then, we first focused on characterizing the polarisation properties of the GRIN lens itself from theory to experiment, with an emphasis on analysing its retardance and fast axis distribution; then we explained two new uses of the GRIN lens cascade taking advantage of the optical properties of themselves – 1) asymmetric properties of MMs of GRIN lens cascade and 2) SHEL in GRIN lens. We gave experimental data and had a discussion for both with detailed analysis the circular anisotropy coefficient of single GRIN lens (and related SOC and SHEL processes). We believe that further GRIN lens cascade can also find use as a special device for other research areas, such as the derivation of quantitative MM parameters from exotic materials (e.g. chiral characteristics), biomedical research (multi-layered birefringence and/or diattenuation characterization), or studies on complex SOI processes of light [66, 70, 130]. However, in the next Chapter, we will focus on the generation and analysing properties of those birefringence channels to open new applications for GRIN lens cascades.

Chapter 4

Vectorial beam generation through GRIN lens cascade

4.1 Vectorial beam generation

Great interest has developed in vector light fields that contain complex phase and polarisation structures, whether in the focal or pupil domains. Of especial interest are those containing singularities, as they promise unprecedented capabilities for applications ranging from classical to quantum optics [141-157]. Examples include various complex vector beams (VB) that have non-uniform polarisation distribution across the transverse plane [141, 145, 147], beams with helicoidal wave fronts that carry orbital angular momentum (OAM) [142, 144] and their combinations as vector vortex beams (VVB) [31, 34]. Currently, such beams can be generated by using a range of modulation devices, such as spatial light modulators, q-plates, metasurfaces, segmented waveplates or Fresnel-reflected cones [141-157]. We present here further options enabled by the birefringence of GRIN lenses especially for their usage in GRIN lens systems

(GLSs). The focussing properties of the GRIN lens arise due to the refractive index led dynamic phase that accounts for the sinusoidal ray trace using scalar theory. However, the birefringence means that vector effects must be considered. Furthermore, the lens is capable of manipulating light through the introduction of a geometric Pancharatnam-Berry phase (PB-phase) [141]. To the best of our knowledge, this is the first time that the PB-phase and its corresponding effects have been studied in GLSs.

4.1.1 Vector beam

4.1.1.1 Singular vector beam – full Poincaré beam

VB have attracted great interest in a wide range of applications that take advantage of their structured polarisation [141, 142]. They can be used to control the focus in microscopy, for the demonstration of Möbius band-like topologies, for electron acceleration and for material processing [141-157]. Of particular interest are singular VBs where the polarisation distribution in the beam cross section has a vectorial singularity, such as a C-point (where the orientation of the polarisation ellipse is undefined) or an L-line (where its handedness is indeterminate) [150, 151, 152]. There is one class of singular VBs called the full Poincaré beam, in which the polarisation structure spans the full Poincaré sphere, which are of great interest in many areas of research [150, 151, 152]. Here we first characterize the VB components generated by GRIN lens cascade.

4.1.1.2 Polarisation singularities – single GRIN lens characterization

Following the characterization of the GRIN lens polarisation properties using the MM in Chapter 3, the properties can equivalently be represented by the Jones matrix as:

$$J_{\mathrm{GRIN}} = \begin{bmatrix} \sin^2(\theta) + \epsilon\cos^2(\theta) & (\epsilon-1)\sin(\theta)\cos(\theta) \\ (\epsilon-1)\sin(\theta)\cos(\theta) & \cos^2(\theta) + \epsilon\sin^2(\theta) \end{bmatrix}, \tag{4-1-1}$$

where $\epsilon = \mathrm{e}^{\mathrm{i}\sigma} = \cos(\sigma) + \mathrm{i}\sin(\sigma)$, and the desired retardance profile $\sigma = f(r) \propto n_{\mathrm{e}}(r)$ (refer to Chapter 3 for information about $f(r)$ and $n_{\mathrm{e}}(r)$ of the GRIN lens). Here, θ is the slow axis direction of the equivalent waveplate, which is equal to the angle in the cylindrical-coordinate system, r is the radius, σ is the effective cumulative retardance at position $(r,\ \theta)$. If a state of polarisation (SOP) incident on the GRIN lens is described by Jones vector $E_{\mathrm{in}} = [\cos\phi, \mathrm{e}^{\mathrm{i}\delta}\sin\phi]^{\mathrm{T}}$, where the parameters ϕ and δ determine the polarisation state, then the output polarisation beam profile E_{out} is given by $E_{\mathrm{out}} = J_{\mathrm{GRIN}} \cdot E_{\mathrm{in}}$. This can be also represented by Eq. (4-1-2):

$$\begin{bmatrix} f_1(\phi,\delta,\theta,\sigma) \\ f_2(\phi,\delta,\theta,\sigma) \end{bmatrix} = \begin{bmatrix} \sin^2(\theta) + \epsilon\cos^2(\theta) & (\epsilon-1)\sin(\theta)\cos(\theta) \\ (\epsilon-1)\sin(\theta)\cos(\theta) & \cos^2(\theta) + \epsilon\sin^2(\theta) \end{bmatrix} \cdot \begin{bmatrix} \cos\phi \\ \mathrm{e}^{\mathrm{i}\delta}\sin\phi \end{bmatrix}, \tag{4-1-2}$$

where functions $f_1(\phi,\delta,\theta,\sigma)$ and $f_2(\phi,\delta,\theta,\sigma)$ determine the output VB. As for the case in Figure 4.1 (a), when we apply Eq. (4-1-2) to a right hand circular polarised incident beam, $E_{\mathrm{R}} = \frac{1}{\sqrt{2}}[1, \mathrm{i}]^{\mathrm{T}}$, it can be easily validated that when $\sigma = \pi$, the polarisation states of the

generated beam vary from right-hand circular (at the centre) to left-hand circular (at the outermost ring). Thus, the polarisation state of the field $[\, f_1(\phi,\delta,\theta,\sigma)\,, f_2(\phi,\delta,\theta,\sigma)\,]^{\mathrm{T}}$ gradually varies across the transverse plane from the centre to the outermost boundary such that the field contains all polarisation states. This validates that the single GRIN lens cascade can produce a full Poincaré beam for any pure input state of polarisation (SOP). Eq. (4-1-2) can be similarly used to simulate the effects of other input polarisation states. We demonstrated this ability further by using the same single GRIN lens cascade (see Figure 4.1 (a) below). Figure 4.1 (a) (ii) shows polarisation singularities in the full Poincaré beam (with topological index [131-134] η=1), which features C-point and an L-line. The corresponding mapping is shown in Figure 4.1 (a) (iii). A quantitative comparison example for demonstration is presented in Figure 4.1 (a) (iv). The simulation and experimental data are from the beam in Figure 4.1 (a) (ii). A sample distribution of polarisations along the L-line [131-134] is chosen in order to illustrate the quality of fit; the demonstration on the Poincaré sphere is also given. The mean errors of parameters S'_1, S'_2 and S'_3 were 1.8%, 2.1% and 2.7% respectively (normalized by S'_0). The mean value is calculated through the following progress: a) taking S'_1 as an example, we first calculate mean value bias (M) of every point such as point n (n=1,2,3…) by $M_n = |S_{1n}\text{-}S'_{1n}/S_{1n}|$; b) adding all the mean value of every point and calculating an overall mean value, i.e., value $S'_1 = (M_1+M_2+M_3 \ \ldots \ M_n)$/n; c) S'_2 and S'_3 are calculated through the same process. It should be pointed out that the precision benefits from the

highly-symmetric birefringence, which is a consequence of the highly symmetric refractive index generated in the manufacturing process. That deserves further exploration, especially if seeking to use GRIN optics as a beam generator for applications that require highly symmetric beams. More examples of beam generation under this cascade are shown in Figure 4.1 (b) through simulation and experiment, which show close correspondence.

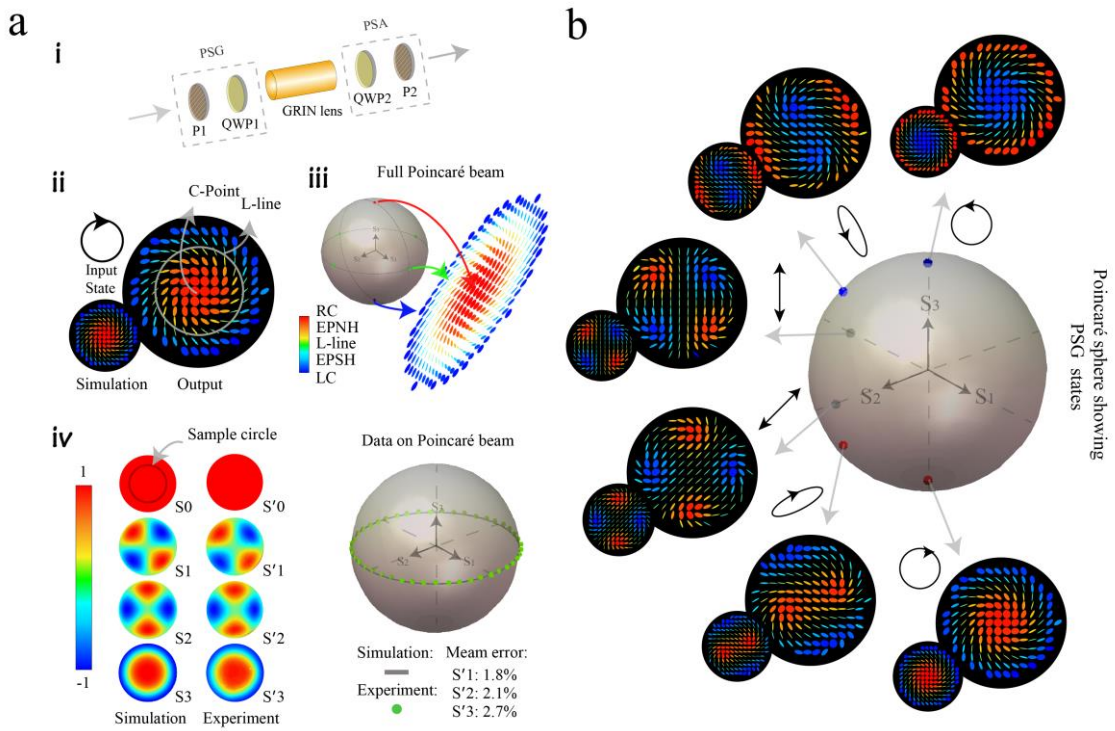


Figure 4.1 Polarisation light field generation and characterization. (a) (i) Schematic of a single GRIN lens. P1 and P2: fixed polarisers with transmission axis at 0°. QWP1 and QWP2: rotated quarter wave plates. Before the GRIN lens is a PSG that includes P1 and QWP1 to generate a chosen arbitrary polarisation state. Following the GRIN lens is a PSA, including P2 and QWP2, which enables Stokes vector measurement. (ii) shows a full Poincaré beam generated by right hand circular input, and its C-point and L-line. The colour bar represents: red side of the colour scale indicates right hand circular (RC) and elliptical polarised light on northern hemisphere (EPNH) of the Poincaré sphere, whereas blue corresponds to left hand circular (LC) and elliptical polarised light on southern hemisphere (EPSH) of the Poincaré sphere. The rest are all linear polarised light on the equator – comprising the L-line. The projection of this beam onto Poincaré sphere are demonstrated in (iii). (iv) Stokes vector distribution of the vector beam in (ii) with

both simulated and experimental data, alongside the data distribution on the Poincaré sphere. A sample distribution of polarisations along the L-line is chosen for quantitative comparison. The mean measurement errors of parameters S'_1, S'_2 and S'_3 are given (normalized by S'_0). The range of the value is from -1 to 1. (b) Beam generated by a single GRIN lens. Five input SOPs generated by the PSG are illustrated (including linear, circular and elliptical states) and shown on the Poincaré sphere. Patterns of polarised light fields in the larger circles represent experimental results and the smaller circles are simulation results.

4.1.1.3 Complex polarisation singularities characterization in GRIN lens cascade

This concept can be extended further. Higher order GRIN lens cascades – those containing more than one GRIN lens, which may or may not be the same – are able to create even more complex VBs, as shown in Figure 4.2 (a) to 4.2 (f). These results reveal that higher order cascades can generate complex polarisation fields that have variations in radial or azimuthal directions, or encompass multiple sub-beams, each of which constitutes a full Poincaré beam; each of these Poincaré beams could have different topological charge or handedness, as well as beam profile (see some analysis in later paragraphs). The beams also contain different complex phase profiles; in section 4.1.2 we illustrate further this phase manipulation ability.

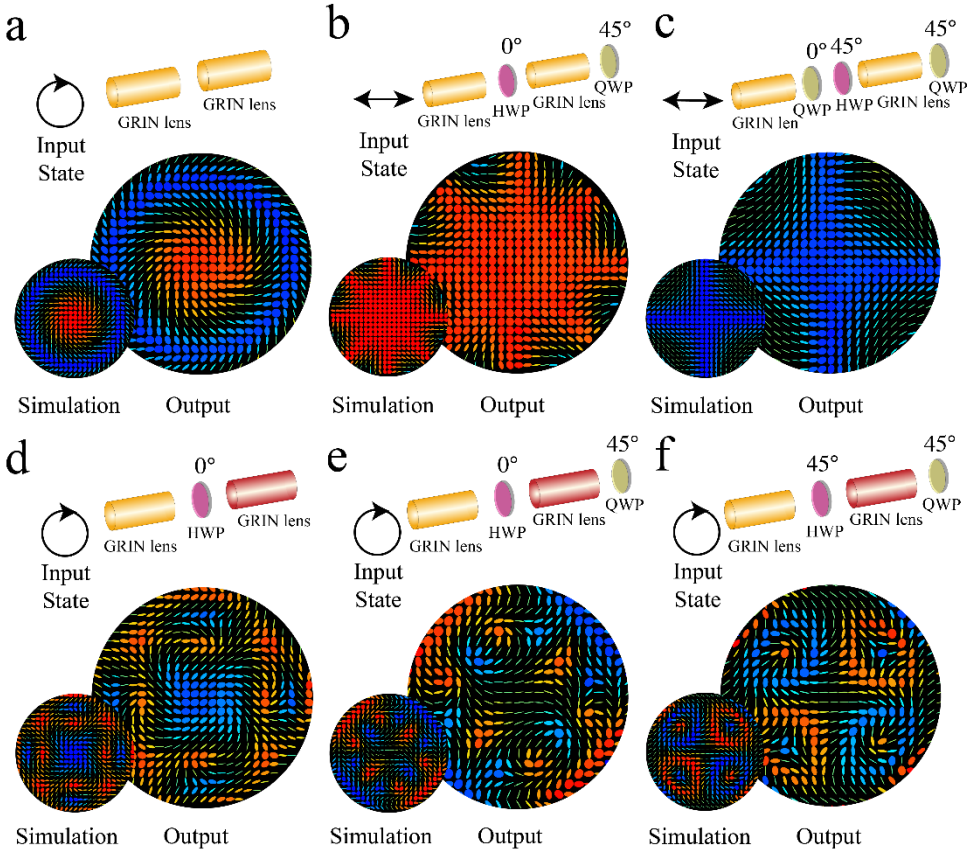


Figure 4.2 VBs generation through GRIN lens cascades. (a), (b), (c), (d), (e) and (f) show higher-order GRIN lens cascades and their generated light fields under specific inputs. Schematic of GRIN lens cascade with right hand circular or horizontal linear input, output polarisation fields for both simulation and experimental results (the red side of the colour scale indicates right hand circular, whereas blue corresponds to left hand circular). Note that before the GRIN lens cascade there is a polarisation state generator (PSG) to generate a chosen arbitrary polarisation state; following the GRIN lens is a polarisation state analyser (PSA) that enables Stokes vector measurement (see method in Chapter 2), like in Figure 4.1 (a) (i). The PSG and PSA parts are omitted for clarity. In (e), (f) and (g) the red-coloured GRIN lens indicates another GRIN type with a larger magnitude retardance profile almost equivalent to a sequence of three of the first (orange) type of lens (for details see Figure 4.3 and corresponding descriptions).

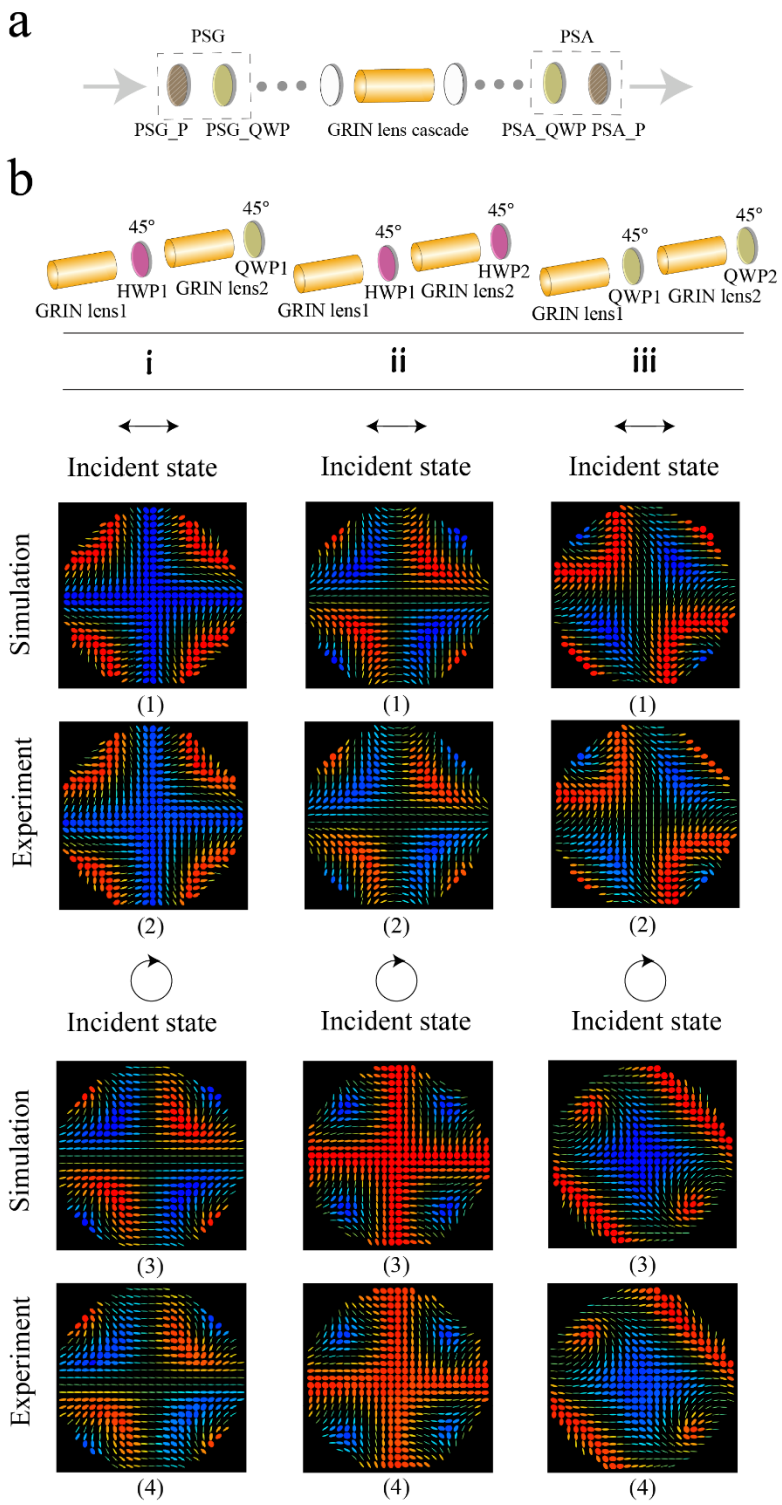
Further demonstration and analysis of representative higher-order VBs generated by different cascades – with different combinations of waveplates and different GRIN lenses, can be found in Figures 4.3 and 4.4. It should be noted that an infinite range of cascades can be created, not only

through different sequences of GRIN lenses and waveplates, but also through variation of the retardance and fast axis directions of the waveplates.

As a first demonstration, Figure 4.3 shows some higher order VBs generated by different kinds of dual GRIN lens cascades, which include two identical GRIN lenses. Figure 4.3 (a) gives an overall view of all cascades considered in this section. In addition to the cascade, the experimental system includes a PSG and a PSA, which are used respectively to generate variable uniform incident polarised light fields and to measure the VBs.

Secondly, we used cascades including two different GRIN lenses. The second of the two lenses had a larger magnitude retardance profile, such that it was almost equivalent to a sequence of three of the first type GRIN lens; this is illustrated in Figure 4.4 (a). The different retardance profile of the second GRIN lens means that different types of VB can be generated. We then applied the similar interstitial optical element combinations as used in Figure 4.3 (b), (c) to Figure 4.4 (b), (c) to generate new VBs from the new GRIN lens cascades. Results are shown in Figure 4.4 (b) and 4.4 (c).

Figures 4.3 (b), 4.3 (c) and Figures 4.4 (b), 4.4 (c) show both simulation and experimental results under horizontal linear and right hand circular polarisation state incident cases. The following observations can be made from the results: 1) the experimentally measured VBs match well to the theoretical calculations; 2) a wide range of VBs can be produced using different cascades VBs; 3) the GRIN lens cascades are able to generate high radial order VBs; 4) the GRIN lens cascades are able to create high azimuthal order VBs.


a
PSG
PSA
PSG_P
PSG_QWP
GRIN lens cascade
PSA_QWP
PSA_P
b
45°
HWP1
GRIN lens2
QWP1
GRIN lens1
HWP2
QWP2
i
ii
iii
Incident state
Simulation
Experiment
(1)
(2)
(3)
(4)

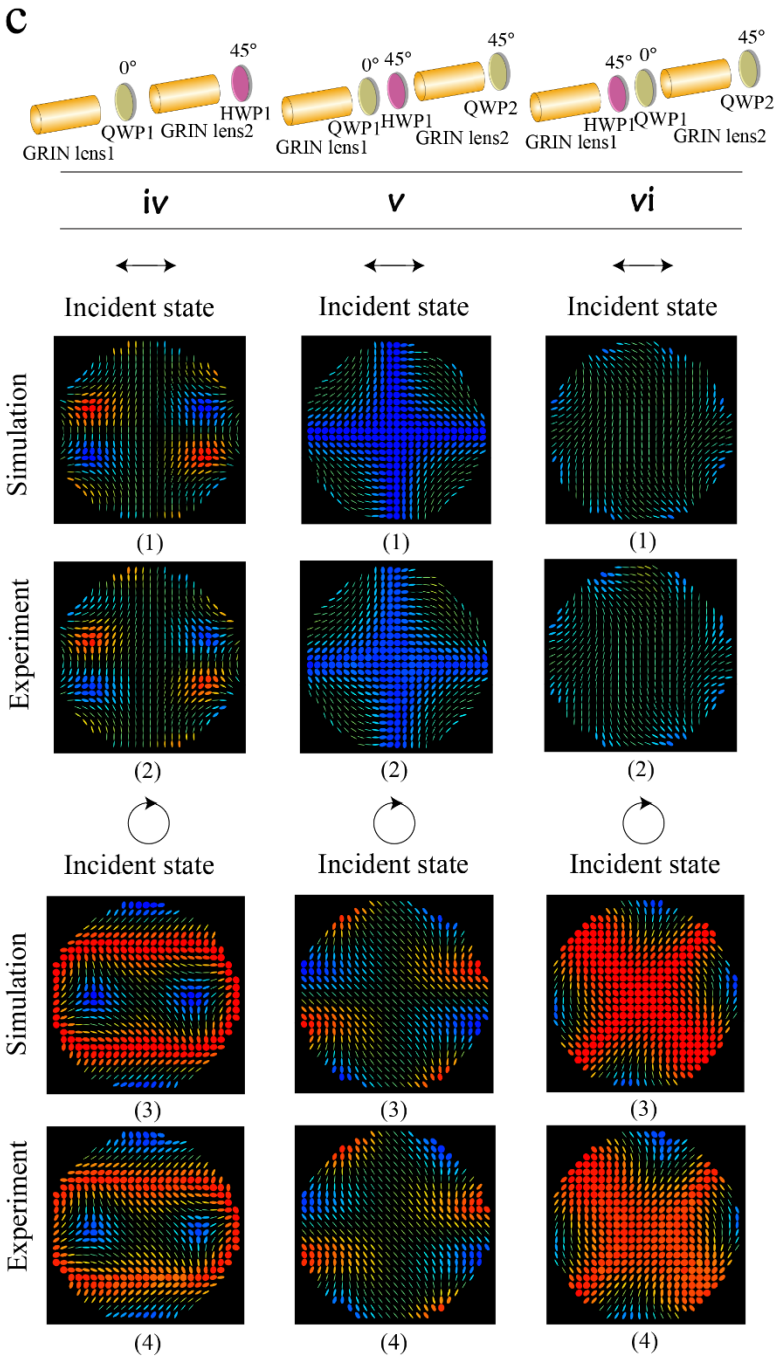
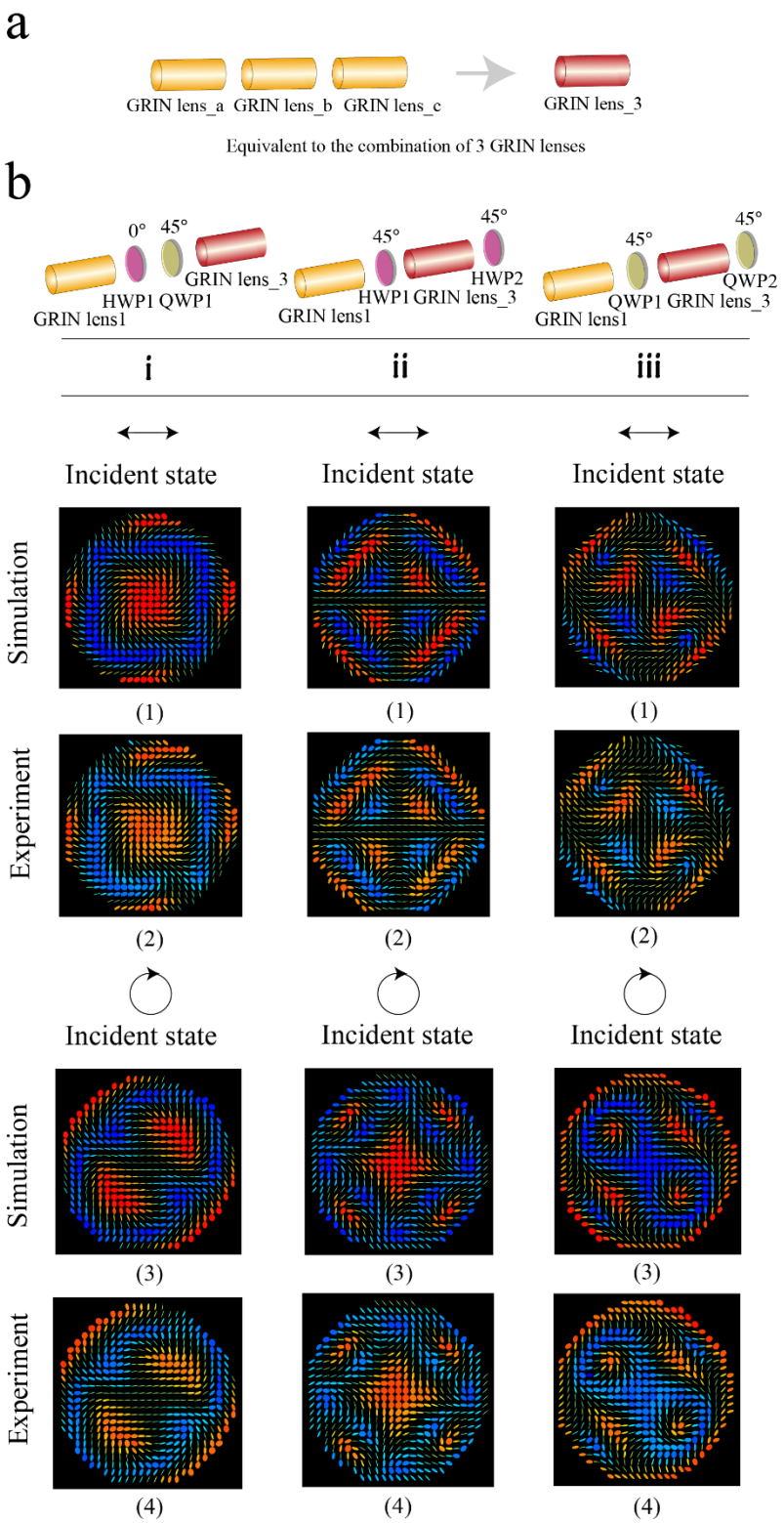


Figure 4.3 VB patterns generated by dual GRIN cascades employing two identical GRIN lenses. (a) the cascade preceded by a PSG and followed by a PSA: the PSG part with PSG_P (polariser) and PSG_QWP (quarter waveplate); the PSA part with PSA_QWP (quarter waveplate) and PSA_P (polariser). These two parts are not shown in subsequent cascades in this section; (b) and (c) are composed of three different cascade structures for each ((i) to (iii) and (iv) to (vi)). The rows for all sub-pictures of (1) and (2) are generated using horizontal linear polarised incident light; (3) and (4) are generated using right hand circular incident light. (1), (3) are simulation results and (2), (4) are experimental counterparts.


a
GRIN lens_a
GRIN lens_b
GRIN lens_c
GRIN lens_3
Equivalent to the combination of 3 GRIN lenses
b
0°
45°
GRIN lens_3
HWP1
QWP1
GRIN lens1
45°
45°
HWP2
HWP1
GRIN lens_3
GRIN lens1
45°
45°
QWP2
QWP1
GRIN lens_3
GRIN lens1
i
ii
iii
Incident state
Incident state
Incident state
Simulation
(1)
(1)
(1)
Experiment
(2)
(2)
(2)
Incident state
Incident state
Incident state
Simulation
(3)
(3)
(3)
Experiment
(4)
(4)
(4)

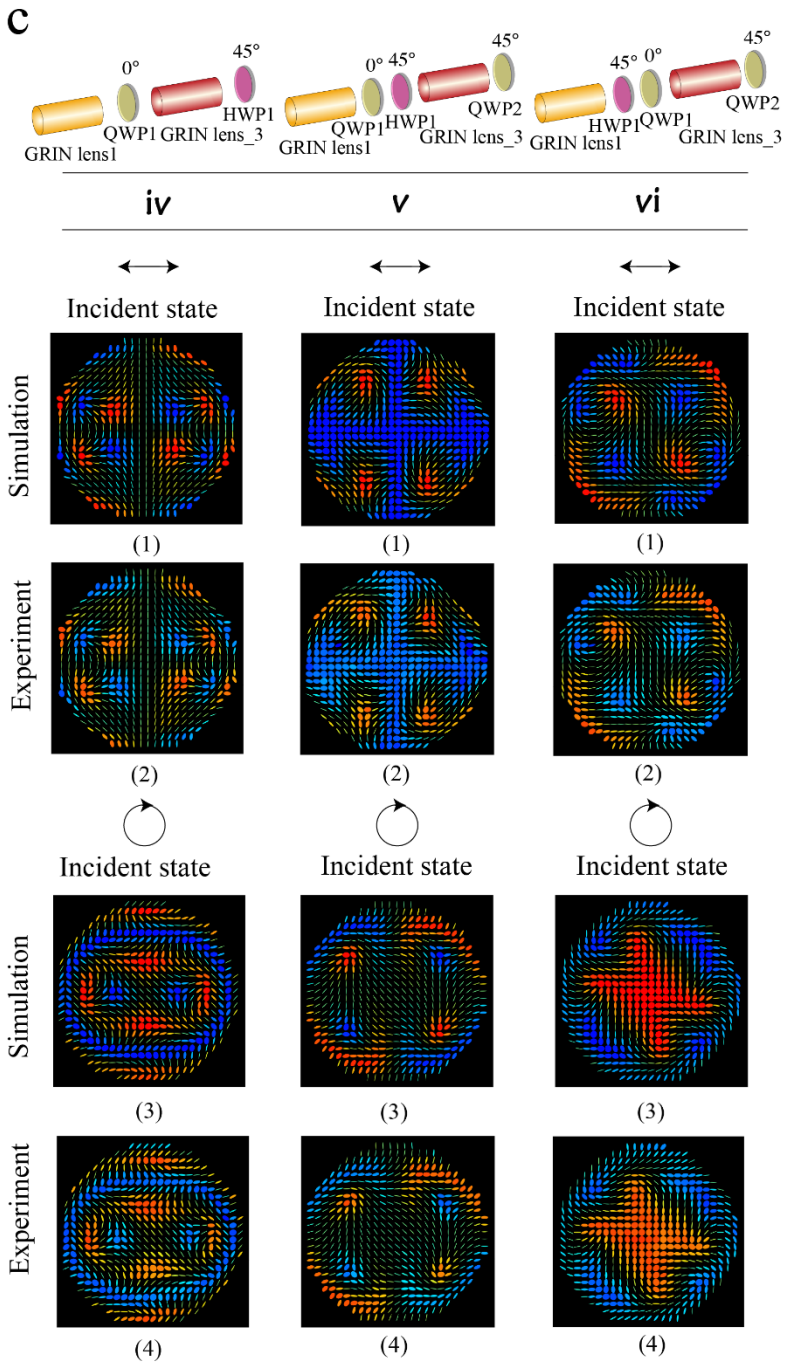


Figure 4.4 VB patterns generated by the dual GRIN cascade employing two different GRIN lenses. (a) the special GRIN lens used in this case is equivalent to an assembly of three of the GRIN lenses used in the experiment for Figure 4.3; (b) and (c) are results from three different cascade structures for each ((i) to (iii) and (iv) to (vi)). The rows for all sub-pictures of (1) and (2) are generated by horizontal linear polarised incident light, and (3) and (4) are generated by right hand circular incident light. (1), (3) are simulation results and (2), (4) are experimental counterparts.

The main principle of VB generation can be found in Eq. (4-1-3), where E_{in} is the incident polarisation light field and E_{out} is the generated beam profile, both represented by Jones vectors. J_{inter}^{m} and J_{GRIN}^{m} $(m = 1,2,3 \ldots)$ are m^{th} Jones matrices of the interstitial optical elements and the GRIN lenses along the cascade. The simulation approach in this section is established through the methods in Chapter 3 with the combination of Eq. (4-1-2) and (4-1-3).

$$E_{\mathrm{out}} = J_{\mathrm{inter}}^{m} \cdot J_{\mathrm{GRIN}}^{m} \cdot J_{\mathrm{inter}}^{m-1} \cdots J_{\mathrm{inter}}^{2} \cdot J_{\mathrm{GRIN}}^{1} \cdot J_{\mathrm{inter}}^{1} \cdot E_{\mathrm{in}}. \quad (m = 1,2,3 \ldots) \qquad (4\text{-}1\text{-}3)$$

Figure 4.5 shows several results using right hand circular polarisation incident light for typical singularities analysis. Based on these results in Figure 4.5, we can make several observations:

1) The GRIN lens cascades are able to generate high radial order VBs due to the nonlinear variation of retardance along the radial direction (Figure 4.5 (b)), and to create high azimuthal order beams (Figure 4.5 (a)). Theoretically, there is no order limit for the generation of the higher order full Poincaré beams. But considering the limitation of our device – in order to have a bigger retardance accumulation, longer GRIN lenses are expected (which might not easily be obtained) – we demonstrated second order vector beams in both radial and azimuthal directions here.
2) These beams in Figure 4.5 contain different kinds of topological structures [131-134], including the so-called lemon and star (associated with topological indices $\pm\frac{1}{2}$, details

refer to Ref [131-134]) as well as spiral (associated with topological index 1 [131-134]), and so on.

3) Figure 4.5 (a) to (c) show GRIN lens cascade generated multiple full Poincaré beams. In Figure 4.5 (a), there are four sectors in the beam profile, each of which contains a full Poincaré beam (the white and green dotted regions show the boundaries of some of these sectors). In Figure 4.5 (b), the red dotted circle contains a full Poincaré beam, the beam inside blue dotted circle contains all polarisation states spanned on the Poincaré sphere twice. In Figure 4.5 (c), we find that in a single-beam there are pair of full Poincaré beams, each with an opposite topological charge (the white and green dotted lines show one pair) and opposite handedness on the corresponding topological charge units.

4) The complex full Poincaré beam in Figure 4.5 (d) contains multiple examples of the same/opposite topological charge units [131-134] and multiple same/opposite handedness beam units (white ellipses demarcate beams that have the same handedness but with opposite topological charges in solid and dotted outlines; those with green outlines have opposite handedness to those in white outlines but with opposite topological charge pairs in their own solid and dotted outlines).

To our knowledge, it has not yet been reported that GRIN lenses can act as a beam generator for various types of VBs and especially for full Poincaré beams. All of the above characteristics

indicate that the various special beams generated by GRIN lens cascades may open new windows for complex polarisation coding and beam engineering. Further quantitative comparisons with existing vector beam generation methods can either a) use the way detailed in section 4.1.1.2 to compare the symmetric properties of the generated beams, or b) use other ways such as measuring the depolarisation properties of the generated vector beams to compare the generation ability of polarisation purity.

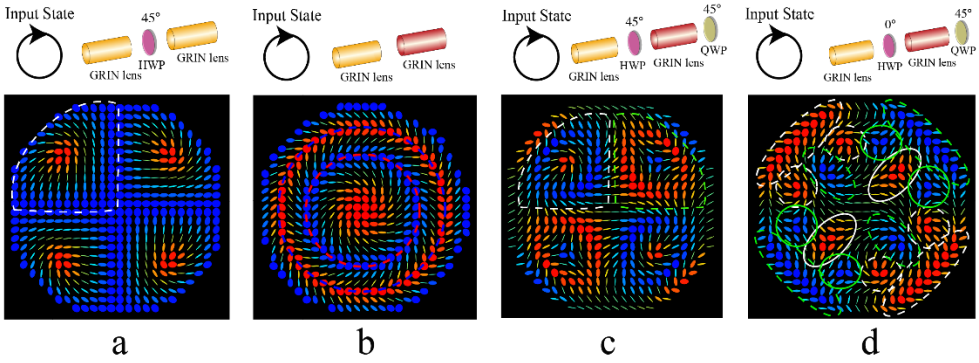


Figure 4.5 Polarisation patterns generated by GRIN cascades employing two identical/different GRIN lenses. (a), (b), (c) and (d) are composed of four different cascade structures which use identical lenses (yellow one) or different lenses (red one). These cascades were also used in Figure 4.2 to 4.4. These beams were generated using right hand circular polarised incident light.

4.1.2 Vortex beam

4.1.2.1 Optical vortex beam – OAM characterization

In this section, based on the polarisation pattern analysis in above section, we provide further details of the analysis of OAM components of different vectorial beams generated by GRIN lens cascade.

4.1.2.2 Phase singularities – single GRIN lens characterization

From Eq. (4-1-1) we know that the Jones Matrix of a GRIN lens is equal to:

$$J_{\mathrm{GRIN}} = \frac{1}{2}\begin{bmatrix} J_{11} & J_{12} \\ J_{21} & J_{22} \end{bmatrix} = \begin{bmatrix} \sin^2(\theta) + \epsilon\cos^2(\theta) & (\epsilon-1)\sin(\theta)\cos(\theta) \\ (\epsilon-1)\sin(\theta)\cos(\theta) & \cos^2(\theta) + \epsilon\sin^2(\theta) \end{bmatrix}, \quad (4\text{-}1\text{-}4)$$

where $\epsilon = \mathrm{e}^{\mathrm{i}\sigma} = \cos(\sigma) + \mathrm{i}\sin(\sigma)$, and $\sigma = f(r) \propto n_{\mathrm{e}}(r)$ (see Chapter 3), θ is the fast axis direction of the equivalent waveplate which equals to the azimuthal angle in the cylindrical coordinate system, r is the radius across the section of the GRIN lens, σ is the linear retardance value of the equivalent waveplate at the position (r, θ). For simplicity of notation, let us make $S^{2\theta} = \sin(2\theta)$, $C^{2\theta} = \cos(2\theta)$, $S^{\sigma} = \sin(\sigma)$, $C^{\sigma} = \cos(\sigma)$. From this we obtain:

$$\begin{bmatrix} J_{11} & J_{12} \\ J_{21} & J_{22} \end{bmatrix} = \begin{bmatrix} 1 + C^{\sigma} + C^{2\theta}(C^{\sigma}-1) + S^{\sigma}\left(1 + C^{2\theta}\right)\mathrm{i} & S^{2\theta}(C^{\sigma}-1) + S^{\sigma}S^{2\theta}\mathrm{i} \\ S^{2\theta}(C^{\sigma}-1) + S^{\sigma}S^{2\theta}\mathrm{i} & 1 + C^{\sigma} + C^{2\theta}(1-C^{\sigma}) + S^{\sigma}\left(1 - C^{2\theta}\right)\mathrm{i} \end{bmatrix}, \quad (4\text{-}1\text{-}5)$$

Suppose a uniformly polarised beam represented by Jones vector E_{in} passes through the GRIN lens J_{GRIN}. We now examine the properties of the generated vector $E_{\mathrm{out}} = J_{\mathrm{GRIN}} \cdot E_{\mathrm{in}}$ in left hand- and right hand-circular eigenpolarisation bases: $E_{\mathrm{L}} = \frac{1}{\sqrt{2}}[1, -\mathrm{i}]^{\mathrm{T}}$, $E_{\mathrm{R}} = \frac{1}{\sqrt{2}}[1, \mathrm{i}]^{\mathrm{T}}$. Following the OAM generation case in the main article, we used a fixed input SOP: $E_{\mathrm{R}} = \frac{1}{\sqrt{2}}[1, \mathrm{i}]^{\mathrm{T}}$ entering a single GRIN lens. Using the Jones matrix calculation of Eq. (4-1-5), we find that,

$$J_{\mathrm{GRIN}}\begin{bmatrix}1\\ \mathrm{i}\end{bmatrix} = z_1\begin{bmatrix}1\\ \mathrm{i}\end{bmatrix} + z_2\begin{bmatrix}1\\ -\mathrm{i}\end{bmatrix}, \tag{4-1-6}$$

where z_1 and z_2 can be written as $z_1 = \frac{1}{2}\left(\mathrm{e}^{\mathrm{i}0} + \mathrm{e}^{\mathrm{i}\sigma}\right), z_2 = \frac{1}{2}\left(\mathrm{e}^{\mathrm{i}(2\theta+\pi)} + \mathrm{e}^{\mathrm{i}(2\theta+\sigma)}\right)$. So, if we use a PSA for state $E_{\mathrm{L}} = \frac{1}{\sqrt{2}}[1, -\mathrm{i}]^{\mathrm{T}}$, would only see the $z_2 E_{\mathrm{L}}$ term from Eq. (4-1-6), which can be written as,

$$z_2\begin{bmatrix}1\\ -\mathrm{i}\end{bmatrix} = \frac{1}{2}\left(\mathrm{e}^{\mathrm{i}(2\theta+\pi)} + \mathrm{e}^{\mathrm{i}(2\theta+\sigma)}\right)\begin{bmatrix}1\\ -\mathrm{i}\end{bmatrix} = A\,\mathrm{e}^{\mathrm{i}(2\theta+\varphi)}\begin{bmatrix}1\\ -\mathrm{i}\end{bmatrix}, \tag{4-1-7}$$

where $A(r)$ is the amplitude distribution. When considering OAM, we are only concerned about the phase term $(2\theta + \varphi)$ in Eq. (4-1-7), where $\varphi(r)$ is an initial phase delay determined by the retardance profile $\sigma(r)$ (see Chapter 3). The exponent i2θ shows that the analyzed E_{L} beam exhibits two units of OAM, which reveals that the GRIN lens can be used as a spin-to-orbital angular momentum convertor. Corresponding results can be found in Figures 4.6 (a) to (h).

We then used a fixed input SOP: $E_{\mathrm{R}} = \frac{1}{\sqrt{2}}[1, \mathrm{i}]^{\mathrm{T}}$ entering a single GRIN lens, but analyzed by $E_{\mathrm{H}} = [1,0]^{\mathrm{T}}$ and $E_{\mathrm{V}} = [0,1]^{\mathrm{T}}$:

$$J_{\mathrm{GRIN}}\begin{bmatrix}1\\ \mathrm{i}\end{bmatrix} = z_{1'}\begin{bmatrix}1\\ 0\end{bmatrix} + z_{2'}\begin{bmatrix}0\\ 1\end{bmatrix}, \tag{4-1-8}$$

From calculation, $[z_{1'} \quad z_{2'}]$ can be written as exponential form:

$$z_{1'} = \frac{1}{2}\left(\mathrm{e}^{\mathrm{i}0} + \mathrm{e}^{\mathrm{i}\sigma} + \mathrm{e}^{\mathrm{i}(2\theta+\pi)} + \mathrm{e}^{\mathrm{i}(\sigma+2\theta)}\right), \tag{4-1-9}$$

$$z_{2'} = \frac{1}{2}\left(\mathrm{e}^{\mathrm{i}\left(\frac{\pi}{2}\right)} + \mathrm{e}^{\mathrm{i}\left(\sigma+\frac{\pi}{2}\right)} + \mathrm{e}^{\mathrm{i}\left(2\theta+\frac{\pi}{2}\right)} + \mathrm{e}^{\mathrm{i}\left(\sigma+2\theta-\frac{\pi}{2}\right)}\right), \tag{4-1-10}$$

In Figure 4.6 below, the corresponding phase profiles, intensity profiles, as well as interference patterns using analysers described by $[1, 0]^{\mathrm{T}}$ (both in experiment and simulation) can be found in Figure 4.6 (d) (iii) to 4.6 (h) (iii) and 4.6 (d) (vii) to 4.6 (h) (vii). We also modified the PSA to obtain a wider variety of wave fronts for illustration; the sequence is shown in Figure 4.6 (b) on the pathway from (i) to (ix) on the Poincaré sphere of the PSA state. The simulated and experimental interferograms as well as intensity distributions can be found in Figure 4.6 (d) to 4.6 (h).

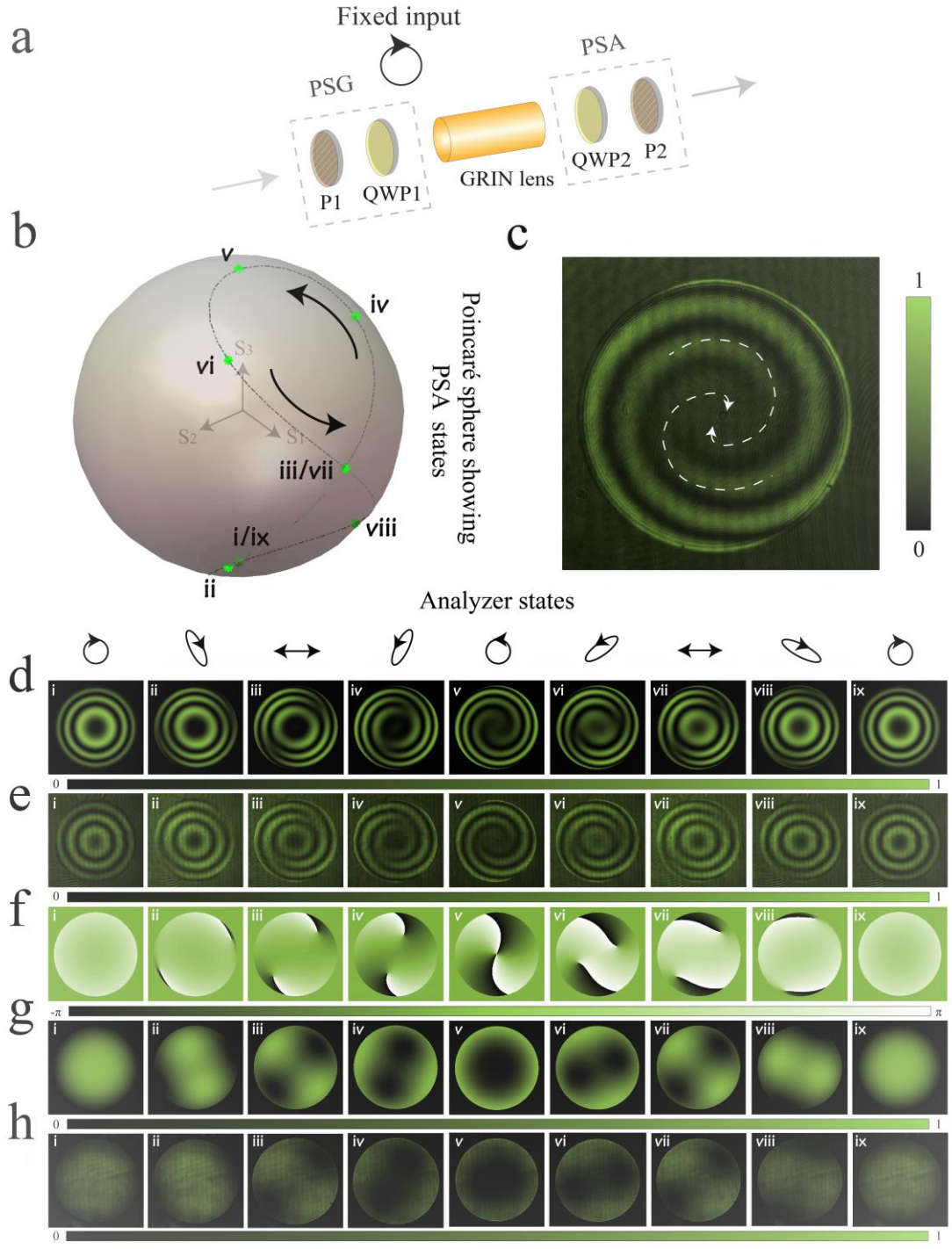


Figure 4.6 OAM generation and characterization (a) Simplified setup for the OAM generation validation. P1 and P2: fixed polarisers with transmission axis at 0°. QWP1: fixed quarter wave plate with fast axis orientation at 45°. QWP2: rotating quarter wave plate. The PSG comprises P1 and QWP1 to generate fix circular SOP, and the PSA is constructed by P2 and QWP2. (b) A Poincaré sphere representation of the pathway of detection polarisation states (i) to (ix) in (d) to (h). (c) A particular illustration of the interference

pattern of state (v) in (f). The two spirals indicated that the light beam contained two units of OAM. (d) to (h) Interference patterns, phase profiles, intensity distributions under different fast axis orientations of the second quarter waveplate (QWP2 in (a)) from -45° to 135° with interval 22.5°. The rows show: (d) Simulation of interference patterns. (e) Experimental interference patterns. (f) Simulation of phase patterns. (g) Simulation of intensity distribution. (h) Experimental intensity distribution. The analyser states for each column are shown above (b). The data here are normalized besides the simulation phase value.

4.1.2.3 Complex phase singularities characterization in GRIN lens cascade

We now examine the properties of the generated vector $E_{\mathrm{out}} = J_{\mathrm{GRIN}} \cdot E_{\mathrm{in}}$ in another specific eigenpolarisation bases ($E_{\mathrm{H}} = [1,0]^{\mathrm{T}}$, $E_{\mathrm{V}} = [0,1]^{\mathrm{T}}$, both in generation and analysis) with single GRIN lens, and then circular eigen bases with multi-GRIN lens based cascades.

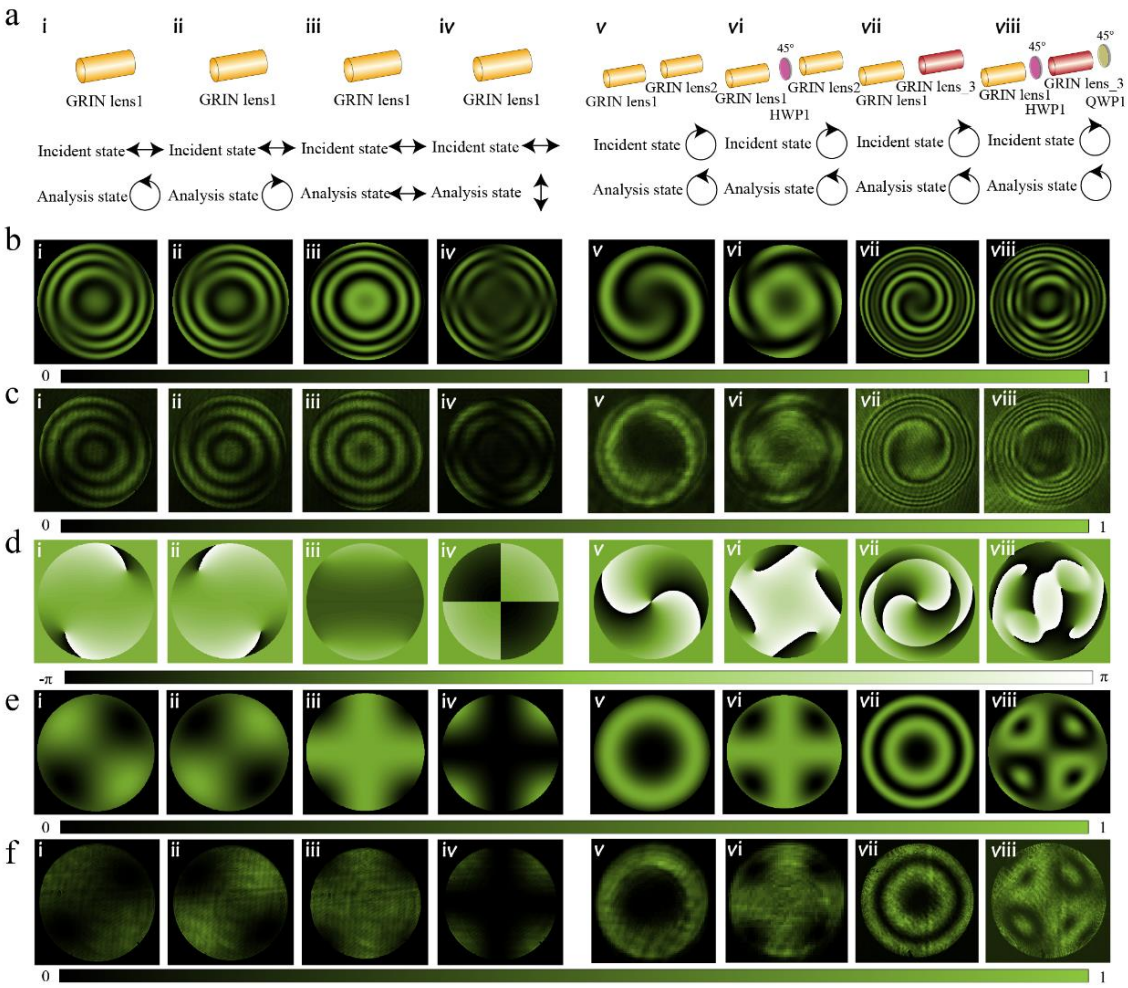


Figure 4.7 Phase profiles, interference patterns, intensity distributions generated by GRIN lens cascade. (a) the corresponding cascade excluding the PSG and PSA, and the specific generated and analysed polarisation state. (b) to (f) simulated interference patterns, experimental interference patterns, simulated absolute phase profiles, simulated intensity distributions and experimental intensity distributions.

We demonstrated cases using linear polarised incident eigenpolarisation bases: $E_{\mathrm{H}} = [1,0]^{\mathrm{T}}$, $E_{\mathrm{V}} = [0,1]^{\mathrm{T}}$. We first used a fixed input SOP: $E_{\mathrm{H}} = [1,0]^{\mathrm{T}}$ entering a single GRIN lens and analyzed by $E_{\mathrm{H}} = [1,0]^{\mathrm{T}}$ and $E_{\mathrm{V}} = [0,1]^{\mathrm{T}}$.

$$J_{\mathrm{GRIN}} \begin{bmatrix} 1 \\ 0 \end{bmatrix} = z_{1}'' \begin{bmatrix} 1 \\ 0 \end{bmatrix} + z_{2}'' \begin{bmatrix} 0 \\ 1 \end{bmatrix}, \tag{4-1-11}$$

We calculate $z_{1''}$and $z_{2''}$ by through the same process used before, as shown in Eq. (4-1-12) and (4-1-13). In the Figure 4.7 we demonstrate phase profiles, intensity distributions and interference patterns (where the object beam is interfered with the same SOP light).

$$z_{1''} = \begin{cases} \frac{1}{2}\left(e^{i0} + e^{i\sigma}\right) + \frac{1}{2}|\cos(2\theta)|\left(e^{i0} + e^{i(\sigma+\pi)}\right), & \theta \in \left[-\frac{3\pi}{4}, -\frac{\pi}{4}\right] \cup \left[\frac{\pi}{4}, \frac{3\pi}{4}\right], \\ \frac{1}{2}\left(e^{i0} + e^{i\sigma}\right) + \frac{1}{2}|\cos(2\theta)|\left(e^{i\pi} + e^{i\sigma}\right), & \text{Otherwise.} \end{cases} \quad (4\text{-}1\text{-}12)$$

$$z_{2''} = \begin{cases} \frac{1}{2}|\sin(2\theta)|\left(e^{i0} + e^{i(\sigma+\pi)}\right), & \theta \in \left[-\frac{\pi}{2}, 0\right] \cup \left[\frac{\pi}{2}, \pi\right], \\ \frac{1}{2}|\sin(2\theta)|\left(e^{i\pi} + e^{i\sigma}\right), & \text{Otherwise.} \end{cases} \quad (4\text{-}1\text{-}13)$$

Using the basis $E_{\mathrm{R}} = \frac{1}{\sqrt{2}}[1, \mathrm{i}]^{\mathrm{T}}$, $E_{\mathrm{L}} = \frac{1}{\sqrt{2}}[1, -\mathrm{i}]^{\mathrm{T}}$ as the analysis eigenbasis, we obtain:

$$J_{GRIN}\begin{bmatrix}1\\0\end{bmatrix} = z_{1'''}\begin{bmatrix}1\\i\end{bmatrix} + z_{2'''}\begin{bmatrix}1\\-i\end{bmatrix}, \quad (4\text{-}1\text{-}14)$$

from which we derive Eq. (4-1-15) and Eq. (4-1-16) below. The corresponding phase profiles, intensity distributions and interference patterns can be found in Figure 4.7 as well.

$$z_{1'''} = \frac{1}{4}\left(e^{i0} + e^{i\sigma} + e^{-i(2\theta+\pi)} + e^{i(\sigma-2\theta)}\right), \quad (4\text{-}1\text{-}15)$$

$$z_{2'''} = \frac{1}{4}\left(e^{i0} + e^{i\sigma} + e^{i(2\theta+\pi)} + e^{i(\sigma+2\theta)}\right). \quad (4\text{-}1\text{-}16)$$

Similar to the polarisation fields shown in the section above, some demonstrations of the complex phase modulation ability of higher order GRIN lens cascades are also shown in Figure 4.7. It can be seen that higher order cascades are able to generate different complex phase patterns that also feature higher order OAM components by choosing the input SOP and the analysis polarisation

state. An example can be seen in Figure 4.7 (d) (vi), which shows four discrete singularities. This method can benefit various applications that require phase control, especially for OAM or vortex beam based applications.

The simulations in this section were based on the theoretical equations above. It should be noted that other combinations of incident polarisations or analysis eigenvectors, or even higher order GRIN lens cascades cases, can be easily calculated through the same process. So, in this section, we have demonstrated here that the GRIN lens cascades have the potential to generate complex structured phase profiles under different input/output eigenpolarisations. This novel structure for phase modulation (including the generation of OAM), derives from the special birefringence profile of GRIN optics. To our knowledge, this has not yet been reported. It might pave the way for new methods of complex beam engineering and benefit corresponding applications such as OAM related quantum-optics and nano-optics studies.

4.1.3 Vector vortex beam

As we have validated in sections 4.1.1 and 4.1.2, the GRIN lenses actually modulate the phase and polarisation simultaneously, so the generated beams are indeed vector vortex beams [31, 34]. It is important to realise that this spatial modulation effects described here are not confined to controlling the beam profile for the corresponding GLSs. They also have applications in focus

shaping such as in fluorescence based GLS micro-endoscope, and application in GLS based polarisation detection which could enable label-free sensing. As we will introduce in later sections and chapters.

4.2 Birefringence and eigenmodes of a GRIN lens

4.2.1 Eigenmodes of a GRIN lens

Due to the inherent link between beam profile and focus, polarisation and/or phase modulation via the cascade also affects the point spread function (PSF) of a GLS. As beam modulations can also be harnessed in many imaging methods to enhance spatial resolution or other imaging properties [42], GRIN lens cascades have expected benefits in various GLSs. Indeed, we can show that through understanding these previously unwanted birefringence phenomena, it is possible to improve the performance of current GLSs, specifically as used for scanning micro-endoscopy.

Previous research has shown that GLS used in biomedical imaging can suffer from a lower-than-expected axial resolution; normally this is attributed to spherical aberration [158, 159]. This has been a particular problem when using multiple pitch or long GRIN lenses, where the PSF has shown significant elongation [30]. We show here that this problematic phenomenon can also be

introduced by the inherent birefringence of the GRIN lens (via the induced spatial polarisation aberration). Furthermore, through understanding of these phenomena, we present a possible solution based upon specific polarisation light fields that improve the axial resolution.

The fast and slow axis distributions of the GRIN lens (see details in Chapter 1) imply that the GRIN lens has two polarisation eigenmodes, for which the beams would maintain the same polarisation profiles throughout the device. These two modes – which are azimuthal and radial linearly polarised light fields – experience their own refractive index profiles $n_o(r)$ and $n_e(r)$, which are still approximately quadratic with r, but have different magnitudes. Hence, their focussing strength is different and the corresponding focussing pitch within the GRIN lens is different. As a consequence, the positions of the two corresponding foci are axially shifted relative to each other in the focal region (for the detailed mechanism see section 1 in Chapter 3). For this reason, other input states that are a combination of these eigenmodes – including uniform polarisation states – create a superposition of both axially offset foci that lead to the elongated focus. However, this problem can be avoided if a single eigenmode is used. The eigenmodes – azimuthal and radial polarized light fields – can be generated via lots of methods, such as using a SHWP (passive component) or multiple SLMs (active components).

4.2.2 Axial resolution modification for GRIN lens imaging system

To verify this proposition experimentally, we first measured the focus of GRIN lens when the input was a mixture of the two eigenmodes, using uniform circular polarisation at the input (Figure 4.8 (a)). The focal spot was elongated along the axis, with full width at half maximum (FWHM) of 17.4 μm (Chapter 3 for the details of GRIN lens and the point spread function measurement process is adopted with reference to Ref [30]). The inclusion of a spatially-variant half waveplate (SHWP) into the cascade, combined with appropriate input polarisation, permitted generation of the two eigenmodes. The pupil fields at the output, as well as the axial PSF, were measured. We can see in Figure 4.8 (b) that the FWHM decreased to 14.1 μm and, in Figure 4.8 (c), that a focal shift of 3.0 μm was presented between the foci of the two eigenmodes, confirming our theory. Note that the foci for the individual eigenmodes were ring shaped in the lateral plane, with zero intensity along the axis due to the phase singularity introduced by the SHWP in the cascade. In a practical imaging system, this effect could be compensated using an appropriate helicoidal phase plate, or an alternative method for preparation of the input polarisation state [160]. Our observations show that enhanced axial resolution can be obtained in a GLS by modulation of the focus through the appropriate configuration of the input polarisation and phase state.

There are several points that should be considered when estimating the uncertainties of the beam split for different GRIN systems. In this validation work, based upon our polarisation measurements above, we estimated that the GRIN lenses we used had maximum birefringence level around 10^{-5} (originating from the intrinsic stress), which is in the range of plausible values for the lithium ion-exchange process used in their manufacture. We tested three different types of pitch 2 GRIN lenses, which, due to their manufacturing processes, had different birefringence properties and lengths. We found that they exhibited variations in beam splitting ranging between ~1.5 μm and ~3.0 μm. These variations are due to the different optical properties of each lens, detailed relationships deserve further explorations. We have assumed here that $n_{\mathrm{o}}(r)$ and $n_{\mathrm{e}}(r)$ follow a parabolic approximation, which one could likely refine for more accurate modelling of the phenomena.

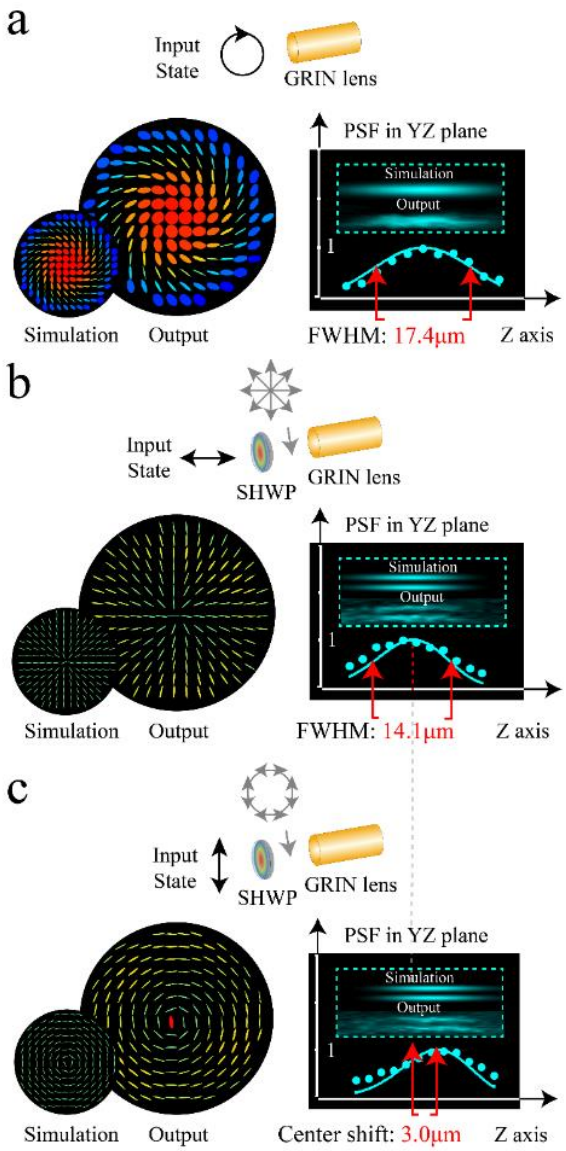


Figure 4.8 PSF modulation through GRIN lens cascade. (a) Schematic of a single GRIN lens cascade illuminated by right hand circular polarised light, beam profile after the GRIN lens, and the corresponding axial PSF including the FWHM. (b) and (c) show the GRIN lens cascade including SHWP with horizontal and vertical linear polarised light input, beam profile after the GRIN lens, and the corresponding axial PSF to demonstrate the focus shift when using the radial/azimuthal polarisation input light fields.

4.3 Summary and discussion

In this chapter, by understanding and harnessing the inherent – and previously undesirable – birefringence of GRIN lenses, we have opened up new possibilities for their use. Combining one

or more GRIN lenses into cascades with other optical elements, provides a wide range of complex beam modulation capabilities to benefit current GLSs, including vector vortex beam generation, focal spot shaping.

The fundamental realizations here about the joint effects of the intrinsic birefringence and the focusing properties of the GRIN lens are also important in understanding some of the current challenges in use of various GLSs [30, 158, 159]. Our observations on the dimensions of the pupil/focal distributions, the use of polarisation eigenmodes, and the improvement of axial resolution, show that better understanding of their vector modulation effects can benefit current GLSs, such as mitigation against aberration problems (we will further explore in Chapter 6) in GRIN lens based two-photon fluorescence micro-endoscopy. Furthermore, the well-controlled creation of ring-shaped foci through vectorial beam manipulation could now enable further lateral resolution enhancements for GLS through stimulated emission depletion [42] (STED), MINFLUX [161] (we will further explore in Chapter 7) or related microscopy methods. These methods are particularly sensitive to polarisation and phase aberrations, so improved understanding of the birefringence effects and their mitigation will be essential if they are to be combined with GLSs. This may find application in *in vivo* deep tissue (such as brain) imaging, which cannot be easily achieved by alternative objective lenses. Combination of the GRIN cascades with active optical elements [162] in cascade, such as a spatial light modulator, could

enable further applications in beam or focal control (we will further explore in Chapter 6 and 7). Further imaging methods for GLSs are then expected across various existing techniques such as structured illumination microscopy [163] (SIM) (we will further explore in Chapter 7). Our observations show that the GRIN cascades perform optically efficient, continuous, non-pixellated, vectorial beam modulation have important consequences for many applications. The geometric phase [144] effects generated within the GRIN cascades are more complex than those from planar wave plate arrays, not only in the spatial domain but also in the time domain (see details in Chapter 3), which may open up interesting prospects for quantum state manipulation. The observation of OAM generation could also have potential for further GRIN lens based micro-manipulation applications, which take advantage of the optical torques introduced by the phase vortex.

Chapter 5

Vectorial beam analysis through GRIN lens cascades

5.1 Müller matrix tissue polarimetry

5.1.1 Introduction of tissue polarimetry

Many common light sources such as the sun, halogen bulbs, LEDs, and incandescent bulbs produce unpolarised light [50, 51]. If the direction of the electric field of light is well defined, it is called polarised light, as we introduced in Chapter 2. The polarisation state of a light beam can be completely represented by a Stokes vector. The Stokes vector of a light beam may change when it interacts with an object due to the polarisation property of the object that can be represented by a Müller matrix (MM) [50, 51]. The MM contains 16 elements to comprehensively represent the polarisation transforming characteristics of the object. Several polarisation parameters, including diattenuation, depolarisation, phase retardance and fast axis direction, etc. can be obtained by a decomposition of the MM, as introduced in Chapter 2. The MM parameters

(derived from MMPD, MMAC methods and so on) are widely employed as quantitative and label-free indicators in many research fields such as remote sensing, material characterisation, and biomedical tissue diagnosis [64, 69, 70, 82, 83].

Polarimetric techniques are up-and-coming tools for recognising complex biological samples, especially those with fibrous or rod-like structures [82, 83]. As a label-free, anisotropic structure sensitive and multi-scattered photons suppressing technique, polarimetry can be used to acquire the information of superficial epithelium [82, 83]. And compared with other label-free methods such as Raman spectroscopy or optical coherence tomography, the polarimetic technique contains several unique advantages: a) it is easy to be combined with other existing techniques to add additional functionality to systems, in the form of polarisation information extraction; b) it can obtain huge amount of the polarisation information of the object (e.g., MM contains the full polarisation properties of the object). Currently, cancer is one of the biggest threats to human health. It is reported that more than 85% of all cancers start with cells developed in the superficial epithelium of the tissue [139], which means that polarimetric techniques have great potential in early cancer detection [139]. In previous research, polarimetric techniques have been applied to assist the diagnosis of various cancerous tissues such as liver cancer, thyroid cancer, cervical cancer and skin cancer [68, 74]. Among available polarimetric techniques, MM polarimetry is

advantageous because it is capable of extracting comprehensive polarisation properties of the sample [91-97]. It is a prevalent imaging and detection method in biomedical applications, where its ability to characterize tissue structures in a label-free manner is highly advantageous [91-97]. Numerous MM polarimeters for tissue imaging have been proposed, many of which are based on sequential generation of states of polarisation (SOP) and analysis by rotation of polarisation components or modulation of variable retarders, in the polarisation state generator (PSG) and analyser (PSA) [91-97].

5.1.2 Sequential/simultaneous Müller matrix tissue polarimetry

Quite a lot of MM polarimeters used in tissue imaging use time-sequential measurement and employ polarisation components such as rotatable waveplates/polarisers, SLMs and photoelastic modulators [68, 74]. However, sequential measurement is not suitable for fast detection, such as for moving objects where it can lead to unexpected measurement errors [73]. The speed can also limit the application of MM polarimetry on *in vivo* detection of dynamic samples in clinical applications [73]. Previous researches have also highlighted some single-shot MM polarimetries for dynamic biomedical samples characterization [164, 165]. However, the requirement of the optical components is normally high and the equipment is not easy to be minimized into a small, cost-effective, embeddable device to access further border usage of tissue polarimetry in applications such as minimal invasive surgery (MIS) [73, 81].

5.2 Snap-shot GRIN lens Müller matrix polarimeter

As shown in Chapters 3 and 4, there is a complex interdependence of the focal field and the polarisation state of the input beam, as processed through the GRIN lens cascade. This dependence provides further opportunities to harness the birefringence properties of the GRIN lens as parallel analysis channels for polarisation sensing. The primary ability of the GRIN lens as a focussing device is due to its continuously varying, rotationally symmetric refractive index distribution. As we already discussed, this is accompanied by the gradually varying birefringence distribution. As a high degree of symmetry is required for focusing, this means that the birefringence distribution is also highly symmetric. It provides a continuous, non-pixellated range of analysis channels that could be used for polarimetry. In this Chapter, by harnessing the commonly undesirable birefringence, we put forward a new single-shot MM polarimeter based on GRIN lens cascade, as shown in Figure 5.1 (see next section for more information about the design of both PSG and PSA).

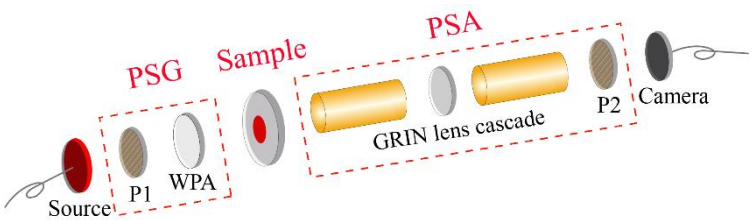


Figure 5.1 GRIN lens based MM polarimeter. Simplified setup of the polarimeter. PSG: P1, polariser; WPA, waveplate array, with different fast axis orientations in each quadrant. PSA: P2, polariser; GRIN lens cascade.

5.2.1 Measurement principle

We first derive here the main equations describing the principle of operation of the MM polarimeter. We use *n* (*n*=1, 2, 3 and 4) to denote the four areas of the PSG array corresponding to the four sectors of the FQWP, and *m* (*m*=1, 2, 3 ... *M*) to denote the chosen pixel number in each sector.

$$S_{\mathrm{out}}^{n,m} = M_{\mathrm{P2}} \cdot M_{\mathrm{GRIN2}}^{n,m} \cdot M_{\mathrm{HWP}} \cdot M_{\mathrm{GRIN1}}^{n,m} \cdot M_{\mathrm{Sample}} \cdot S_{\mathrm{in}}^{n,m}, \qquad (5\text{-}2\text{-}1)$$

where $S_{\mathrm{in}}^{n,m}$ represents incident Stokes vectors generated by the four sectors of the PSG array (the *m* is the chosen pixel number in each sector; all pixels in each sector have same incident SOP). $S_{\mathrm{out}}^{n,m}$ is the combination of output Stokes vectors (both in the channel *m* of the sector *n*; the same meanings are followed in the later description). M_{Sample} denotes the MM of the targeted sample, and M_{P2}, M_{HWP} denote the MMs of the polariser and the half waveplate. $M_{\mathrm{GRIN1}}^{n,m}$, $M_{\mathrm{GRIN2}}^{n,m}$ are MMs of the GRIN lenses in the corresponding spatial positions. Since only intensity information can be recorded by the camera, which means only the first element of $S_{\mathrm{out}}^{n,m}$ can be obtained (the intensity information at sector *n* from channel *m*), then Eq. (5-2-1) can be modified into Eq. (5-2-2) and Eq. (5-2-3):

$$I_{\mathrm{out}} = A \cdot M_{\mathrm{Sample}} \cdot S_{\mathrm{in}}, \qquad (5\text{-}2\text{-}2)$$

$$\begin{bmatrix} I_{\text{out}}^{1,1} \\ \vdots \\ I_{\text{out}}^{1,M} \\ I_{\text{out}}^{2,1} \\ \vdots \\ I_{\text{out}}^{2,M} \\ I_{\text{out}}^{3,1} \\ \vdots \\ I_{\text{out}}^{3,M} \\ I_{\text{out}}^{4,1} \\ \vdots \\ I_{\text{out}}^{4,M} \end{bmatrix} = \begin{bmatrix} a_0^{1,1} & a_1^{1,1} & a_2^{1,1} & a_3^{1,1} \\ \vdots & & & \\ a_0^{1,M} & a_1^{1,M} & a_2^{1,M} & a_3^{1,M} \\ a_0^{2,1} & a_1^{2,1} & a_2^{2,1} & a_3^{2,1} \\ \vdots & & & \\ a_0^{2,M} & a_1^{2,M} & a_2^{2,M} & a_3^{2,M} \\ a_0^{3,1} & a_1^{3,1} & a_2^{3,1} & a_3^{3,1} \\ \vdots & & & \\ a_0^{3,M} & a_1^{3,M} & a_2^{3,M} & a_3^{3,M} \\ a_0^{4,1} & a_1^{4,1} & a_2^{4,1} & a_3^{4,1} \\ \vdots & & & \\ a_0^{4,M} & a_1^{4,M} & a_2^{4,M} & a_3^{4,M} \end{bmatrix} \cdot M_{\text{Sample}} \cdot \begin{bmatrix} s_0^{1,1} & \cdots & s_0^{1,M} & s_0^{2,1} & \cdots & s_0^{2,M} & s_0^{3,1} & \cdots & s_0^{3,M} & s_0^{4,1} & \cdots & s_0^{4,M} \\ \vdots & \ddots & \vdots & \vdots & \ddots & \vdots & \vdots & \ddots & \vdots & \vdots & \ddots & \vdots \\ s_3^{1,1} & \cdots & s_3^{1,M} & s_3^{2,1} & \cdots & s_3^{2,M} & s_3^{3,1} & \cdots & s_3^{3,M} & s_3^{4,1} & \cdots & s_3^{4,M} \end{bmatrix}. \tag{5-2-3}$$

Where the intensity information recorded by the camera for each modulation and detection channel are defined as a vector:

$$I_{\text{out}} = \begin{bmatrix} I_{\text{out}}^{1,1} & \cdots & I_{\text{out}}^{1,M} & I_{\text{out}}^{2,1} & \cdots & I_{\text{out}}^{2,M} & I_{\text{out}}^{3,1} & \cdots & I_{\text{out}}^{3,M} & I_{\text{out}}^{4,1} & \cdots & I_{\text{out}}^{4,M} \end{bmatrix}^{\text{T}}, \tag{5-2-4}$$

and A is defined by:

$$A = \begin{bmatrix} A^{1,1} & \cdots & A^{1,M} & A^{2,1} & \cdots & A^{2,M} & A^{3,1} & \cdots & A^{3,M} & A^{4,1} & \cdots & A^{4,M} \end{bmatrix}^{T}, \tag{5-2-5}$$

which is a $4m \times 4$ matrix in which each component $A^{n,m} = \begin{bmatrix} a_0^{n,m} & a_1^{n,m} & a_2^{n,m} & a_3^{n,m} \end{bmatrix}$ consists of the first row of the corresponding $M_{\text{P2}} \cdot M_{\text{GRIN2}}^{n,m} \cdot M_{\text{HWP}} \cdot M_{\text{GRIN1}}^{n,m}$. We then expand $S_{\text{in}}^{n,m} = \begin{bmatrix} s_0^{n,m} & s_1^{n,m} & s_2^{n,m} & s_3^{n,m} \end{bmatrix}^{\text{T}}$, and let

$$S_{\text{in}} = \begin{bmatrix} s_0^{1,1} & \cdots & s_0^{1,M} & s_0^{2,1} & \cdots & s_0^{2,M} & s_0^{3,1} & \cdots & s_0^{3,M} & s_0^{4,1} & \cdots & s_0^{4,M} \\ \vdots & \ddots & \vdots & \vdots & \ddots & \vdots & \vdots & \ddots & \vdots & \vdots & \ddots & \vdots \\ s_3^{1,1} & \cdots & s_3^{1,M} & s_3^{2,1} & \cdots & s_3^{2,M} & s_3^{3,1} & \cdots & s_3^{3,M} & s_3^{4,1} & \cdots & s_3^{4,M} \end{bmatrix}, \tag{5-2-6}$$

which is a $4 \times 4m$ matrix that consists of columns that are individual Stokes vectors from each combination of PSG sectors and camera pixels. Then the MM of the sample can be calculated as:

$$M_{\text{Sample}} = A^{-1} \cdot I_{\text{out}} \cdot S_{\text{in}}^{-1}, \tag{5-2-7}$$

where S_{in}^{-1} is the pseudo inverse matrix of S_{in} , and A^{-1} is the pseudo inverse matrix of A.

5.2.2 System design

In this section, we give two geometries for a GRIN lens-based snap-shot MM polarimeter – one configuration using a single GRIN lens and another configuration based on dual GRIN lenses. The detailed design, optimization of both the PSG and PSA are presented. We also compare the advantages and disadvantages of two such configurations to choose the better one to carry on further experimental validations.

5.2.2.1 Single GRIN lens configuration

Here, we propose a new MM polarimeter to measure the point MM in a single-shot, taking advantage of the polarisation properties of a GRIN lens – its gradually changing birefringence profile. A GRIN lens contains spatially varied birefringence and was previously used as a variable retarder in spatial domain to construct a single-shot GRIN lens Stokes polarimeter [166]. Optimized polarisation analysing channels have been calculated theoretically and validated experimentally [166, 167]. It should be pointed out that due to topological charge of GRIN lens

is two (validated in Chapter 3 and 4) – i.e., the fast axis distribution spans across the effective orientations (0 degree to 90 degrees) twice – so actually half of the GRIN lens could contain optimized Stokes vector measurement channels. Based on that conclusion, we put forward one possible configuration of a single-shot MM polarimeter based on single GRIN lens.

The polarimeter architecture (shown in Figure 5.2 (a)) contains: A PSG array comprising four quarter waveplates with different orientations, is designed and used to simultaneously generate four optimized SOPs, illuminating different areas of a sample. The GRIN lens is explored to simultaneously determine four emergent Stokes vectors from the corresponding areas of the sample, with a polariser as the PSA, then the MM of the sample can be derived by taking a snapshot using a CCD camera (mathematical equations can be found in above section). Such a MM polarimeter does not involve moving parts, electrical signal modulation, or the division of amplitude components. There are many ways to specify the illumination polarisations and analyser configurations for MM polarimetry [73, 167]. To find optimum measurement configurations, one can use the condition number (CN) (which is widely used for the optimization of instrument matrices (PSG/PSA) of various polarimeters [73, 167]) of the system as an optimisation criterion for both the PSG and PSA [73, 167]. The CN can also be related to the volume of the inner tetrahedron constructed by the SOPs inside the Poincaré sphere (shown in Figure 5.2 (c) below) [73, 167].

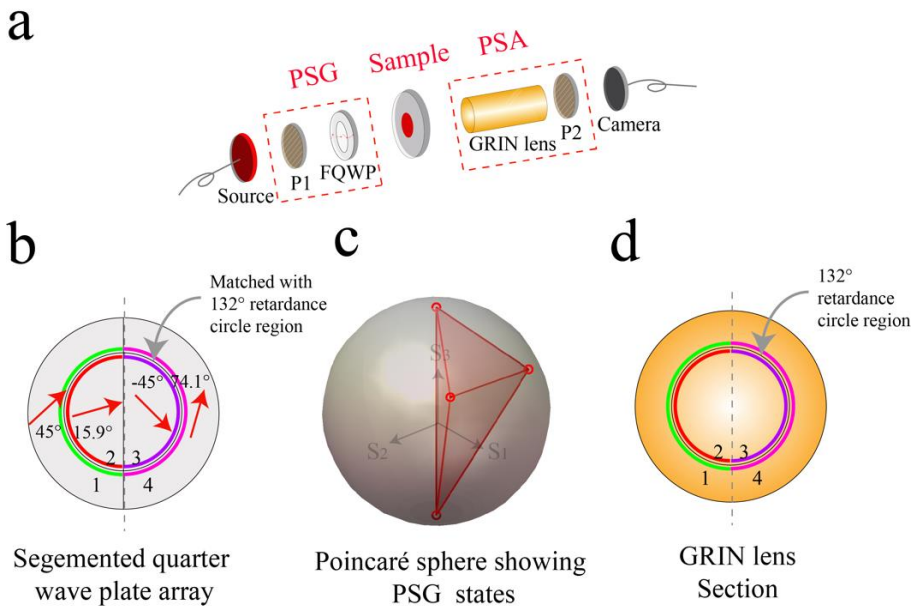


Figure 5.2 Characterisation of single GRIN lens based MM polarimeter. (a) Simplified setup of the polarimeter. PSG: P1, polariser; FQWP, four-quadrant quarter waveplate, with different fast axis orientations in each quadrant. PSA: P2, polariser. (b) Schematic of the waveplate array of PSG (and its related Poincaré sphere in (c) showing the SOPs generated by the PSG) and (d) the corresponding front surface section of GRIN lens. Area 1, 2, 3 and 4 in (b) and (d) are well matched. The red arrows in (b) represent the fast axis direction of the four quarter waveplates (45°, 15.9°, -45° and 74.1°) and the colourful four half annuluses (green, red, purple and pink) are regions for analysis. The solid grey circle in (d) is the 132° retardance circle region of the GRIN lens, and the solid grey line is central line.

In the previous Stokes polarimeter study, different ring regions from the GRIN lens surface have been chosen to calculate the Stokes vectors according to CN [73, 167]. It was found that the 132° phase retardance ring of the GRIN lens section has the lowest CN with the best measurement accuracy, which was also validated in other Stokes polarimeter works [73, 167]. As shown in Chapter 3, the polarisation characteristics of GRIN lens are centrally symmetric, and as we discussed above that a half annulus can have the same CN as the whole ring has according to the

definition of CN. Thus, four half annuluses located in the neighbourhood of the 132° phase retardance circle of the GRIN lens are chosen as separate analysis channels in Figure 5.2 (d). It also makes the GRIN lens into a key part of a multiple Stokes vectors analyser. Regions for calculation can also be found in Figure 5.2 (d) highlighted by four different colours (green, red, purple and pink).

According to these chosen regions, the key part of the PSG – a special segmented waveplate array (see Figure 5.2 (b)) – is designed with two half annulus shaped waveplates (area 1, 4) and two semi-circle shaped waveplates (area 2, 3), shown in Figure 5.2 (b). The red arrows represent the fast axis directions of the waveplates (45°, 15.9°, -45° and 74.1° in area 1, 2, 3 and 4 separately) which were optimized according to Ref [73, 167] for the PSG of a traditional MM polarimeter with a criterion of CN.

In this section we indeed put forward a new single-shot MM polarimeter; However, if we think further, this type of polarimeter with four uneven surface segmented PSG and PSA is not suitable for back scattering detection configuration [81], such as *in vivo* clinical diagnosis. So, in the next section, we will put forward a dual GRIN lens based single-shot MM polarimeter, which is more suitable for back scattering configuration.

5.2.2.2 Dual GRIN lenses configuration

For a back scattering configuration polarimetry, the best way is to modify the PSA, by segmenting the GRIN lens surface into four quadrants, and all of them could reach optimal CN to keep measurement precision. Based upon this, we propose here a new compact single-shot MM polarimeter based on a GLS – specifically, a dual GRIN lens cascade. It includes a PSG consisting of a polariser and a four-quadrant quarter waveplate (Figure 5.3 (b) (i)) to generate simultaneously four different illumination SOPs. Figure 5.3 (b) (ii) shows the optimized SOPs on the Poincaré sphere as generated by the PSG (the fast axes of waveplates 1 to 4 were oriented at 45°, 15.9°, 74.1°, and -45° according to the optimization shown in Ref [73, 167], same as the single GRIN lens configuration). The GRIN lens cascade based PSA is shown in Figure 5.3 (a); here, a half-waveplate was sandwiched between two identical GRIN lenses, which were followed by a polariser. We applied the MMPD method (see method in Chapter 2) to assess the equivalent retardance and fast axis direction of the GRIN cascade in PSA – these are shown for both simulation and experiment in Figure 5.3 (c) (ii) and (iii). Each of the four quadrants of the PSA provides access to a continuum of polarisation analysis channels. Taking advantage of these channels, the GRIN lens cascade can be employed as a complete analyser to calculate four Stokes vectors in a single-shot – one for each of the four channels, which thus enables the single-shot MM measurement. As shown in Figure 5.3 (c) (ii) and 5.3 (c) (iii), the polarisation properties of

the GRIN lens cascade have rotational symmetry (this cascade is also used to generate four equivalent full Poincaré beams units in a single beam in Chapter 4). And, each of the four sectors equivalently encompasses required optimal combinations of retardance and fast axis direction, and each sector is enabled to generate a full Poincaré beam. Additionally, as the birefringence profile is determined by the atomic level scale of ion implantation, the number of potential channels in the system is determined in effect by the pixelation of the camera. Thus, the GRIN lens based MM polarimeter has the great advantage of providing multiple parallel channels to aid the calculation. We chose m (m=4, 5, 6…) pixels in each channel to calculate four Stokes vectors simultaneously, to then work out the target MM. If taking MMPD results as a standard, the chosen pixels encompass the analysis channels of the 132° phase retardance ring on each PSA sector, so it follows that the optimum CN (1.732) can be achieved. The additional effective pixels can help reduce spatial noise when combining the pixel information [73, 166, 167]. For these reasons, the GRIN cascade can form as a basis of an optimal MM measurement system.

Specially, compared with the single GRIN lens design, this design is actually a more versatile instrument and can be adapted for either transmission or back scattering configuration according to various applications and it has potential to act as a polarisation detected fibre-based probe, making use of the polarisation characteristics and volume of the GRIN lens. So, in the validation process, we focused on the dual GRIN lens based MM polarimeter.

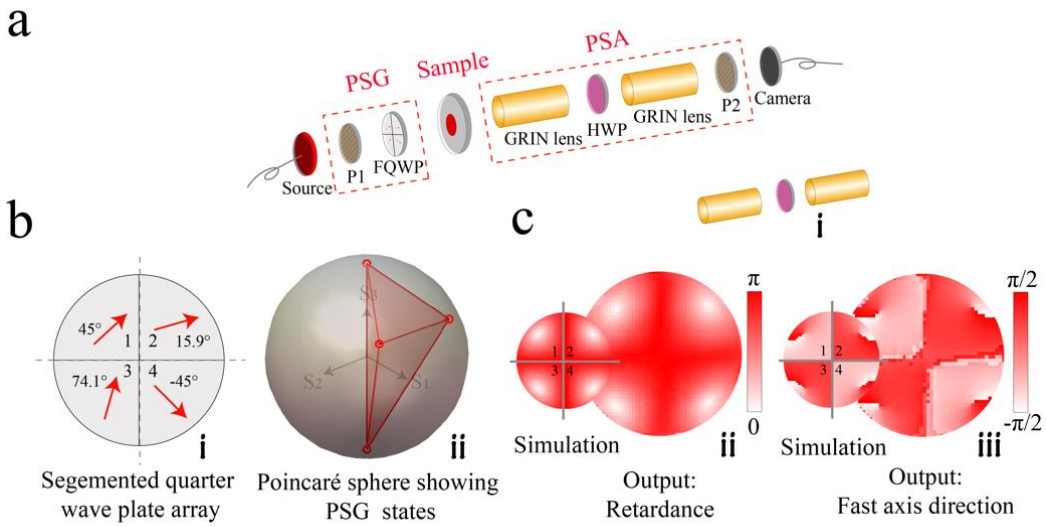


Figure 5.3 Characterization of dual GRIN lens based MM polarimeter. (a) Simplified setup of the polarimeter. PSG: P1, polariser; FQWP, four-quadrant quarter waveplate, with different fast axis orientations in each quadrant. PSA: P2, polariser; HWP, half waveplate. (b) (i) and (ii) details of FQWP and the Poincaré sphere showing the SOPs generated by the PSG. (c) (i) The GRIN lens cascade in the PSA besides the P2. (ii) and (iii) Simulation and experimental results of retardance and the fast axis orientation of (i), derived by the MMPD method. The retardance range is from 0 to π radians and the fast axis orientation range is from -π/2 to π/2 radians.

5.2.3 Validation of standard samples

In order to test the capabilities of the dual GRIN lens based MM polarimeter, we used as samples four polarisers with different orientations (0°, 90°, 45°, -45°), which are illustrated as P2 to P5 in the experimental setup in Figure 5.4 (a). We took measurements of each polariser in a single-shot and compared the derived MMs with the theoretical MMs (Figure 5.4 (b) (i) to 5.4 (b) (iv)). The maximum errors of the derived MM elements were smaller than 6.93%. The GRIN lens cascade based polarimeter has the following advantages: 1) it can perform single-shot MM measurement in a robust and stable manner; 2) single-shot measurements enable precise measurement of

moving/dynamic objects; 3) it has the potential to be miniaturised into an integrated instrument, especially a fibre-based probe with scanning detection for clinical applications.

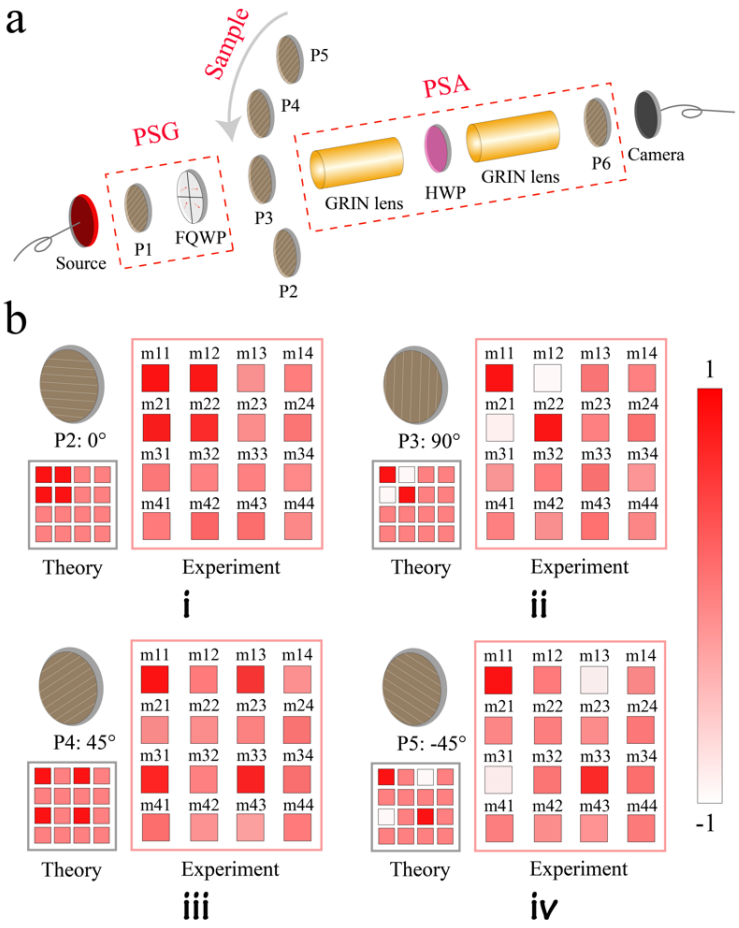


Figure 5.4 Characterization of dual GRIN lens based MM polarimeter. (a) Simplified setup for the validation experiment of the polarimeter. PSG: P1, polariser; FQWP, four-quadrant quarter waveplate, with different fast axis orientations in each quadrant. PSA: P6, polariser; HWP, half waveplate. P2 to P5: polarisers with transmission axis orientations at 0°, 90°, 45°, -45°. (b) (i) to (iv) The measured single-shot MMs (MM element value range is normalized into -1 to 1) of the four polarisers (red boxes), and corresponding ground truth (black boxes).

5.3 Cancer characterization via GRIN lens cascade

Previous studies showed that the changes of fibrous tissue structures, which are strongly related to the MMPD parameter retardance δ, are important features to determine the progression stages of human breast ductal carcinoma [139]. Thus, in this section, in order to show potential biomedical application of the dual GRIN lens based MM polarimeters, we measured the MMs of the human breast ductal carcinoma tissue slides at two different stages. Clinically, different stages of breast ductal carcinoma tissues have different proportions and distribution of fibrous structures in and around the milk ducts (there are stages 1 (normal), 2 (ductal carcinoma in situ) and 3 (invasive ductal carcinoma)) [139]. Through this work, the samples were unstained, dewaxed sections of human breast ductal carcinoma tissue slices at different stages, prepared and provided by the Department of Pathology, Shenzhen Sixth People's (Nanshan) Hospital. For the tissues in stages 1 (normal), and 3 (invasive ductal carcinoma), we selected 12-μm-thick slices [139] for demonstration. For comparison, the corresponding 4-μm-thick hematoxylin and eosin (H and E) stained slices [139] were also prepared. The age range of the patients was from thirty to fifty-five years. This work was approved by the Ethics Committee of the Shenzhen Sixth People's (Nanshan) Hospital.

The obtained results were also compared to those acquired using a traditional MM microscope (as a ground truth). We found that the new MM polarimeter can distinguish the healthy human breast tissues from cancerous ones efficiently in a snapshot, without requiring any use of

exogenous contrast agents. But we also noticed that the results obtained with the new polarimeter demonstrated a larger standard deviation than the MM microscope.

5.3.1 GRIN lens cascade polarimeter measurement

We measured 10 points per sample using our new MM polarimeter and a conventional MM microscope (overall 20 samples), as ground truth for quantitative comparison. In each sample, we chose the points by using MM polarimeter with the diameter of the field of view (FOV) at 0.19 mm (Femto Technology Co. Ltd., G-B151157-S1483). The FOV of the MM microscope (error of elements < 0.3%) was around four times larger than that of the polarimeter, so we took measurements from chosen sub-areas within same FOV of MM polarimeter to be processed. Then we calculated the mean value of the retardance across these areas to set as ground truth for further comparison through the same quantitative comparison process used to differentiate the breast cancerous stages by polarisation parameters [139].

We first demonstrated the method on one healthy tissue sample (named Sample H1, where H represents healthy) and one carcinoma tissue sample (named Sample C1, where C represents cancerous). The number of the random sampled points measured by the GRIN lens cascade for each was fixed at 10 throughout this work (see Figure 5.5, corresponding method refers to Ref [139]).

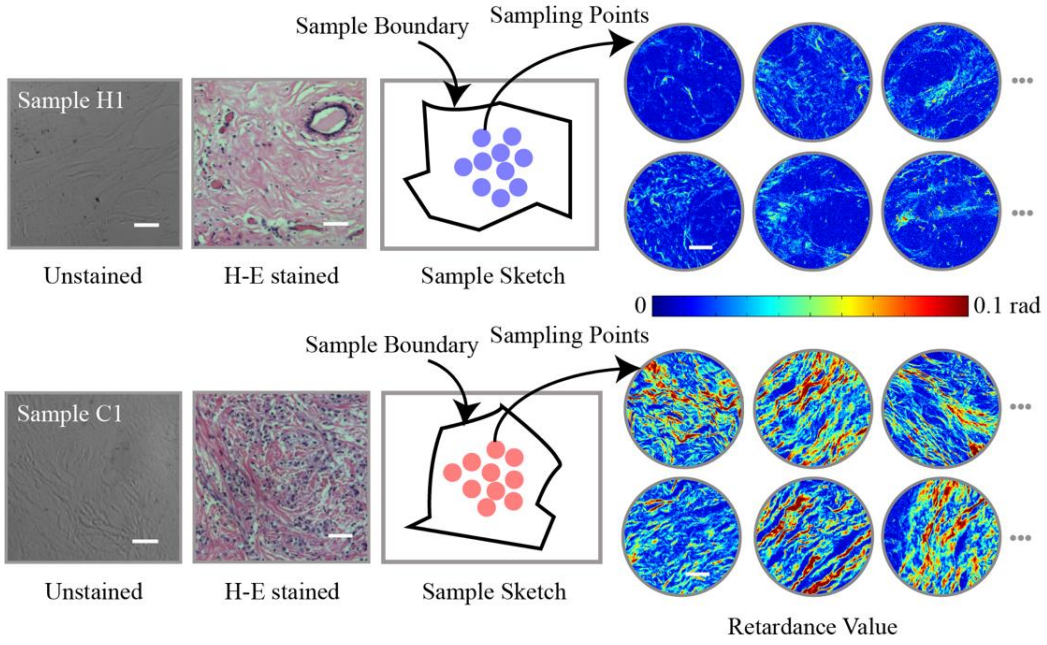


Figure 5.5 Demonstration of the samples H1 and C1 (unstained slides and their H-E stained counterparts). Sketches with corresponding random sampling points and examples of retardance distributions measured by the MM microscope (as ground truth). Scale bar: 50 μm.

Example MMs, as well as corresponding MMPD parameters images, from healthy and cancerous tissues are illustrated in Figure 5.6 below.

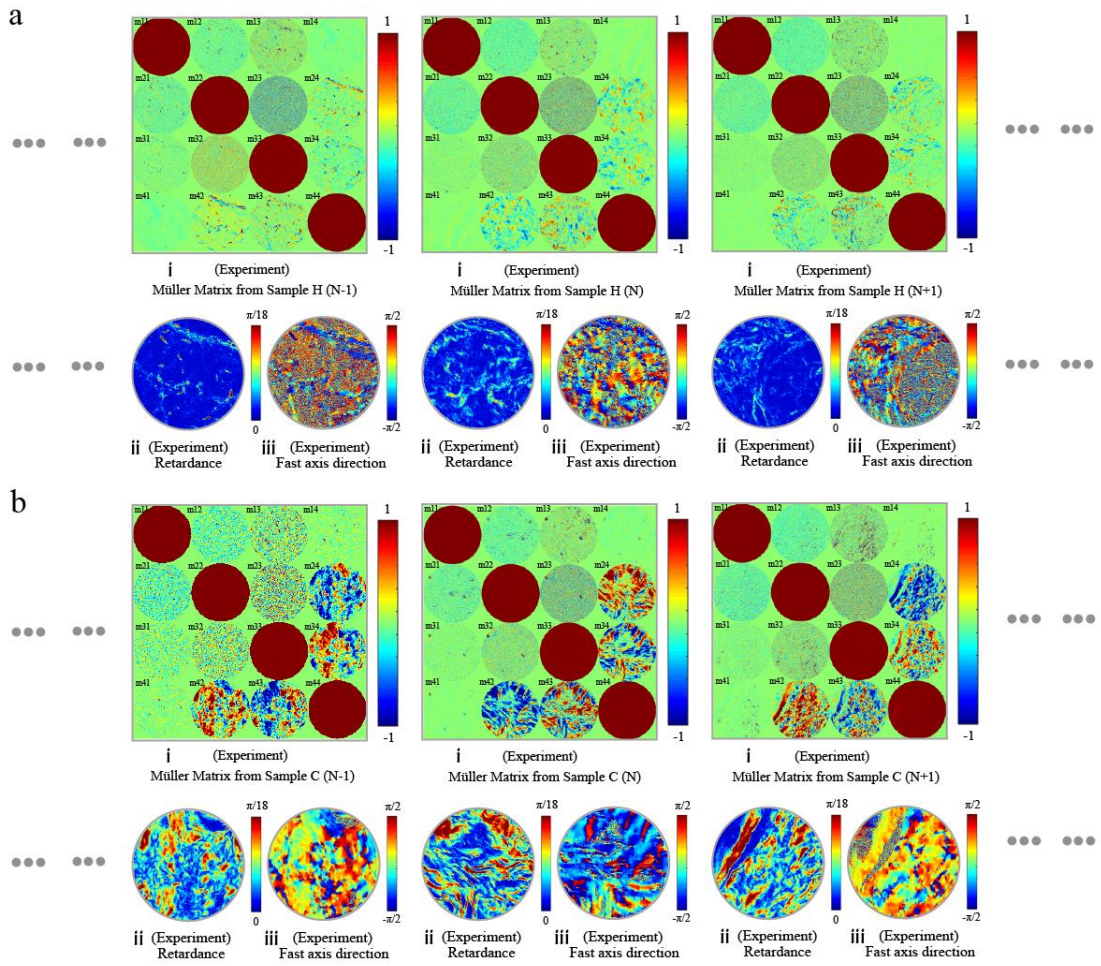


Figure 5.6 Original MMs of healthy and cancerous samples. (a) Demonstrations of the original MMs (MM element value range is normalized into -1 to 1) (i), MMPD parameters (retardance (ii) and fast axis directions (iii)) of the healthy samples. (b) Demonstrations of the original MMs, MMPD parameters (retardance (ii) and fast axis directions (iii)) of the cancerous samples.

5.3.2 Data processing algorithm and optimization method

For simplicity of measurement by the MM polarimeter we assume that measurement of the average SOP should be sufficient for discrimination purposes. We first defocused the GRIN lens image, in order to implement optical averaging of the polarisation effects of spatially varying structures, then applied the processes in flow chart (Figure 5.7) to calculate the retardance value.

In this work, the original retardance value α_1 of the chosen region on PSA has been set as 132° (optimal CN region [73, 166, 167]), β is a threshold parameter set as 0.5, γ_1, ε are predetermined parameters corresponding to the step size (determined retardance value changing rate for the chosen region) and maximum region (determined effective CN region [73, 166, 167]). These were set at the default value 1° and 30°, respectively. Note that 1) for feasibility demonstration we simply begin to choose region with optimal CN (related with 132° retardance) to calculate MM. 2) If the reconstruction failed, we chose other rings (adjacent rings within effective CN region on PSA) to continue the same process (see Figure 5.7). 3) As for region chosen, there are two directions (add or minus retardance on each sector) that both could have effective CN, so the right hand side processes in Figure 5.7 keep it works for both. 4) Of course other kind of region shape can be chosen and optimize those processes.

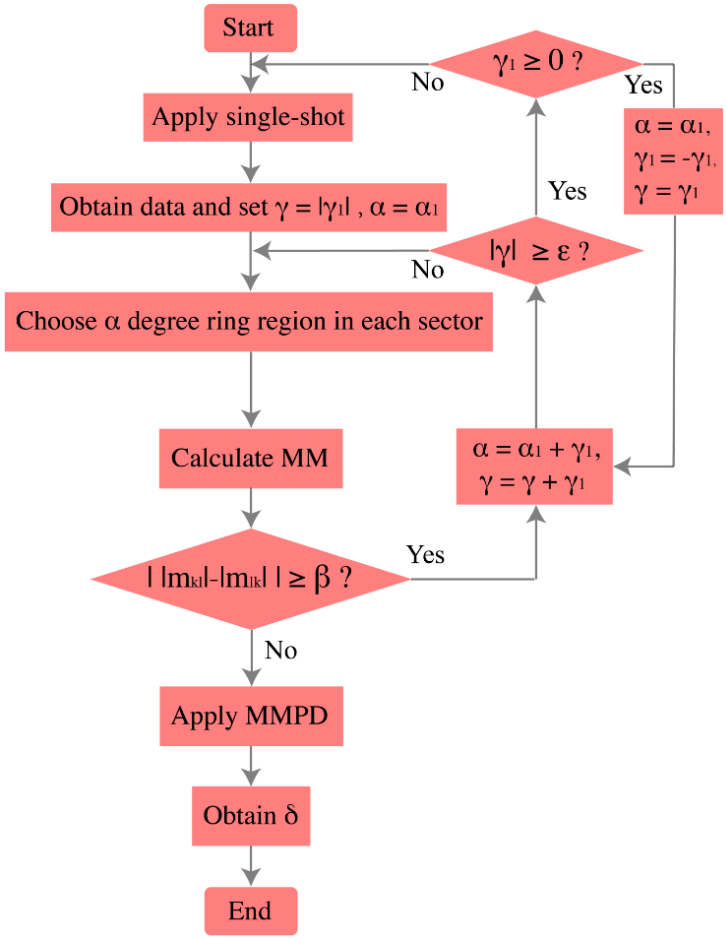


Figure 5.7 Flow chart for retardance calculation. m_{kl} (k, l = 1,2,3,4) and m_{lk} (k, l = 1,2,3,4) are symmetric elements of MM. α_1, γ_1, ε are predetermined retardance value parameters. β is a predetermined threshold parameter. δ is the retardance value. α and γ are variable parameters.

5.3.1 Statistical analysis, comparison and error analysis

Figure 5.8 (a) reveals the statistical distribution of data measured by the cascade and MM microscope, as ground truth (see data details and the corresponding P-value analysis in Table 5.1 below). We found from the data that the measured values of retardance for Sample C1 were significantly larger than those of the Sample H1 just as the same significant difference existed among the data measured by MM microscope. Then we applied the same processes to other

samples. Demonstrations of statistical histograms (mean value and the standard deviation of the retardance) of different samples measured by the GRIN lens cascade and a conventional MM microscope (ground truth) were shown in Figure 5.8 (b).

Furthermore, all the obtained data measured by the MM polarimeter were used to draw an overall 3-D dot distribution in Figure 5.8 (c). The measured values from all 10 breast ductal carcinoma samples (1324 ± 433 rad/104) were significantly larger than those of the 10 healthy ones (408 ± 189 rad/104) – these retardance measurements were calculated from the original measured data (in Figure 5.8 (c)) through standard statistical methods [139] to obtain their mean values and standard deviations. The difference is due to the larger proportion of fibrous structures present in the cancerous tissues, which is a consequence of the inflammatory reactions induced by cancer cells [139]. The results reveal that the GRIN lens cascade based polarimeter has the ability to differentiate between healthy and cancerous breast tissues. Then, combined with the corresponding MM microscope data, Table 5.1 was formed to show the data measured by two approaches as well as the corresponding P-value [139], which shows the significant difference between the two classes of samples. Considering the projection on Y (sample number) - Z (retardance) plane (Figure 5.8 (c)) and the P-values in Table 5.1 of either individual samples or the overall combination, it can be seen that the polarimeter is able to distinguish efficiently the

healthy and cancerous breast tissues. The difference between two kinds of samples is obvious across the tested samples; this also confirms the robustness of the polarimeter. Compared to the data measured by the MM microscope, larger standard deviations from the data measured by the GRIN lens cascade based polarimeter can be observed. The difference might result from the inhomogeneous sample structure in the effective FOV. To make the process more efficient and precise, detailed error analysis and corresponding optimization will be the subject of further work.

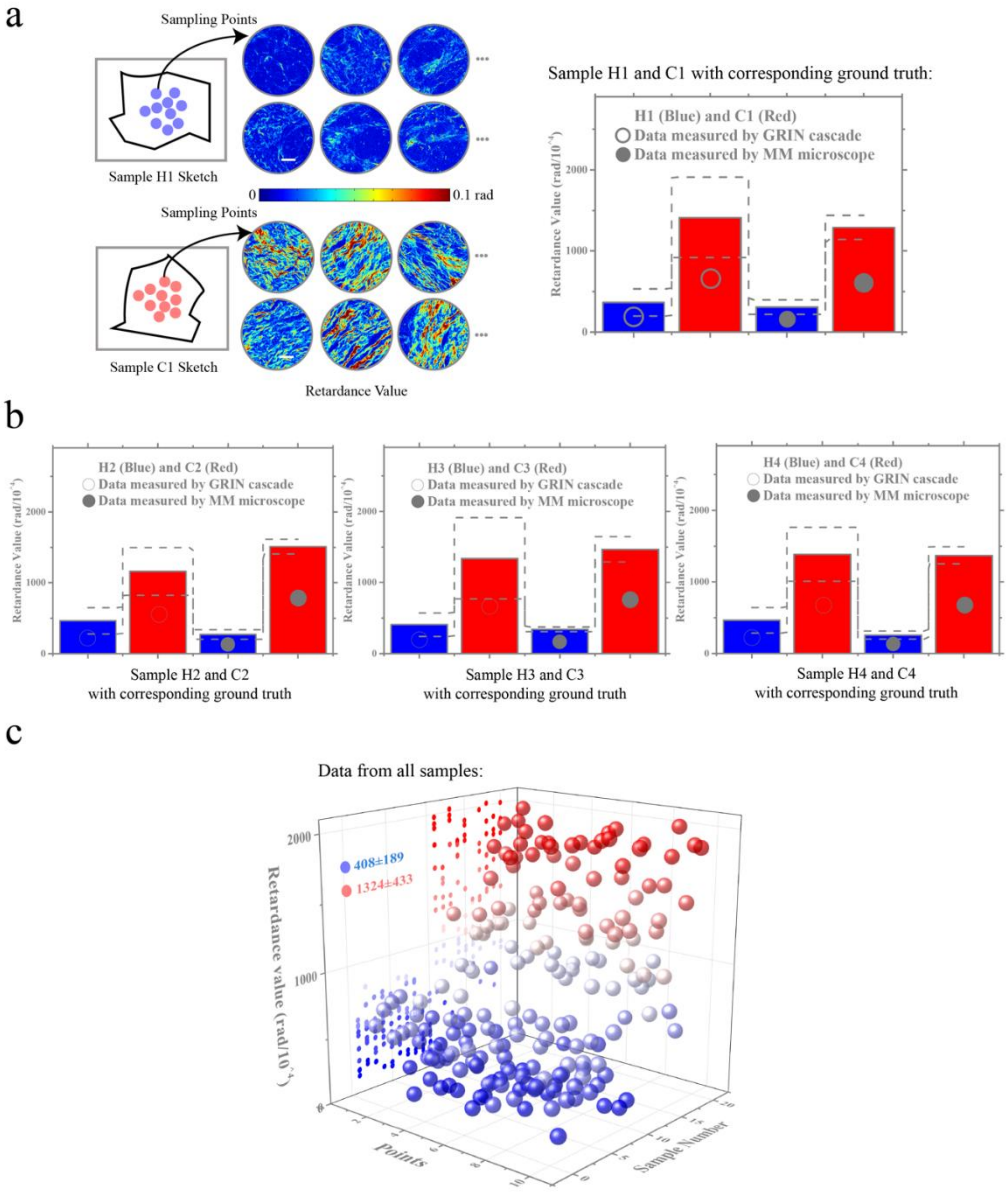


Figure 5.8 Statistical analysis. (a) Statistical histogram (mean value and the standard deviation of the retardance) of the 10 points from each sample (H1 and C1) within the same region, measured by the GRIN lens cascade and a conventional MM microscope. Standard deviations are shown via the dashed lines. Numbers refer to Table 5.1 (b) Demonstrations of statistical histograms (mean value and the standard deviation of the retardance) of different samples measured by the GRIN lens cascade and a conventional MM microscope (ground truth). (c) Overall data distribution (retardance value). The overall number of samples was 20 (half cancerous vs. half healthy, giving 10 testing points per sample). Note that blue (ball or histogram) represents healthy samples while red represents cancerous samples.

Table 5.1 Value of retardance δ (rad) of samples used in this section

	Slide H1 and Slide C1					Slide H2 and Slide C2				
	Healthy		*Cancerous*			*Healthy*		*Cancerous*		
	mean value	*standard deviation*	*mean value*	*standard deviation*	**P-value*	*mean value*	*standard deviation*	*mean value*	*standard deviation*	**P-value*
GRIN cascade	0.0365	0.0166	0.1412	0.0497	<0.001	0.0463	0.0185	0.1159	0.0338	<0.001
MM microscope	0.0309	0.0089	0.1289	0.0151	<0.001	0.0271	0.0067	0.1513	0.0104	<0.001
	Slide H3 and Slide C3					Slide H4 and Slide C4				
	Healthy		*Cancerous*			*Healthy*		*Cancerous*		
	mean value	*standard deviation*	*mean value*	*standard deviation*	**P-value*	*mean value*	*standard deviation*	*mean value*	*standard deviation*	**P-value*
GRIN cascade	0.0406	0.0164	0.1340	0.0573	<0.001	0.0464	0.0178	0.1385	0.0377	<0.001
MM microscope	0.0314	0.0033	0.1467	0.0179	<0.001	0.0257	0.0056	0.1371	0.0122	<0.001
	...					Combination of all slides				
	Healthy		*Cancerous*			*Healthy*		*Cancerous*		
	mean value	*standard deviation*	*mean value*	*standard deviation*	**P-value*	*mean value*	*standard deviation*	*mean value*	*standard deviation*	**P-value*
GRIN cascade	…					0.0408	0.0189	0.1324	0.0433	<0.001
MM microscope						0.0323	0.0102	0.1279	0.0171	<0.001

*the P-value is obtained by the significance test method [139] (P<=0.05 is significant), which shows the significance of the difference between the two sets of data.

5.4 Summary and discussion

In this chapter, a new type of single-shot MM polarimeter is proposed based on GRIN lens cascade. It consists of a spatially engineered polarising component array as a polarisation state generator and a GRIN lens cascade based polarisation state analyser. By taking advantage of the spatially varied birefringence of a GRIN lens, the polarimeter was explored to analyse multiple Stokes vectors simultaneously and was further developed into a snapshot MM polarimeter. This new GRIN lens cascade based MM polarimeter is robust, stable, and easy to construct. Especially it is static and has the potential to be miniaturized to adapt to minimally invasive surgery environments. Some single-shot MM polarimeters have already been proposed in previous studies

[71, 81], their technique is mainly based on sacrificing the spectral domain or spatial domain to enable the single-shot MM measurement [71, 81]. Our technique based on the spatial segmented method as well. As taking advantage of an unexpected property of the GRIN lens, the system is designed for imaging and minimizing mass and size for future use – which are the specific characteristic/advantage of our technique. The device was validated on standard samples, and the results demonstrated that the polarimeter could measure point MM of an object in a snapshot with promising accuracy and robustness. To show its potential biomedical applications, human breast ductal carcinoma and healthy tissue slices were used to test the polarimeter with the results compared to those acquired using an established MM microscope. We also showed that the polarimeter can distinguish the cancerous human breast tissue samples from healthy ones efficiently in a single-shot, without requiring any use of exogenous contrast agents. For its future prospects, it actually has the potential for wide field or scanned imaging, possibly in combination with fibers. The demonstrations in this chapter were performed at a single wavelength, but could be expanded to multiple wavelength channels polarimetry, while still maintaining optimal MM measurement for each wavelength.

Chapter 6

Vectorial adaptive optics enhanced GRIN lens system

6.1 Vectorial adaptive optics

Previous Chapters focused on that understanding and harnessing the unexpected birefringence via using GRIN lenses in cascade with other optical components to enable extra functionality in commonplace GRIN lens systems. Chapter 3 presented new research aspects via investigating the optical properties of GRIN lens cascades themselves; Chapter 4 showed how we can turn GRIN lens cascade into a new beam generator; Chapter 5 demonstrated that GRIN lens cascade can act as a new beam analyser with specific passive components. In this Chapter, we change the point of view back to focus on the GRIN lens imaging systems (GLSs) themselves. Through better understanding of the vectorial modulation effects of the birefringence, we used active optical components in cascade with GRIN lens to mitigate against the related aberration (polarisation and

phase) problems in current GRIN lens-based micro-endoscopy systems, in order to improve their imaging quality. The blue dotted circle in Figure 6.1 below visualizes the position of this Chapter.

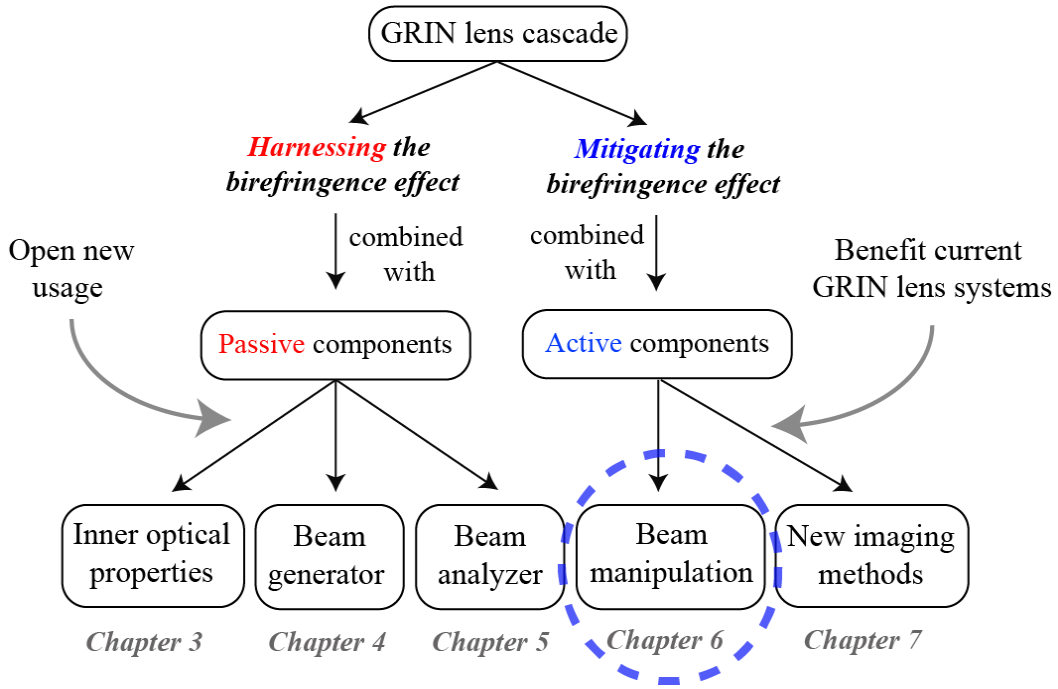


Figure 6.1 Relationships between the Chapters. Brief structure of relationships between every Chapter in this thesis. Blue dotted circle represents the topic that we will discuss and investigate in this Chapter.

6.1.1 Phase correction with traditional adaptive optics

Adaptive optics (AO) is becoming an ever more powerful technology for microscopy/micro-endoscopy and many scientists are now combining AO into their existing microscopes/micro-endoscopes with specific applications [162, 168]. In practice, performance of the microscope/micro-endoscope is affected by the optical properties of the optical elements and the specimen (especially in thick tissue imaging such as deep brain imaging) induced aberrations [162, 168]. These aberrations detrimentally affect the resolution and contrast of the obtained images –

limiting the sample information that imaging can tell [162, 168]. Therefore, AO is introduced into those areas in order to overcome the aberrations and associated imaging distortion [162, 168]. Ever since the early 2000s [168, 169], adaptive optical microscopy/micro-endoscopy has been implemented and more and more innovative advances that set the scene for various research applications [170-180]. Various dynamic correction elements have been used to implement AO – such as deformable mirrors (DMs), spatial light modulators (SLMs), digital micromirror device (DMD) and transmission fluidic-based device (TFD) [170-180]. These methods have been widely used to compensate the phase aberration induced by imperfect optical components and/or samples. It should be noted that both open-loop and close-loop control systems were presented in previous AO involved research. Definitions of those two types can be found in Ref [162, 176].

6.1.2 Polarisation correction with polarisation adaptive optics

AO is usually thought of in terms of the feedback correction of phase aberrations [162]. However, there are many optical microscopy/micro-endoscopy systems where perturbation in the polarisation state can have detrimental effects. For certain specific microscopy/micro-endoscopy systems, polarisation aberrations also have a great influence on the system performance [173, 174]. In single molecule microscopes, such as photoactivated localization microscopy (PALM), stochastic optical reconstruction microscopy (STORM), sparse deconvolution of polarisation-modulated fluorescent images (SPOD) or super-resolution dipole orientation mapping (SDOM),

the emitting dipole orientation is easily affected by polarisation aberrations [173, 174]. In stimulated emission depletion (STED) and structured illumination microscopy (SIM) systems, polarisation aberrations would cause the non-zero intensity in the centre of the depletion beam or affect the interference pattern stability [173, 174]. In GRIN lens endoscopic systems, polarisation aberrations also contribute to unexpected axial resolution and distortion of the output vectorial light field [31].

It should be noted that there are several reasons why spatially varying polarisation aberrations may be introduced in an optical system: for example, unexpected cases that can be acted as the existence of extra components – such as extra retarders (sample induced), extra diattenuators (sample induced), extra depolarisers (imaging issues) [181-186]. Fresnel effects at surfaces can modify the polarisation states of beams as well; these effects may be particularly significant at high angles of incidence. Specifically, through interfaces between the cover glass and immersion or mounting media (including both thin tissue in transmission mode and bulk tissue in back scattering mode), Fresnel effects would also contribute to the system polarisation aberrations [181-186]. Therefore, adaptive control of the polarisation state would be of great benefit in those cases. Previous research showed that close-loop systems have huge advantageous in microscopy/micro-endoscopy systems [162]. For this, we would like to implement polarisation adaptive optics technique with three fundamental components: 1) a method for measuring the

polarisation state across a beam profile, 2) a method for controlling the polarisation state, and 3) a strategy for feedback control. The first preliminary demonstration of close-loop adaptive polarisation control to correct the extrinsic polarisation aberrations via the above methods was presented by our group – detailed theoretical formulism and experimental demonstrations can refer to Ref [174].

6.1.3 Phase and polarisation correction with vectorial adaptive optics

As polarisation aberration and phase aberration are both crucial in many microscopy/micro-endoscopy systems, full correction of these errors is essential to obtain optimal performance of these systems. For this purpose, we present here the concept of vectorial adaptive optics (V-AO) to extend the traditional phase-based AO techniques into vectorial beam domain (with both phase and polarisation). In the latter section 6.2, we would introduce two full polarisation and phase controlled geometries and chose the proper one to implement. We demonstrate that full vectorial beam control can be implemented via a combined spatial light modulators (SLMs) and/or deformable mirror (DM) system. We also present in further section that V-AO can manipulate/improve the point spread function (PSF) performance of the GRIN micro-endoscope. The enhancement of the normal/vectorial PSF performance validated that our technique may solve numerous optical residual error issues in microscopic/endoscopic imaging systems.

6.2 Vectorial adaptive optics correction system

AO elements can be polarisation sensitive, such as SLMs [173], or polarisation insensitive, such as DMs, DMDs or TFDs. We put forward a sequential model as shown in Figure 6.2 according to Ref [173]. This consists of a sequence of AO elements positioned along the beam path at normal incidence, such that the distance between the devices is small enough so that diffraction effects between elements can be negligible. We note also that similar operation could be achieved if suitable 4F imaging systems are used between each pair of AO devices, although they are omitted here for clarity. And in this section we focus on the manipulation of a uniform fixed state to any arbitrary state. We make the approximation here that all beams are at normal incidence and the illumination is assumed to be a collimated beam of monochromatic, fully polarised light, although the polarisation state may vary across the beam profile.

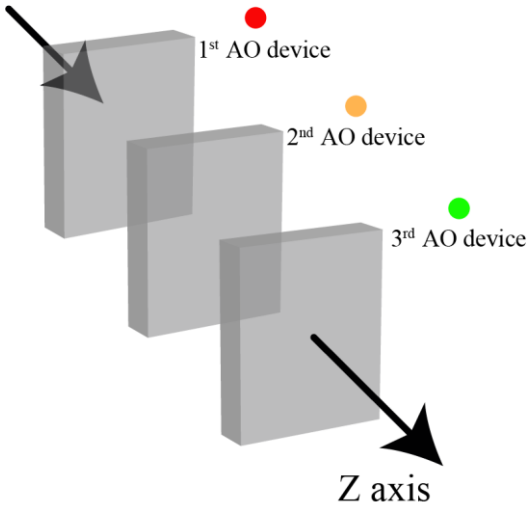


Figure 6.2 Schematic of the multiple AO elements system. A three pass system is presented for full polarisation and phase control. Note in this section we introduce a V-AO control model and for clarify, we

simplify all components into transmission mode to explain the feasibility to generate arbitrary states using combinations of AO devices.

6.2.1 Spatial light modulator based geometry

Several methods have been developed for the generation of arbitrary states using combinations of SLMs [162, 173, 174]. The simplest of these methods consist of consecutive passes through multiple SLMs. In practice, this may be implemented in an equivalent way by passing the beam through different regions of the same SLM [174]. We briefly introduce here a widely used system that generates a defined polarisation and/or phase state from a known input. The input beam is chosen to have a uniform, linear polarisation. For generation of arbitrary polarisation and phase states, a minimum of three SLM modulations is required (as shown in Figure 6.3), as the transition in polarisation state requires two free variables, and phase requires one free variable.

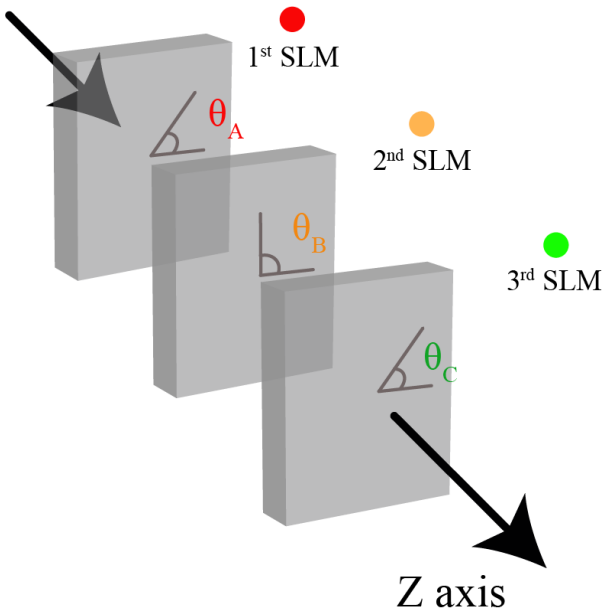


Figure 6.3 Schematic of the multiple SLM system. The modulation axis of each SLM is set at a chosen angle θ_A, etc.

In the optimal configuration, the input polarisation state is fixed in 45° linear polarised. The first SLM is used for phase modulation and the rest two are for full polarisation modulation capability – the extraordinary optical axis of the second SLM must be oriented at 45° to the polarisation state of the input light. The third SLM is then oriented at 45° to the second SLM. On the Poincaré sphere, the action of the second SLM is to move the polarisation state along a great circle (see Figure 6.4); the third SLM then moves the state along a circle in a perpendicular plane to the plane of the second SLM path. These two transitions can reach any point on the sphere and hence permit the generation of any polarisation state. Although we have assumed that all SLMs are capable of full $\pm\pi$ radians retardance, this same modulation range could also be achieved if the third SLM was limited to $\pm\pi/2$ radians. Note that if the orientation of either SLM is not perfectly aligned, the paths on the Poincaré sphere will not be in perpendicular planes, so there will be regions of the sphere that cannot be reached; hence, there will be polarisation states that cannot be generated by the system. For more details refer to Ref [173].

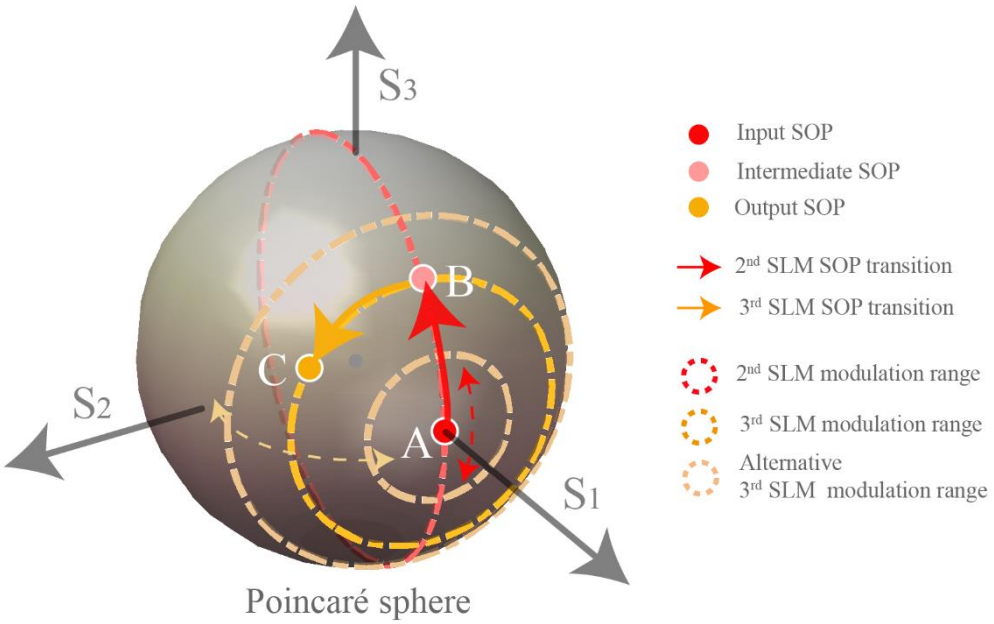


Figure 6.4 State of polarisation (SOP) transitions on the Poincaré sphere for the latter two SLM system. S_1, S_2 and S_3 are the axes representing the Stokes vector components. Point A represents the linear polarised input state; point B is the state after the first SLM; point C shows the output state. Variation of the retardance of the two SLMs permits the translation of point C to any point on the surface of the sphere.

6.2.2 Spatial light modulators and deformable mirror based geometry

The previous design in section 6.2.1 is fully SLM based. The phase is modulated via the first SLM. Alternatively, we could also use a DM as the phase modulator. The structure is shown in Figure 6.5. The actions of the first and second SLM are to move the polarisation state along different circles on the Poincaré sphere are visualized in Figure 6.4.

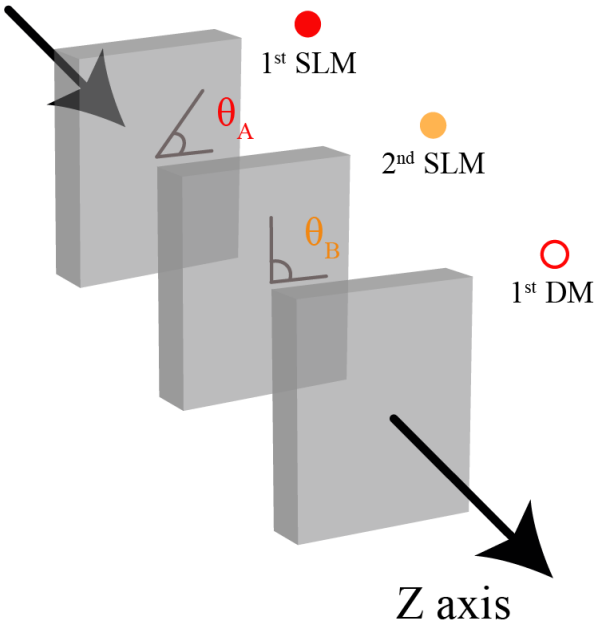


Figure 6.5 Schematic of the multiple SLM and DM system. The modulation axis of each SLM is set at a chosen angle θ_A, etc.

It should be noted that as the DM is polarisation insensitive, under our theoretical model there is no place preference for the DM. In the work below (for the demonstration of V-AO enhanced GRIN lens system), we use DM instead of the third SLM considering the system stability (such as polarisation insensitivity) and device availability in the laboratory.

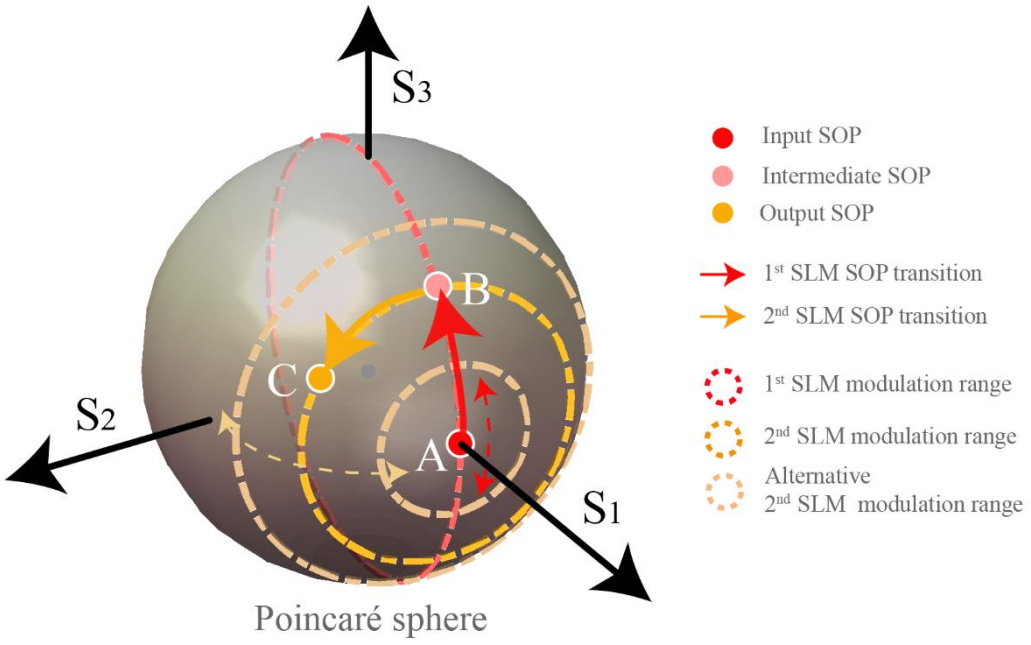


Figure 6.6 SOP transitions on the Poincaré sphere for the first and second SLMs. S_1, S_2 and S_3 are the axes representing the Stokes vector components. Point A represents the linear polarised input state; point B is the state after the first SLM; point C shows the output state. Variation of the retardance of the two SLMs permits the translation of point C to any point on the surface of the sphere.

6.3 Vectorial adaptive optics correction in GRIN lens system

6.3.1 System confirmation

As we have mentioned in the end of Chapter 4, the complex intrinsic birefringence of a GRIN lens imaging system indeed sets barriers for its performance and also prevents the development of new imaging methods. Here, with the help of V-AO, we give a possible solution to improve the GRIN system performance (this Chapter) and future prospects (Chapter 7). The system for the demonstration is presented below both schematically (Figure 6.7) and in practice (Figure 6.8).

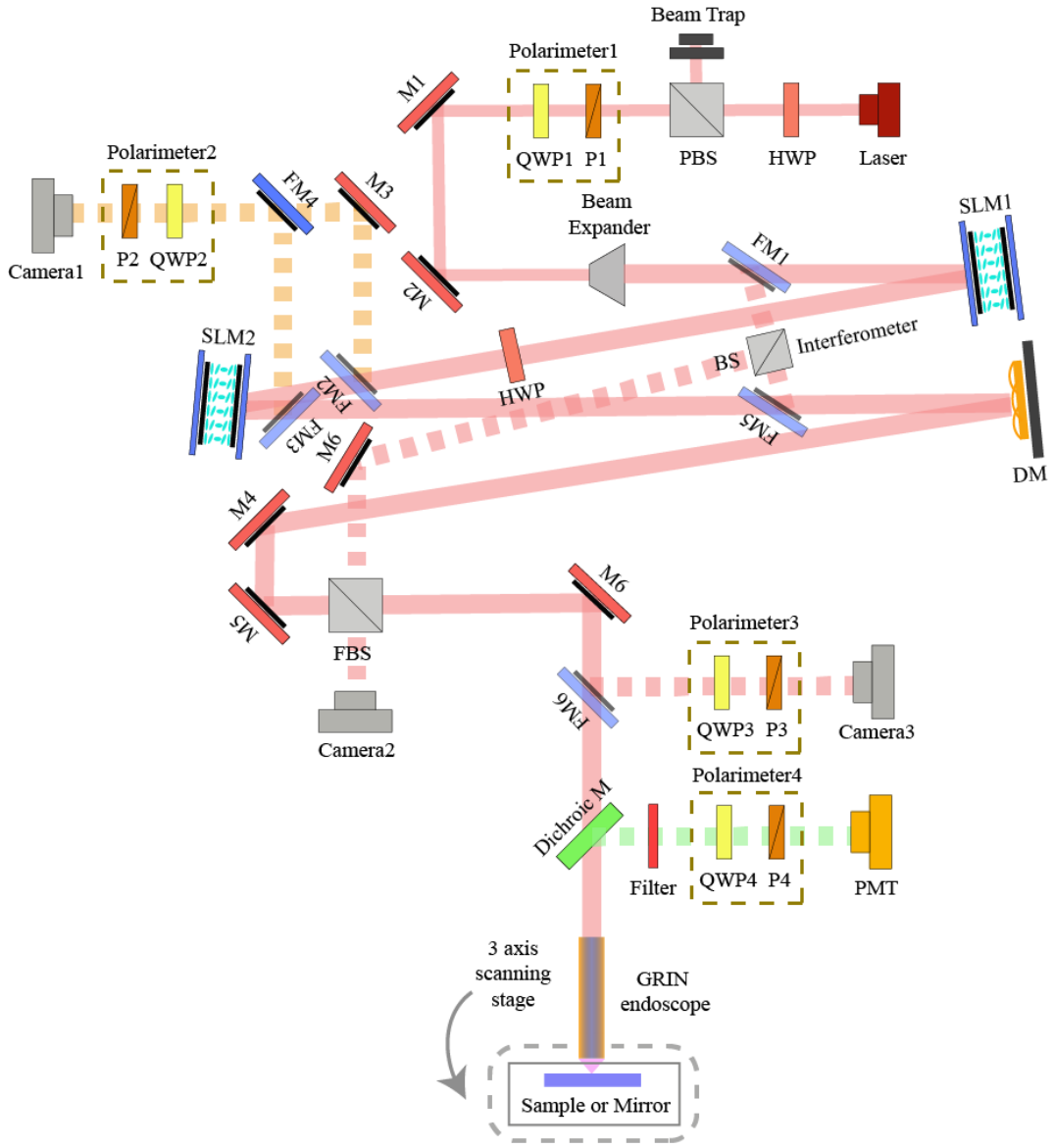


Figure 6.7 Sketch of the GRIN endoscopy system. Details and functionalities of the components can be found in the related paragraphs in the main text.

The system is mainly a GRIN lens based endoscopic system. The light source is a He-Ne laser (linear polarised output), the linear polarisation orientation is modulated by a half wave plate (HWP) and the intensity is modulated via the polarisation beam splitter (PBS). The original *polarimeter 1* in the system is used as polarisation state generator (PSG) to generate any arbitrary

uniform polarised light fields and also is capable of measuring the polarisation errors of different optical path lengths chosen from the system. The PSG compromises a polariser (P1) and a quarter wave plate (QWP1). All abbreviations M and FM in the sketch represent mirror and flip mirror, respectively. SLM1 and SLM2 are used to modulate the polarisation state of the light beam and the DM controls the phase. MF 2 and 3 are used to bypass the rest of the system to do in situ polarisation calibration of the SLMs via *polarimeter 2*. More details of this calibration method can be found in Ref [75-78]. An *interferometer* is constructed by FM 1, FM 5, M6, beam splitter (BS), flip beam splitter (FBS) and a camera. It is used to do in situ calibration of the DM. In this method, we use a silver mirror placed in the focus of the objective lens [175]. The light passes through the objective, reflects from the mirror, then passes back through the objective before reaching the sensor. This ensures that the aperture of the lens is used as the reference aperture in the system. After modulating via SLM1, SLM2 (polarisation), and DM (phase), the modulated beam is conjugated to the back pupil of GRIN lens, hence enabling any arbitrary vectorial beam state control at pixel level. Another *polarimeter 3* is conjugated to the pupil as well, acting as a polarisation state analyser (PSA)/polarisation sensor. The system includes transmission imaging ability (the illumination path via incoherent light source is not shown in Figure 6.7), and also is capable of scanned imaging via moving the 3-axis piezo stage, such as for future implementation of reflection or fluorescence confocal microscopes. The dichroic mirror and filter are used to

select the emission light of the targeted fluorescence beads, which is finally captured by the photomultiplier tube (PMT). The *polarimeter 4* (an alternative optional assembly) can provide the function to do further polarisation information extraction. It also should be noted that the necessary 4F imaging systems (shown in Figure 6.8) are omitted here (in Figure 6.7) for clarity.

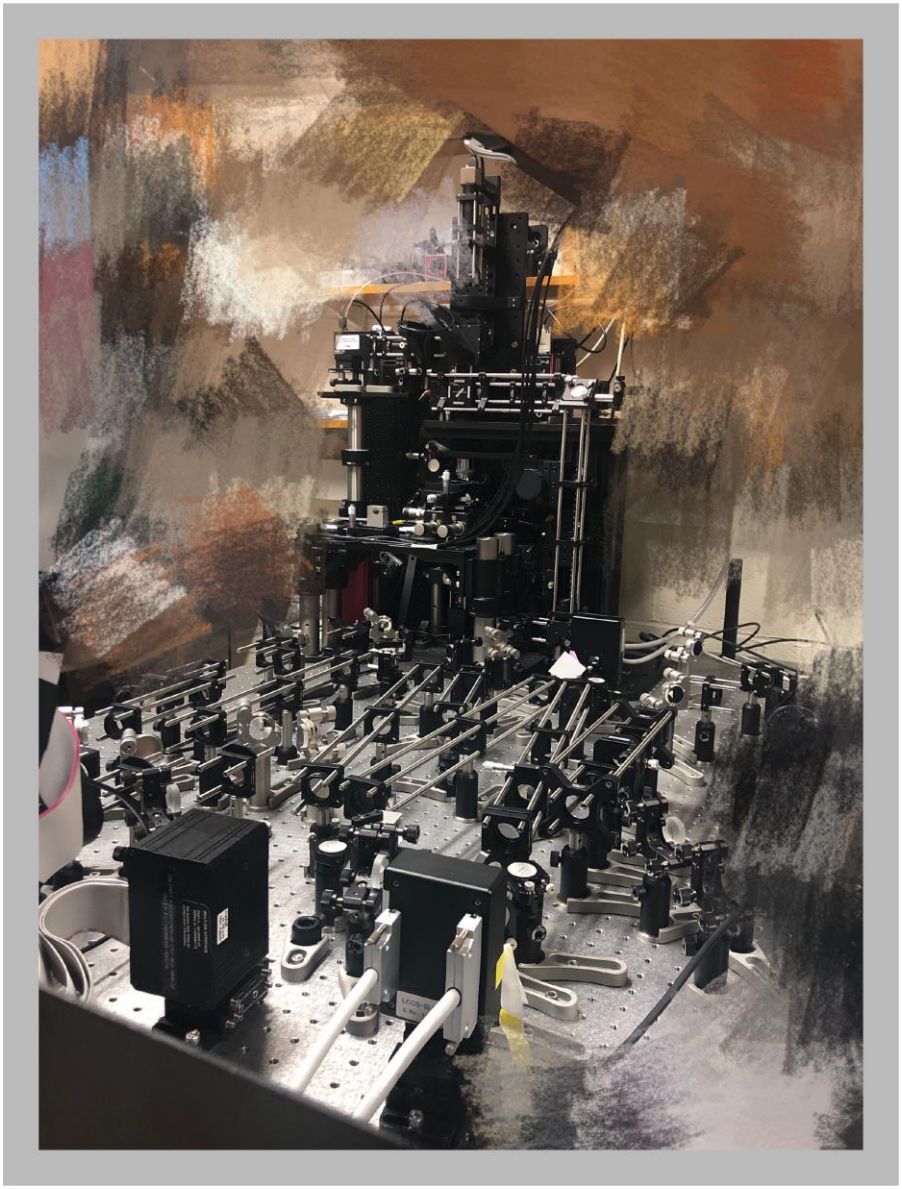


Figure 6.8 The GRIN endoscopy system. The whole experimental system in the lab that was shown schematically in Figure 6.7.

6.3.2 Adaptive polarisation closed-loop correction

Section 6.1.2 briefly explained the concept of polarisation adaptive optics (P-AO). There exist a few works that demonstrated closed-loop correction for intrinsic or extrinsic polarisation aberrations [174]. However, previous research on system polarisation aberration has only focussed on 1) overall performance without detailed analysis of specific components; 2) polarisation insensitive microscopy/endoscopy methods; 3) small polarisation distortion of the beam [174, 187]. In this section, we demonstrate the P-AO closed-loop correction with applications in analysing/correcting polarisation aberrations induced by specific components – a tilted vortex wave plate and a GRIN lens. Misalignments and the intrinsic birefringence create polarisation distortions that are crucial for polarisation related applications [181-187]. We only consider pupil domain analysis in this section; focal domain analysis will be followed later.

6.3.2.1 Tilted vortex wave plate

A spatially variant wave plate (SHWP) array is a widely-used polarisation optical component. Its applications span across quantum optics to classical optics [42, 147]. A key usage is to do vectorial beam shaping [42, 147]. We also explored its new usage in Chapter 4 as a potential part of components that can be adopted in modifying the axial PSF performance of GRIN endoscopic systems with respect to the generated vector fields. However, in practice, the misaligned SHWP

can be a problem affecting the expected output beam profile. To conquer that problem – especially for the occasions that SHWP is integrated in a system that could not be modified easily – we use P-AO system to do such aberration compensation. In our system (shown in Figure 6.7), we used polarisation sensors to detect and estimate the polarisation distortion induced by the misalignment of the SHWP. The SHWP was tilted (θ=3 degrees with respect to normal plane) and placed into the conjugate plane of the pupil of GRIN lens.

Figure 6.9 (a) shows the simulated theoretical polarisation properties of the SHWP (in the form of the MM) and the corresponding output beam profile using linear polarized light incidence (0 degree with respect to the defined coordinate system). The generated beams of the tilted SHWP with/without the help of P-AO are shown in Figure 6.9 (b). As we can find from the results of P-AO on and P-AO off, the corrected vector beam profile is closer to the theory. A sampled distribution of polarisations along a random L-line of the beam is chosen in order to estimate the quality of correction [31]. The demonstration of the quantitative Stokes vector error analysis showing on Poincaré sphere is also given (Figure 6.9 (c)) (method refers to Ref [31]). The mean measurement errors of parameters S'_1, S'_2 and S'_3 are 2.6%, 2.9% and 3.2% respectively (normalized by S'_0) (refer to section 4.1.1.2 for the method of comparing the symmetric properties

of the vector beams). This demonstration showed that the induced system polarisation errors can be corrected to a certain degree.

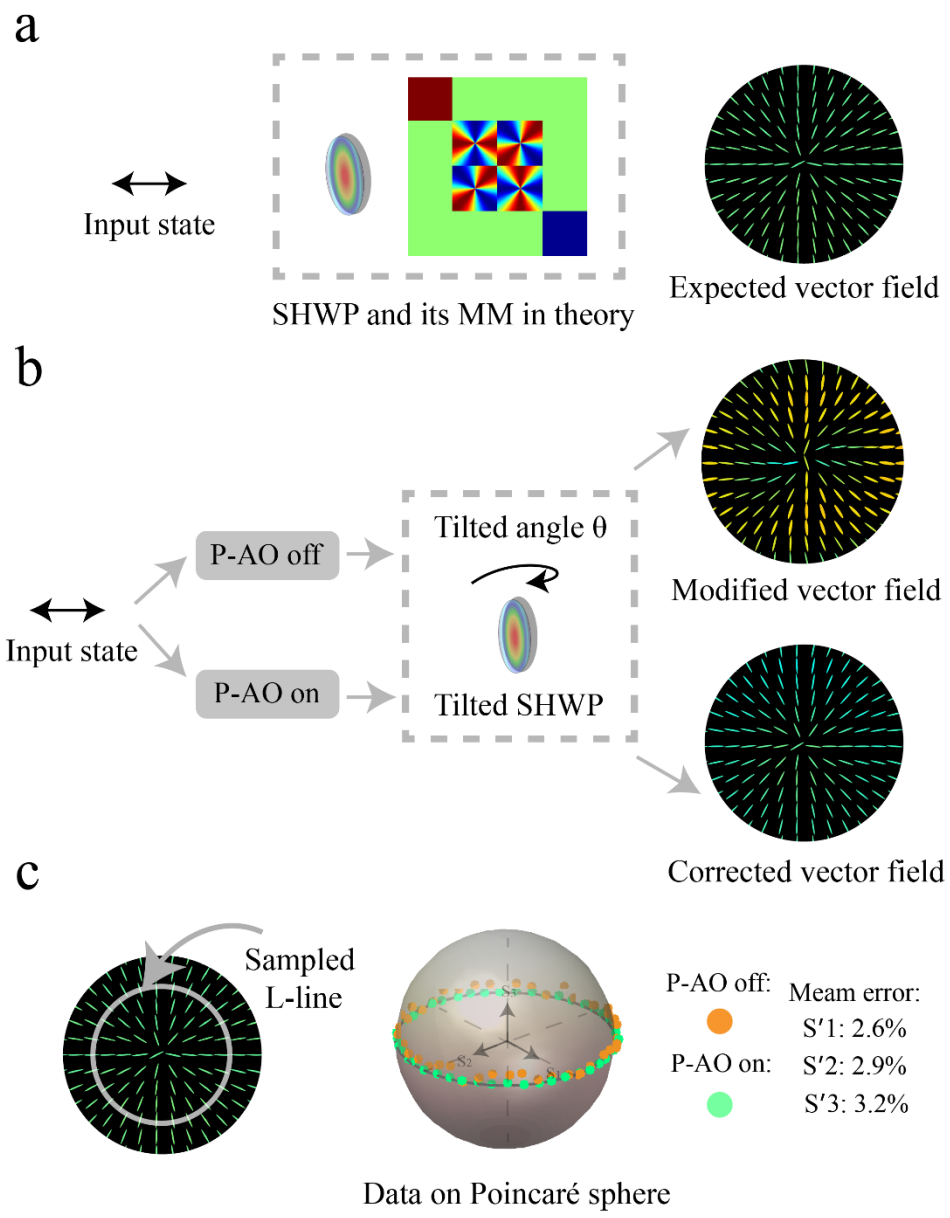


Figure 6.9 Polarisation correction for the tilted vortex wave plate case. (a) MM of SHWP in theory with the expected output vector beam. (b) The vector beams generating via the tilted vortex wave plate (θ=3 degrees with respect to normal plane) without/with P-AO correction. (d) Stokes vector error analysis with visualizations on the Poincaré sphere.

6.3.2.2 GRIN lens

As we discussed in above Chapters, through understanding the intrinsic birefringence of the GRIN lens, it can open many new usages. However, the basic function of the GRIN lens is an imaging device – it is also widely used in lots of endoscopic systems with their various biomedical applications [23-26，188]. In traditional GRIN imaging systems, the birefringence would lead to unexpected phase and polarisation aberrations [188]. Here, with the help of P-AO, we are able to control the polarisation state of the illuminated light fields on the pupil domain of GRIN lens, then further control the light fields in its focal domain (next section). That would provide a great opportunity to overcome aberration issues of existing GRIN endoscopic systems and then pave the way to new imaging methods for GLSs (refer to Chapter 7). To the best of our knowledge, the adaptive correction of the polarisation aberration in GLS has never been demonstrated. It should also be noted that, as the polarisation aberration can be the main aberration source when using GRIN lens to do vector imaging such as polarisation endoscopic imaging [188]. So even only polarisation aberration correction (regardless of phase aberration) for GLSs can already benefit many existing imaging methods.

Figure 6.10 (a) shows the MM of a low numerical aperture (NA=0.1) objective lens which is comparable of the MM of free space and the expected output beam using right hand circular

polarised light incidence (generated via the whole PSG). The generated beams of GRIN lens with/without the help of P-AO correction are shown in Figure 6.10 (b). The correction process follows the process in Ref [174]. The difference between the generated beam profiles that with P-AO *on* and *off* are significant. The P-AO corrected output beam is closer to the expected beam performance. Then, we chose the L-line of the full Poincaré beam that generated by GRIN lens (NA=0.1, details refer to Chapter 3) as a determination of the same spatial location on GRIN lens surface to quantify the Stokes vector correction precision (before and after P-AO correction). Quantitative Stokes vector error analysis and data distribution on the Poincaré sphere are given in Figure 6.10 (c) following the same process that had been adopted in the previous section. The mean measurement errors of parameters S'_1, S'_2 and S'_3 are 3.3%, 1.9% and 2.5% respectively (normalized by S'_0) (refer to section 4.1.1.2 for the method of comparing the symmetric properties of the vector beams). This demonstration showed that the polarisation errors were corrected in a good manner.

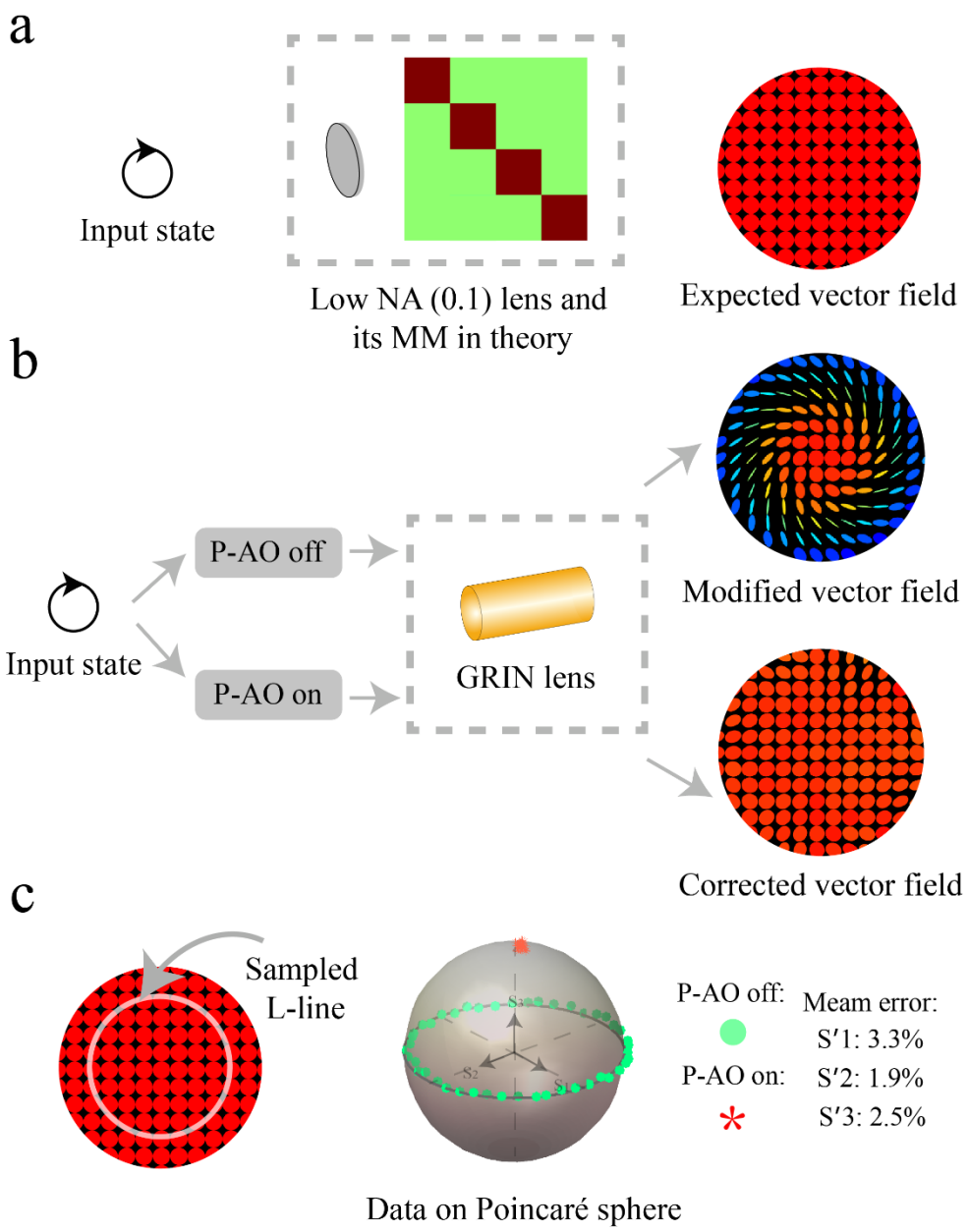


Figure 6.10 Polarisation correction for the GRIN lens. (a) MM of a low NA lens in theory and the corresponding output vector beam. (b) The generated vector beam profiles without/with P-AO correction after passing through the GRIN lens. (d) Stokes vector error analysis with corresponding data on the Poincaré sphere.

6.3.3 Vectorial adaptive optics for point spread function modulation

6.3.3.1 Point spread function modification (polarisation only)

The PSF determines the resolution of the imaging systems (such as in various florescence microscopes/micro-endoscopies), and the properties of the focus also affects the vector field reconstruction properties (such as in second/third harmonic generation (SHG/THG) microscopes) [172]. In section 6.3.2.2 we discussed the vector beam modulation/correction in the pupil domain of GLS. Here we focus on the analysis in the focal domain of the GLS. As first step, we demonstrated full polarisation correction using P-AO, and in section 6.3.3.2 we apply V-AO correction including phase, both via simulation.

Figure 6.11 (a) shows the theoretical lateral PSF of the GRIN lens (related optical parameters such as laser wavelength are determined by the system in Figure 6.7) without the birefringence effect. It shows the intensity distribution with a 0 degree linear polarised illumination. Figure 6.11 (b) shows the theoretical lateral PSF when modulated by the birefringence. Figure 6.11 (c) shows the PSF after P-AO on state (polarization correction). It can be found that even after the polarization error correction (i.e., when P-AO is applied), the intensity distribution of the PSF contains non-neglectable differences if compared to theory. One of the reasons is that there were additional induced phase aberrations introduced by the compensation devices and GRIN lens themselves (via a geometric phase effect) [31], which also modified the PSF profile. Thus, the implementation of full polarisation and phase correction (V-AO) is critical for the performance of those GRIN endoscopic systems.

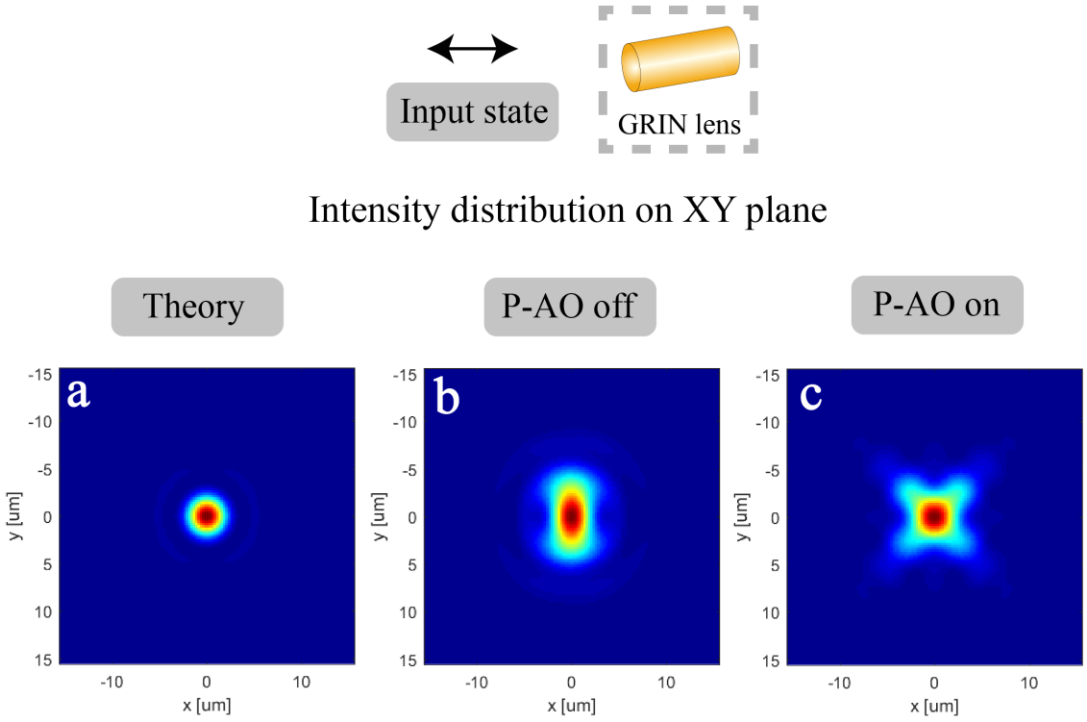


Figure 6.11 Vector state correction of the PSF of GRIN lens system. (a) PSF in theory. (b) PSF obtained at the state of P-AO off. (c) PSF obtained at the state of P-AO on.

6.3.3.2 Point spread function modification (polarisation and phase)

In this section, we show the simulation results applying full V-AO method to control the PSF of GRIN endoscopic system. The above section only focussed on polarisation errors; now the dimension of phase is also included. Theoretically, the phase aberrations could occur from various sources: system phase aberration such as unexpected spherical aberration induced by 4F imaging lenses; sample phase aberration due to refractive index mismatch; geometric phase induced by retarders (SLMs or GRIN lens itself) in the systems. However, in the real experimental case, we will apply sensor-less AO method to perform phase correction, so all the phase aberrations can

be packaged and corrected via a single device [162]. Based on the progress demonstrated in previous section, we tried here to add the dimension of phase correction to compensate the geometric phase induced aberration. Figure 6.12 (a) shows the theoretical PSF intensity profile. Figure 6.12 (b), (c) show the PSF profiles for both states of V-AO on and off. It can be clearly found that the intensity profile of the PSF is improved in Figure 6.12 (c) compared with (b).

So far, we have given a preliminary demonstration that V-AO enhanced GRIN endoscopic system can have better system performance compared with the same endoscopic systems without V-AO. The experimental validation and detailed quantitative analysis of the vectorial aberration correction process of the V-AO enhanced GRIN endoscopic systems will obviously be next step of our work. With these improved methods of vectorial fields manipulation, we believe it would also pave the way for the development of new imaging methods through GRIN lens systems (details in Chapter 7).

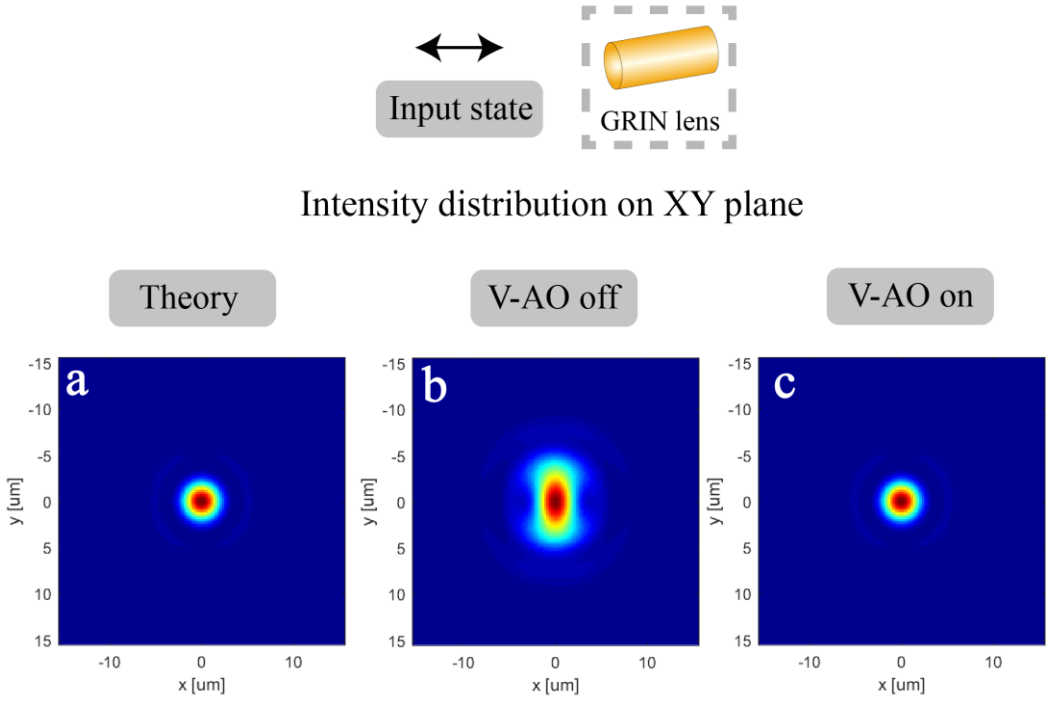


Figure 6.12 Vectorial state correction of the PSF of GRIN lens system. (a) PSF in theory. (b) PSF obtained at the state of V-AO off. (c) PSF obtained at the state of V-AO on.

6.4 Summary and discussion

In this Chapter, based on previous understanding of the intrinsic birefringence of the GRIN lens, we now aim to mitigate the birefringence effects (polarisation and phase aberrations) of the GLSs with the help of V-AO (including P-AO), so that we can improve the performance of the current GLSs. We first presented a three pass modulation structure to show the ability to fully control the phase and polarisation state of the beam via multi-AO devices, then we briefly explained the three SLMs configuration and two SLMs with a DM configuration. Using the latter configuration, we built a V-AO enhanced GRIN endoscopic system. Preliminary demonstrations of the correction of the polarisation aberration (using P-AO) were shown both in pupil domain and focal domain

of GRIN lens. This is already important for the related precision vector field imaging methods such as GRIN lens based endoscopic polarisation imaging [29, 30]. Last, with full polarisation and phase control of the illuminated beam (using V-AO), we showed simulations that we can compensate the polarisation and phase aberrations that were induced by the intrinsic birefringence of GRIN lens to enhance the performance of the PSF. Shaped/enhanced PSFs have been demonstrated and analysed by comparison to their theoretical counterparts (i.e., those without birefringence effects). All validations in this Chapter can not only benefit normal or vectorial GRIN based imaging methods, but also be useful for opening up new imaging methods for GRIN endoscopic systems, as will be discussed in Chapter 7.

Chapter 7

Conclusion, future work and discussion

7.1 Conclusion and future work

The work in this thesis focuses on studies about how to understand and take advantage of previously unwanted birefringence in the GRIN lens. In particular, we studied, both theoretically and experimentally, that a single unit or a cascade of GRIN lenses can be used to investigate the asymmetric Müller matrix of the multi-layer birefringence/diattenuation systems, and demonstrate the spin-Hall effect of light (SHEL) that can be harnessed in a GRIN lens cascade when symmetry breaking happens (Chapter 3). The GRIN cascade can also generate a variety of vector vortex beams – vectorial light fields that feature complex phase and polarisation properties normally containing singularities. It is quite surprising that there still exists off-the-shelf component that could generate structured light (Chapter 4). GRIN cascades can be used to analyse various polarisation states simultaneously, i.e., measure multiple Stokes vectors, which enables a

single-shot Müller matrix polarimeter. The instrument can comprehensively extract the polarisation characteristics of an object. We also demonstrated that when applied to a biological tissue sample this technique potentially offers a way to distinguish between healthy and diseased tissues based on an analysis of the sample's optical retardance properties (Chapter 5). Further demonstrations included some preliminary implementations of a new adaptive optics method to correct the aberration in those systems to enable new use of the traditional GRIN endoscope systems (Chapter 6).

There still exists several aspects that can be further investigated – such as analysing the SHEL inside GRIN cascades with multiple modulation components; such as analysing the OAM purity in vector vortex beams that generated through GRIN lens cascades; such as minimizing the MM polarimeter into a probe and using back-scattering configuration to do further fast *in vivo* biomedical sample characterization and so on. But as a main follow-up of our work (an extension of Chapter 6), we will try to develop more complete new imaging methods of GRIN endoscopic systems through compensating its inner complex birefringence effects via the help of vectorial adaptive optics. We elaborate here on novel imaging methods that can be divided into two categories – fluorescence and label-free methods.

7.1.1 Novel fluorescence-based imaging methods using GRIN lens cascades

Considered as an imaging device in endoscopic systems, the majority of the imaging systems that feature GRIN lenses are fluorescence based [29, 30]. However, cutting-edge super-resolution microscopy methods [172] still have not been fully transferred into GRIN endoscopic systems for biomedical applications. As we discussed throughout the whole thesis, the complex birefringence inside the GRIN lens would definitely introduce non-neglectable polarisation and phase errors, which would actually destroy the expected light fields that are required in many super-resolution methods [31]. So, a deep understanding and analysis of those related vectorial effects would be an important basis of realising those imaging methods to endoscopic systems, especially with the help of vectorial adaptive optics. Our studies in this project give a new insight to transfer those existing super-resolution imaging methods into GRIN lens based imaging systems.

7.1.1.1 Micro-endoscope for stimulated emission depletion (STED) microscopy

As demonstrated at the end of Chapter 4, we noticed that there exist two eigenmodes of the GRIN lens – they are azimuthal and radial polarised light fields, and they suffer their own refractive index when propagating through GRIN lenses. To show this effect, we demonstrated the tiny beam split along the axial direction. This phenomenon is strongly related to the birefringence profile of the target GRIN lens – which means its pitch length, physical length and other

parameters would affect the splitting. There existed huge space for detailed investigations such as for the interaction of parameter A_o and A_e.

As far as we have validated, the split was demonstrated in long GRIN lens that used in a clinical instrument, such as rigid micro-endoscopic systems [188] – laparoscopes. It is likely that a future stimulated emission depletion (STED) based method can first be demonstrated on those imaging systems to show precision control of the point spread function, enhance lateral resolution and reveal potential applications. We plan to use vectorial adaptive optics (Chapter 6) to fully control the polarisation and phase of the incident beam and realize this method. Through Jones calculus (Eq. (7-1-1)) we could deduce that the target input beam profile (J_{in}) generated by vectorial adaptive optics system should possess pre-compensated polarisation and phase distribution when used for a depletion beam (J_{out}) in the STED method. The J_{GRIN} is the Jones matrix of the GRIN lens and J_{GRIN}^{-1} is the inverse matrix of J_{GRIN}.

$$\begin{aligned} J_{out} &= J_{GRIN} \cdot J_{in}, \\ J_{in} &= J_{GRIN}^{-1} \cdot J_{out}. \end{aligned} \tag{7-1-1}$$

The method is expected to at least have a better lateral resolution compared with previous GRIN endoscopic imaging systems, and has a great potential to be further developed as a 3D imaging method.

7.1.1.2 Micro-endoscope for structured illumination microscopy

Structured illumination microscopy (SIM) is widely used in various biomedical research with advantages such as fast imaging speed, low illumination power, high resolution – especially for *in vivo* imaging [163, 172]. Here, through a better understanding of the intrinsic birefringence and aberrations of GRIN lens (and cascades), with the help of vectorial adaptive optics, we could now calculate and modulate the input light fields (input beams) in the back pupil of GRIN lens to create interference patterns in its focus plane, which enable SIM imaging. The corresponding modulation can be described mathematically in the same way as shown in Eq. (7-1-1). Of course, the polarisation modulation (via spatial light modulators (SLMs)) of vectorial adaptive optics is used to compensate the polarisation aberration; the phase correction is controlled by such as a deformable mirror (shown in Figure. 6.2, Chapter 6). This can also be used to compensate the geometric phase induced by SLMs as system phase aberrations, and furthermore, to compensate the phase aberration from the sample to enable deep SIM.

7.1.2 New label-free polarimetric method for GRIN lens cascade

Besides the fluorescence-based methods, with the help of vectorial adaptive optics, we could also enable new label-free imaging methods using GRIN lens cascades. These label-free methods

include second harmonic generation (SHG), third harmonics generation (THG) [189], polarisation sensitive harmonic imaging [189], and wide filed polarisation imaging [188]. Here, based on our studies on using the GRIN lens as a spatial functional polarisation state analyser, we could also establish further label-free polarimetric imaging methods. The latter two sections describe the new methods that extend polarimetric imaging in two other dimensions: spectral domain and space domain.

7.1.2.1 Multi-wavelength micro-endoscopy

GRIN lens and cascade can perform simultaneous Stokes vectors calculation, which is validated in Chapter 5) both theoretically and experimentally. And for different wavelengths, the optical paths inside the GRIN lens are different (as proved theoretically in Chapter 3), which gives us a chance to do single-shot multi-wavelength polarimetry, not only for simultaneous Stokes vector measurement but also for simultaneous Müller matrix measurement. One way to approach this is using a multi-channel detector such as a (short bandwidth) RGB colour detector that contains three channels, in which we could simultaneously obtain at least three wavelengths' information from the detector to extract their own polarisation. As the multi-wavelength technique (especially using RGB colour) has shown great potential in characterizing biomedical samples and revealing their inner microstructure information [172], the GRIN cascade based multi-wavelength polarimetry may open new methods for deep tissue label-free detection. An alternative method

takes advantage of the intrinsic chromatic properties of most GRIN lenses, which translate different wavelength information into different intensity patterns that incompletely overlap with each other onto the detector. We may recognize the intensity patterns recorded by the single detector directly to reveal different polarisation information of different wavelength. Further imaging analysis algorithms are required for the recognition of the partial overlapped intensity information.

7.1.1.2 Micro-endoscope with multi-layer scanning

Through understanding of the polarisation aberration and its interaction with phase aberration in GRIN lens system, with the help of vectorial adaptive optics, we will be able to apply a remote focusing technique [190] to perform axial scanning then enables endoscopic 3D label-free (such as SHG or THG) imaging. Also, the GRIN system can be used to analyse the polarisation properties of the emission light simultaneously. It should be pointed out that for Stokes vector measurement and analysis, the Stokes vectors information of SHG and THG signal are comparable to traditional Stokes vector analysis [191]; However, for Müller matrix measurement and its analysis on SHG and THG signal, high order Müller matrix should be considered [191, 192]. Those new imaging methods and analysis may pave a new way for novel *in vivo* biomedical (deep tissue) research.

7.2 Discussion

This thesis explains in detail the motivation, aim, current advance and future expectation of my work. However, possible opportunities (see above section 7.1) coexist with challenges. For example, for the existing explorations of the GRIN lens and its cascades, lots of detailed analyses are still required such as the relationship between refractive index profile and birefringence profile of GRIN lens, with respect to different ion-exchange processes. The related spin-orbital interaction (spin-orbital conversion and SHEL) process and geometric phase effect also need further investigation. For vectorial adaptive optics enhanced imaging methods, probably the optical designs and corresponding calculations for beam manipulations need to be tailored for different types of GRIN lens systems, and their targeted applications should also be taken into consideration (such as for shorter ones the split effect can be ignored in some cases but for longer ones the same effect cannot be neglected). I believe with confidence in the coming months or years of this project: we will finally be able to conquer the challenges and develop more interesting techniques. As an overall conclusion and outlook for this project: the optical properties of GRIN lenses and their combination in cascade with other optical devices provide a wealth of opportunity for further development in a wide range of applications, spanning from quantum optics to clinical diagnosis.

Reference

1. Hoad, T.F. The concise Oxford dictionary of English etymology. (Clarendon Press Oxford, 1986).
2. Morwood, J. & Morwood, J. A dictionary of Latin words and phrases. (Oxford University Press New York, 1998).
3. Zehr, H. Changing lenses, Vol. 114. (Scottdale, PA: Herald Press, 1990).
4. Lindberg, D.C. & Lindberg, D.C. Theories of Vision from al-Kindi to Kepler. (University of Chicago Press, 1981).
5. Steck, D.A. Classical and modern optics. *course notes available online at http://steck. us/teaching* (2006).
6. Guenther, B. Modern optics. (OUP Oxford, 2015).
7. Uluç, K., Kujoth, G.C. & Başkaya, M.K. Operating microscopes: past, present, and future. *Neurosurgical Focus* **27**, E4 (2009).
8. Hickie, W.J. The Comedies of Aristophanes: A New and Literal Translation from the Revised Text of Dindorf, with Notes and Extracts from the Best Metrical Versions, Vol. 1. (HG Bohn, 1859).
9. Glick, T.F., Livesey, S. & Wallis, F. Medieval science, technology, and medicine: an encyclopedia. (Routledge, 2014).

10. Watson, F. Stargazer: the life and times of the telescope. *Stargazer: the life and times of the telescope/Fred Watson. Cambridge, MA: Da Capo Press, 2005.* (2005).

11. Hilliam, R. Galileo Galilei: Father of modern science. (The Rosen Publishing Group, Inc, 2004).

12. Westfall, R.S. & Devons, S. (AAPT, 1981).

13. Steneck, N. The Light of Nature: Essays in the History and Philosophy of Science Presented to AC Crombie. JD North, JJ Roche. (1987).

14. Jorink, E. Reading the book of nature in the Dutch Golden Age, 1575-1715. (Brill, 2010).

15. Rosenthal, J.W. Spectacles and other vision aids: A history and guide to collecting. (Norman Publishing, 1996).

16. Seeger, R.J. Men of physics: Galileo Galilei, his life and his works. (Elsevier, 2016).

17. Koestler, A. & Durston, J. The watershed: a biography of Johannes Kepler. (Anchor Books Garden City, NY, 1960).

18. Dobbs, B.J.T. Newton's alchemy and his theory of matter. *Isis* **73**, 511-528 (1982).

19. Gomez-Reino, C., Perez, M.V. & Bao, C. Gradient-index optics: fundamentals and applications. (Springer Science & Business Media, 2012).

20. Moore, D.T. Gradient-index optics: a review. *Applied Optics* **19**, 1035-1038 (1980).

21. Merchand, E. Gradient index optics. (Elsevier, 2012).

22. Ghatak, A. (Tata McGraw-Hill, New Delhi, 2005).

23. Kim, J.K. et al. Fabrication and operation of GRIN probes for in vivo fluorescence cellular imaging of internal organs in small animals. *Nature Protocols* **7**, 1456 (2012).

24. Flusberg, B.A. et al. Fiber-optic fluorescence imaging. *Nature Methods* **2**, 941 (2005).

25. Barretto, R.P., Messerschmidt, B. & Schnitzer, M.J. In vivo fluorescence imaging with high-resolution microlenses. *Nature Methods* **6**, 511 (2009).

26. Pillai, R.S., Lorenser, D. & Sampson, D.D. Deep-tissue access with confocal fluorescence microendoscopy through hypodermic needles. *Optics Express* **19**, 7213-7221 (2011).

27. Reismann, D. et al. Longitudinal intravital imaging of the femoral bone marrow reveals plasticity within marrow vasculature. *Nature Communications* **8**, 2153 (2017).

28. Kampasi, K. et al. Dual color optogenetic control of neural populations using low-noise, multishank optoelectrodes. *Microsystems & Nanoengineering* **4**, 10 (2018).

29. Meng, G. et al. High-throughput synapse-resolving two-photon fluorescence microendoscopy for deep-brain volumetric imaging in vivo. *Elife* **8**, e40805 (2019).

30. Huland, D.M. et al. In vivo imaging of unstained tissues using long gradient index lens multiphoton endoscopic systems. *Biomedical Optics Express* **3**, 1077-1085 (2012).

31. He, C. et al. Complex vectorial optics through gradient index lens cascades. *Nature Communications* **10**, 1-8 (2019).

32. Rouke, J.L. & Moore, D.T. Birefringence measurements in gradient-index rod lenses. *Applied Optics* **38**, 6574-6580 (1999).

33. Camacho, J. & Tentori, D. Polarization optics of GRIN lenses. *Journal of Optics A: Pure and Applied Optics* **3**, 89 (2001).

34. Radwell, N., Hawley, R., Götte, J. & Franke-Arnold, S. Achromatic vector vortex beams from a glass cone. *Nature Communications* **7**, 1-6 (2016).

35. Marrucci, L., Manzo, C. & Paparo, D. Optical spin-to-orbital angular momentum conversion in inhomogeneous anisotropic media. *Physical Review Letters* **96**, 163905 (2006).

36. Devlin, R.C., Ambrosio, A., Rubin, N.A., Mueller, J.B. & Capasso, F. Arbitrary spin-to–orbital angular momentum conversion of light. *Science* **358**, 896-901 (2017).

37. Lai, W. et al. Generation of radially polarized beam with a segmented spiral varying retarder. *Optics Express* **16**, 15694-15699 (2008).

38. Booth, M.J. Adaptive optics in microscopy. *Philosophical Transactions of the Royal Society A: Mathematical, Physical and Engineering Sciences* **365**, 2829-2843 (2007).

39. Kumar, V., Philip, G.M. & Viswanathan, N.K. Formation and morphological transformation of polarization singularities: hunting the monstar. *Journal of Optics* **15**, 044027 (2013).

40. Wang, J. et al. Terabit free-space data transmission employing orbital angular momentum multiplexing. *Nature Photonics* **6**, 488 (2012).

41. Yu, N. et al. Light propagation with phase discontinuities: generalized laws of reflection and refraction. *Science* **334**, 333-337 (2011).

42. Zhan, Q. Cylindrical vector beams: from mathematical concepts to applications. *Advances in Optics and Photonics* **1**, 1-57 (2009).

43. Born, M. & Wolf, E. Principles of optics: electromagnetic theory of propagation, interference and diffraction of light. (Elsevier, 2013).

44. Thompson, B., Goldstein, D. & Goldstein, D. (CRC Press, 2003).

45. Rubinsztein-Dunlop, H. et al. Roadmap on structured light. *Journal of Optics* **19**, 013001 (2016).

46. Bass, M. Handbook of Optics, Volume IV: Optical Properties of Materials, Nonlinear Optics, Quantum Optics (set). (McGraw-Hill, 2009).

47. Bashara, N. Ellipsometry and polarized light. *Norht-Holland Publishin Company*, 235 (1977).

48. Huard, S. Polarization of light. *Polarization of Light, by Serge Huard, pp. 348. ISBN 0-471-96536-7. Wiley-VCH, January 1997.*, 348 (1997).

49. Tuchin, V.V. & Tuchin, V. Tissue optics: light scattering methods and instruments for medical diagnosis. (2007).

50. Brosseau, C. Fundamentals of polarized light. (Wiley, New York, 1998).

51. Goldstein, D.H. Polarized light. (CRC press, 2016).

52. Berry, M.V. The adiabatic phase and Pancharatnam's phase for polarized light. *Journal of Modern Optics* **34**, 1401-1407 (1987).

53. Lu, S.-Y. & Chipman, R.A. Interpretation of Mueller matrices based on polar decomposition. *JOSA A* **13**, 1106-1113 (1996).

54. Arteaga, O. & Canillas, A. Pseudopolar decomposition of the Jones and Mueller-Jones exponential polarization matrices. *JOSA A* **26**, 783-793 (2009).

55. Ossikovski, R., De Martino, A. & Guyot, S. Forward and reverse product decompositions of depolarizing Mueller matrices. *Optics Letters* **32**, 689-691 (2007).

56. Ortega-Quijano, N. & Arce-Diego, J.L. Mueller matrix differential decomposition. *Optics Letters* **36**, 1942-1944 (2011).

57. Arteaga, O., Garcia-Caurel, E. & Ossikovski, R. Anisotropy coefficients of a Mueller matrix. *JOSA A* **28**, 548-553 (2011).

58. He, H. et al. A possible quantitative Mueller matrix transformation technique for anisotropic scattering media/Eine mögliche quantitative Müller-Matrix-Transformations-

Technik für anisotrope streuende Medien. *Photonics & Lasers in Medicine* **2**, 129-137 (2013).

59. Ghosh, N., Wood, M.F. & Vitkin, I.A. Mueller matrix decomposition for extraction of individual polarization parameters from complex turbid media exhibiting multiple scattering, optical activity, and linear birefringence. *Journal of Biomedical Optics* **13**, 044036 (2008).

60. Gil, J.J. Characteristic properties of Mueller matrices. *JOSA A* **17**, 328-334 (2000).

61. Sun, M. et al. Characterizing the microstructures of biological tissues using Mueller matrix and transformed polarization parameters. *Biomedical Optics Express* **5**, 4223-4234 (2014).

62. Du, E. et al. Mueller matrix polarimetry for differentiating characteristic features of cancerous tissues. *Journal of Biomedical Optics* **19**, 076013 (2014).

63. He, H. et al. Application of sphere-cylinder scattering model to skeletal muscle. *Optics Express* **18**, 15104-15112 (2010).

64. He, H. et al. Two-dimensional backscattering Mueller matrix of sphere-cylinder scattering medium. *Optics Letters* **35**, 2323-2325 (2010).

65. Guo, Y. et al. A study on forward scattering Mueller matrix decomposition in anisotropic medium. *Optics Express* **21**, 18361-18370 (2013).

66. Samlan, C. & Viswanathan, N.K. Field-controllable Spin-Hall Effect of Light in Optical Crystals: A Conoscopic Mueller Matrix Analysis. *Scientific Reports* **8**, 2002 (2018).

67. Tyo, J.S., Goldstein, D.L., Chenault, D.B. & Shaw, J.A. Review of passive imaging polarimetry for remote sensing applications. *Applied Optics* **45**, 5453-5469 (2006).

68. Qi, J. & Elson, D.S. Mueller polarimetric imaging for surgical and diagnostic applications: a review. *Journal of Biophotonics* **10**, 950-982 (2017).

69. Azzam, R.M. in Polarization: Measurement, Analysis, and Remote Sensing, Vol. 3121 396-405 (International Society for Optics and Photonics, 1997).

70. Schulz, M. et al. Giant intrinsic circular dichroism of prolinol-derived squaraine thin films. *Nature Communications* **9**, 2413 (2018).

71. Ghosh, N. & Vitkin, A.I. Tissue polarimetry: concepts, challenges, applications, and outlook. *Journal of Biomedical Optics* **16**, 110801 (2011).

72. He, C. et al. Linear polarization optimized Stokes polarimeter based on four-quadrant detector. *Applied Optics* **54**, 4458-4463 (2015).

73. Chang, J. et al. Division of focal plane polarimeter-based 3× 4 Mueller matrix microscope: a potential tool for quick diagnosis of human carcinoma tissues. *Journal of Biomedical Optics* **21**, 056002 (2016).

74. Mahato, K. & Mazumder, N. Polarization-resolved Stokes-Mueller imaging: a review of technology and applications. *Lasers in Medical Science* (2019).

75. Azzam, R. Photopolarimetric measurement of the Mueller matrix by Fourier analysis of a single detected signal. *Optics Letters* **2**, 148-150 (1978).

76. Goldstein, D.H. & Chipman, R.A. Error analysis of a Mueller matrix polarimeter. *JOSA A* **7**, 693-700 (1990).

77. Smith, M.H. Optimization of a dual-rotating-retarder Mueller matrix polarimeter. *Applied Optics* **41**, 2488-2493 (2002).

78. Compain, E., Poirier, S. & Drevillon, B. General and self-consistent method for the calibration of polarization modulators, polarimeters, and Mueller-matrix ellipsometers. *Applied Optics* **38**, 3490-3502 (1999).

79. De Martino, A., Garcia-Caurel, E., Laude, B. & Drévillon, B. General methods for optimized design and calibration of Mueller polarimeters. *Thin Solid Films* **455**, 112-119 (2004).

80. Arteaga, O., Freudenthal, J., Wang, B. & Kahr, B. Mueller matrix polarimetry with four photoelastic modulators: theory and calibration. *Applied Optics* **51**, 6805-6817 (2012).

81. Qi, J. & Elson, D.S. A high definition Mueller polarimetric endoscope for tissue characterisation. *Scientific Reports* **6**, 25953 (2016).

82. Novikova, T., Pierangelo, A., De Martino, A., Benali, A. & Validire, P. Polarimetric imaging for cancer diagnosis and staging. *Optics and Photonics News* **23**, 26-33 (2012).

83. Da Costa, V. et al. Nondestructive imaging of live human keloid and facial tissue using multiphoton microscopy. *Archives of Facial Plastic Surgery* **10**, 38-43 (2008).

84. Qi, J., Barrière, C., Wood, T.C. & Elson, D.S. Polarized multispectral imaging in a rigid endoscope based on elastic light scattering spectroscopy. *Biomedical Optics Express* **3**, 2087-2099 (2012).

85. Qi, J. et al. Assessment of tissue polarimetric properties using Stokes polarimetric imaging with circularly polarized illumination. *Journal of Biophotonics* **11**, e201700139 (2018).

86. He, C. et al. Characterizing microstructures of cancerous tissues using multispectral transformed Mueller matrix polarization parameters. *Biomedical Optics Express* **6**, 2934-2945 (2015).

87. Nan, Z., Xiaoyu, J., Qiang, G., Yonghong, H. & Hui, M. Linear polarization difference imaging and its potential applications. *Applied Optics* **48**, 6734-6739 (2009).

88. Yun, T. et al. Monte Carlo simulation of polarized photon scattering in anisotropic media. *Optics Express* **17**, 16590-16602 (2009).

89. Qi, J., He, C. & Elson, D.S. Real time complete Stokes polarimetric imager based on a linear polarizer array camera for tissue polarimetric imaging. *Biomedical Optics Express* **8**, 4933-4946 (2017).

90. Rubin, N.A. et al. Matrix Fourier optics enables a compact full-Stokes polarization camera. *Science* **365**, eaax1839 (2019).

91. Azzam, R. Stokes-vector and Mueller-matrix polarimetry. *JOSA A* **33**, 1396-1408 (2016).

92. Pierangelo, A. et al. Ex-vivo characterization of human colon cancer by Mueller polarimetric imaging. *Optics Express* **19**, 1582-1593 (2011).

93. Pierangelo, A. et al. in Optical Biopsy IX, Vol. 7895 78950E (International Society for Optics and Photonics, 2011).

94. Antonelli, M.R. et al. in European Conference on Biomedical Optics 80872U (Optical Society of America, 2011).

95. Shukla, P. & Pradhan, A. Mueller decomposition images for cervical tissue: Potential for discriminating normal and dysplastic states. *Optics Express* **17**, 1600-1609 (2009).

96. Wood, M.F. et al. Polarization birefringence measurements for characterizing the myocardium, including healthy, infarcted, and stem-cell-regenerated tissues. *Journal of Biomedical Optics* **15**, 047009 (2010).

97. Wang, Y. et al. Mueller matrix microscope: a quantitative tool to facilitate detections and fibrosis scorings of liver cirrhosis and cancer tissues. *Journal of Biomedical Optics* **21**, 071112 (2016).

98. Schwider, J. in Progress in optics, Vol. 28 271-359 (Elsevier, 1990).

99. Dai, Y., Antonello, J. & Booth, M.J. Calibration of a phase-only spatial light modulator for both phase and retardance modulation. *Optics Express* **27**, 17912-17926 (2019).

100. Antonello, J. & Verhaegen, M. Modal-based phase retrieval for adaptive optics. *JOSA A* **32**, 1160-1170 (2015).

101. Allen, L., Beijersbergen, M.W., Spreeuw, R. & Woerdman, J. Orbital angular momentum of light and the transformation of Laguerre-Gaussian laser modes. *Physical Review A* **45**, 8185 (1992).

102. Mair, A., Vaziri, A., Weihs, G. & Zeilinger, A. Entanglement of the orbital angular momentum states of photons. *Nature* **412**, 313 (2001).

103. Bliokh, K.Y., Rodríguez-Fortuño, F.J., Nori, F. & Zayats, A.V. Spin–orbit interactions of light. *Nature Photonics* **9**, 796 (2015).

104. Friese, M., Nieminen, T., Heckenberg, N. & Rubinsztein-Dunlop, H. Optical alignment and spinning of laser-trapped microscopic particles. *Nature* **394**, 348 (1998).

105. Garcés-Chávez, V. et al. Observation of the transfer of the local angular momentum density of a multiringed light beam to an optically trapped particle. *Physical Review Letters* **91**, 093602 (2003).

106. Padgett, M. & Bowman, R. Tweezers with a twist. *Nature Photonics* **5**, 343 (2011).

107. Ngcobo, S., Litvin, I., Burger, L. & Forbes, A. A digital laser for on-demand laser modes. *Nature Communications* **4**, 2289 (2013).

108. Willner, A.E. et al. Optical communications using orbital angular momentum beams. *Advances in Optics and Photonics* **7**, 66-106 (2015).

109. Zhao, N., Li, X., Li, G. & Kahn, J.M. Capacity limits of spatially multiplexed free-space communication. *Nature Photonics* **9**, 822 (2015).

110. Parigi, V. et al. Storage and retrieval of vector beams of light in a multiple-degree-of-freedom quantum memory. *Nature Communications* **6**, 7706 (2015).

111. Wang, X.-L. et al. Quantum teleportation of multiple degrees of freedom of a single photon. *Nature* **518**, 516 (2015).

112. Malik, M. et al. Multi-photon entanglement in high dimensions. *Nature Photonics* **10**, 248 (2016).

113. Padgett, M.J. Orbital angular momentum 25 years on. *Optics Express* **25**, 11265-11274 (2017).

114. Ling, X. et al. Giant photonic spin Hall effect in momentum space in a structured metamaterial with spatially varying birefringence. *Light: Science & Applications* **4**, e290 (2015).

115. Ling, X. et al. Recent advances in the spin Hall effect of light. *Reports on Progress in Physics* **80**, 066401 (2017).

116. Ling, X., Zhou, X., Shu, W., Luo, H. & Wen, S. Realization of tunable photonic spin Hall effect by tailoring the Pancharatnam-Berry phase. *Scientific Reports* **4**, 5557 (2014).

117. Bliokh, K., Aiello, A. & Alonso, M. Spin-orbit interactions of light in isotropic media. *The Angular Momentum of Light*, 174-245 (2012).

118. Liberman, V. & Zel'dovich, B.Y. Spin-orbit interaction of a photon in an inhomogeneous medium. *Physical Review A* **46**, 5199 (1992).

119. Cardano, F. & Marrucci, L. Spin–orbit photonics. *Nature Photonics* **9**, 776 (2015).

120. Xiao, S. et al. Spin-dependent optics with metasurfaces. *Nanophotonics* **6**, 215-234 (2016).

121. Bliokh, K.Y. & Aiello, A. Goos–Hänchen and Imbert–Fedorov beam shifts: an overview. *Journal of Optics* **15**, 014001 (2013).

122. Barnett, S.M. Optical angular-momentum flux. *Journal of Optics B: Quantum and Semiclassical Optics* **4**, S7 (2001).

123. Brasselet, E. et al. Dynamics of optical spin-orbit coupling in uniaxial crystals. *Optics Letters* **34**, 1021-1023 (2009).

124. Bomzon, Z.e., Biener, G., Kleiner, V. & Hasman, E. Space-variant Pancharatnam–Berry phase optical elements with computer-generated subwavelength gratings. *Optics Letters* **27**, 1141-1143 (2002).

125. Biener, G., Niv, A., Kleiner, V. & Hasman, E. Formation of helical beams by use of Pancharatnam–Berry phase optical elements. *Optics Letters* **27**, 1875-1877 (2002).

126. Bomzon, Z.e., Kleiner, V. & Hasman, E. Pancharatnam–Berry phase in space-variant polarization-state manipulations with subwavelength gratings. *Optics Letters* **26**, 1424-1426 (2001).

127. Marrucci, L., Manzo, C. & Paparo, D. Pancharatnam-Berry phase optical elements for wave front shaping in the visible domain: switchable helical mode generation. *Applied Physics Letters* **88**, 221102 (2006).

128. Shitrit, N., Bretner, I., Gorodetski, Y., Kleiner, V. & Hasman, E. Optical spin Hall effects in plasmonic chains. *Nano Letters* **11**, 2038-2042 (2011).

129. Shitrit, N. et al. Spin-optical metamaterial route to spin-controlled photonics. *Science* **340**, 724-726 (2013).

130. Li, P., Lv, D., He, H. & Ma, H. Separating azimuthal orientation dependence in polarization measurements of anisotropic media. *Optics Express* **26**, 3791-3800 (2018).

131. Kumar, V. & Viswanathan, N.K. Topological structures in vector-vortex beam fields. *JOSA B* **31**, A40-A45 (2014).

132. Galvez, E.J. & Khajavi, B. Monstar disclinations in the polarization of singular optical beams. *JOSA A* **34**, 568-575 (2017).

133. Samlan, C. & Viswanathan, N.K. Chiral dynamics of exceptional points in weakly absorbing biaxial crystal. *Optics Letters* **43**, 3538-3541 (2018).

134. Samlan, C., Naik, D.N., Viswanathan, N.K. & Miyamoto, Y. Ultra short polarization singularities from two beam interference. (2018).

135. Lu, X. & Chen, L. Spin-orbit interactions of a Gaussian light propagating in biaxial crystals. *Optics Express* **20**, 11753-11766 (2012).

136. Lu, X., Wu, Z., Zhang, W. & Chen, L. Polarization singularities and orbital angular momentum sidebands from rotational symmetry broken by the Pockels effect. *Scientific Reports* **4**, 4865 (2014).

137. Samlan, C., Naik, D.N. & Viswanathan, N.K. Isogyres–Manifestation of Spin-orbit interaction in uniaxial crystal: A closed-fringe Fourier analysis of conoscopic interference. *Scientific Reports* **6**, 33141 (2016).

138. Berry, M. & Dennis, M. The optical singularities of birefringent dichroic chiral crystals. *Proceedings of the Royal Society of London. Series A: Mathematical, Physical and Engineering Sciences* **459**, 1261-1292 (2003).

139. Dong, Y. et al. Quantitatively characterizing the microstructural features of breast ductal carcinoma tissues in different progression stages by Mueller matrix microscope. *Biomedical Optics Express* **8**, 3643-3655 (2017).

140. Zhou, J. et al. Optical edge detection based on high-efficiency dielectric metasurface. *Proceedings of the National Academy of Sciences* **116**, 11137-11140 (2019).

141. Nye, J.F. & Berry, M.V. Dislocations in wave trains. *Proceedings of the Royal Society of London. A. Mathematical and Physical Sciences* **336**, 165-190 (1974).

142. Dennis, M., O'Holleran, K. & Padgett, M. (Elsevier, 2009).

143. Bozinovic, N. et al. Terabit-scale orbital angular momentum mode division multiplexing in fibers. *Science* **340**, 1545-1548 (2013).

144. Slussarenko, S. et al. Guiding light via geometric phases. *Nature Photonics* **10**, 571 (2016).

145. Sephton, B., Dudley, A. & Forbes, A. Revealing the radial modes in vortex beams. *Applied Optics* **55**, 7830-7835 (2016).

146. Maurer, C., Jesacher, A., Fürhapter, S., Bernet, S. & Ritsch-Marte, M. Tailoring of arbitrary optical vector beams. *New Journal of Physics* **9**, 78 (2007).

147. Rosales-Guzmán, C., Ndagano, B. & Forbes, A. A review of complex vector light fields and their applications. *Journal of Optics* **20**, 123001 (2018).

148. Wang, H., Shi, L., Lukyanchuk, B., Sheppard, C. & Chong, C.T. Creation of a needle of longitudinally polarized light in vacuum using binary optics. *Nature Photonics* **2**, 501 (2008).

149. Bauer, T. et al. Observation of optical polarization Möbius strips. *Science* **347**, 964-966 (2015).

150. Naidoo, D. et al. Controlled generation of higher-order Poincaré sphere beams from a laser. *Nature Photonics* **10**, 327 (2016).

151. Beckley, A.M., Brown, T.G. & Alonso, M.A. Full poincaré beams. *Optics Express* **18**, 10777-10785 (2010).

152. Cardano, F., Karimi, E., Marrucci, L., de Lisio, C. & Santamato, E. Generation and dynamics of optical beams with polarization singularities. *Optics Express* **21**, 8815-8820 (2013).

153. Huang, B., Wang, W., Bates, M. & Zhuang, X. Three-dimensional super-resolution imaging by stochastic optical reconstruction microscopy. *Science* **319**, 810-813 (2008).

154. Youngworth, K.S. & Brown, T.G. Focusing of high numerical aperture cylindrical-vector beams. *Optics Express* **7**, 77-87 (2000).

155. Kimura, W. et al. Laser acceleration of relativistic electrons using the inverse Cherenkov effect. *Physical Review Letters* **74**, 546 (1995).

156. Niziev, V. & Nesterov, A. Influence of beam polarization on laser cutting efficiency. *Journal of Physics D: Applied Physics* **32**, 1455 (1999).

157. Han, W., Cheng, W. & Zhan, Q. Flattop focusing with full Poincaré beams under low numerical aperture illumination. *Optics Letters* **36**, 1605-1607 (2011).

158. Kitano, I., Toyama, M. & Nishi, H. Spherical aberration of gradient-index rod lenses. *Applied Optics* **22**, 396-399 (1983).

159. Knittel, J., Schnieder, L., Buess, G., Messerschmidt, B. & Possner, T. Endoscope-compatible confocal microscope using a gradient index-lens system. *Optics Communications* **188**, 267-273 (2001).

160. Liu, Z. et al. Generation of arbitrary vector vortex beams on hybrid-order Poincaré sphere. *Photonics Research* **5**, 15-21 (2017).

161. Balzarotti, F. et al. Nanometer resolution imaging and tracking of fluorescent molecules with minimal photon fluxes. *Science* **355**, 606-612 (2017).

162. Booth, M.J. Adaptive optical microscopy: the ongoing quest for a perfect image. *Light: Science & Applications* **3**, e165 (2014).

163. Gustafsson, M.G. Surpassing the lateral resolution limit by a factor of two using structured illumination microscopy. *Journal of Microscopy* **198**, 82-87 (2000).

164. Otani, Y., Wakayama, T., Oka, K. & Umeda, N. Spectroscopic Mueller matrix polarimeter using four-channeled spectra. *Optics Communications* **281**, 5725-5730 (2008).

165. Nishiyama, I., Yoshida, N., Otani, Y. & Umeda, N. Single-shot birefringence measurement using radial polarizer fabricated by direct atomic force microscope stroking method. *Measurement Science and Technology* **18**, 1673 (2007).

166. Chang, J., Zeng, N., He, H., He, Y. & Ma, H. Single-shot spatially modulated Stokes polarimeter based on a GRIN lens. *Optics Letters* **39**, 2656-2659 (2014).

167. Sabatke, D. et al. Optimization of retardance for a complete Stokes polarimeter. *Optics Letters* **25**, 802-804 (2000).

168. Ji, N. Adaptive optical fluorescence microscopy. *Nature Methods* **14**, 374 (2017).

169. Girkin, J.M., Poland, S. & Wright, A.J. Adaptive optics for deeper imaging of biological samples. *Current Opinion in Biotechnology* **20**, 106-110 (2009).

170. Booth, M.J., Neil, M.A., Juškaitis, R. & Wilson, T. Adaptive aberration correction in a confocal microscope. *Proceedings of the National Academy of Sciences* **99**, 5788-5792 (2002).

171. Débarre, D. et al. Image-based adaptive optics for two-photon microscopy. *Optics Letters* **34**, 2495-2497 (2009).

172. Hell, S.W. et al. The 2015 super-resolution microscopy roadmap. *Journal of Physics D: Applied Physics* **48**, 443001 (2015).

173. Hu, Q., Dai, Y., He, C. & Booth, M.J. Arbitrary vectorial state conversion using liquid crystal spatial light modulators. *Optics Communications* (2019).

174. Dai, Y. et al. Active compensation of extrinsic polarization errors using adaptive optics. *Optics Express* **27**, 35797-35810 (2019).

175. Žurauskas, M. et al. IsoSense: frequency enhanced sensorless adaptive optics through structured illumination. *Optica* **6**, 370-379 (2019).

176. Kubby, J.A. Adaptive optics for biological imaging. (CRC press, 2013).

177. Bueno, J.M., Gualda, E.J. & Artal, P. Adaptive optics multiphoton microscopy to study ex vivo ocular tissues. *Journal of Biomedical Optics* **15**, 066004 (2010).

178. Thompson, A.J., Paterson, C., Neil, M.A., Dunsby, C. & French, P.M. Adaptive phase compensation for ultracompact laser scanning endomicroscopy. *Optics Letters* **36**, 1707-1709 (2011).

179. Tyson, R.K. Principles of adaptive optics. (CRC press, 2015).

180. Banerjee, K., Rajaeipour, P., Ataman, Ç. & Zappe, H. in Adaptive Optics: Analysis, Methods & Systems OW2J. 6 (Optical Society of America, 2018).

181. Chipman, R.A. & Chipman, L.J. Polarization aberration diagrams. *Optical Engineering* **28**, 282100 (1989).

182. Chipman, R.A. Polarization aberrations (thin films). (1987).

183. McGuire, J.P. & Chipman, R.A. Polarization aberrations. 1. Rotationally symmetric optical systems. *Applied Optics* **33**, 5080-5100 (1994).

184. McGuire, J.P. & Chipman, R.A. Polarization aberrations. 2. Tilted and decentered optical systems. *Applied Optics* **33**, 5101-5107 (1994).

185. Chipman, R.A. Polarization analysis of optical systems. *Optical Engineering* **28**, 280290 (1989).

186. Yun, G., Crabtree, K. & Chipman, R.A. Skew aberration: a form of polarization aberration. *Optics Letters* **36**, 4062-4064 (2011).

187. Chen, J., Kong, L. & Zhan, Q. Demonstration of a vectorial optical field generator with adaptive close loop control. *Review of Scientific Instruments* **88**, 125111 (2017).

188. Chang, J., Zeng, N., He, H., Guo, Y. & Ma, H. Removing the polarization artifacts in Mueller matrix images recorded with a birefringent gradient-index lens. *Journal of Biomedical Optics* **19**, 095001 (2014).

189. Masters, B.R. & So, P. Handbook of biomedical nonlinear optical microscopy. (Oxford University Press, 2008).

190. Žurauskas, M., Barnstedt, O., Frade-Rodriguez, M., Waddell, S. & Booth, M.J. Rapid adaptive remote focusing microscope for sensing of volumetric neural activity. *Biomedical Optics Express* **8**, 4369-4379 (2017).

191. Samim, M., Krouglov, S. & Barzda, V. Nonlinear Stokes-Mueller polarimetry. *Physical Review A* **93**, 013847 (2016).

192. Krouglov, S. & Barzda, V. Three-dimensional nonlinear Stokes–Mueller polarimetry. *JOSA B* **36**, 541-550 (2019).

Journal Publications

1) C. He*, J. Chang, Q. Hu, J. Wang, J. Antonello, H. He, S. Liu, J. Lin, B. Dai, D. S. Elson, P. Xi, H. Ma and M. J. Booth*. "Complex vectorial optics through gradient index lens cascades." ***Nature Communications*** 10.1 (2019): 1-8.

*- Highlighted by **Nature Photonics**, in News & Views, 'Graded lens surprise'.*
*- Highlighted by **Light: Science & Applications**, in News & Views, 'Common elements for uncommon light: vector beams with GRIN lenses'.*
*- Double-highlighted News in **Dynamic Optics and Photonics Group**, University of Oxford, 'Vectorial GRIN lens paper highlighted'.*

***C.H.** and M.J.B. conceived the main ideas for the applications of GRIN lens cascades, developed the concepts, and planned the modelling and experiments. **C.H.,** J.C., J.W., Q.H., and J.A. performed GRIN lens equations, and contributed to polarization measurement methods and interferometry. **C.H.,** B.D., Q.H., J.C., J.L., and P.X. performed the simulations, VVB mathematical approaches and the analysis of OAM components. **C.H.,** J.W., and H.H. performed the PSF measurement and tested the MM polarimeter, and S.L. prepared the samples. **C.H.,** J.C., J.L., H.H., D.E.S., and H.M. contributed to MMPD method, MM calculation algorithm, and MM analysis method. **C.H.** carried out the remaining experiments, prepared the figures, and analysed the results. **C.H.** and M.J.B. wrote the paper.*

2) Y. Dai, **C. He**, J. Wang, R. Turcotte, L. Fish, M. Wincott, Q. Hu and M. J. Booth*. "Active compensation of extrinsic polarization errors using adaptive optics." ***Optics Express*** 27.24 (2019): 35797-35810.

*M.J.B. conceived the idea. Y.D. performed the experiments and wrote the paper. **C.H.** developed and performed the polarization measurement and analysis methods. J.W., L.F., Q.H., and Y.D. built the modulation and generation method and competed the software. R.T. prepared the sample.*

3) [Q. Hu, Y. Dai, **C. He** and M. J. Booth*]. "Arbitrary vectorial state conversion using liquid crystal spatial light modulators." ***Optics Communications*** (2019).

*M.J.B. conceived the idea and wrote the paper. **C.H.**, Q.H., and Y.D. performed the mathematic calculation.*

*[]: co-first author *: corresponding author*

Participated Conference

Oral presentation:

1) Conference name: AOIM XII Workshop Proceedings / Face2Phase
Time duration: 21-25 October, 2019
Place: Science Center of Delft University, Delft, Netherlands

2) Conference name: Light Conference 2019
Time duration: 16-18 July, 2019
Place: Changchun Institute of Optics, Fine Mechanics and Physics, Chinese Academy of Sciences, Changchun, China

Won conference prize: Finalist (Top 10) of the Best Student Presentations

3) Conference name: Focus on Microscopy 2019
Time duration: 14-17 April, 2019
Place: the Queen Elizabeth II (QEII) conference centre, Broad Sanctuary, Westminster, London, UK

Post presentation:

1) Conference name: Oxford Photonics Day
Time duration: 24 April, 2019
Place: Department of Engineering Science, University of Oxford, Oxford, UK

Won conference prize: **Student Poster Presentation Prize, 2nd Place**